



Eidgenössische Technische Hochschule Zürich
Swiss Federal Institute of Technology Zurich



Master Thesis

Experimental study on the seismic and aseismic deformation during the failure of granitic rock

Submitted to the
Earth Sciences Department at
ETH Zürich

Under the supervision of
Dr. Paul Antony Selvadurai, Swiss Seismological Service, ETH Zürich
Dr. Claudio Madonna, Geological Institute, ETH Zürich
Prof. Dr. Stefan Wiemer, Swiss Seismological Service, ETH Zürich

Zihua Niu

zihniu@student.ethz.ch

19-952-043

August 30, 2021

Acknowledgements

Much support has been received in the course of this research. I would like to give my heartfelt thanks to my supervisors, Dr. Paul Antony Selvadurai, Dr. Claudio Madonna and Prof. Dr. Stefan Wiemer. I could never reach this far without their knowledge and experience in the conducting of experiments, in the writing of scientific report and in the manners of delivery research findings to my colleagues. Especially, I would like to give my sincere appreciation to Dr. Paul Antony Selvadurai who has dedicated a lot of time in discussing scientific problems with me and in helping me improve my scientific writing and presentation. He is not only very responsive to my questions but encouraging when I propose my preliminary ideas to him. I have learnt a lot under his supervision.

I have also enjoyed the time spent with my colleague in the LabQuake team – Antonio Felipe Salazar Vasquez, Patrick Bianchi and Sofia Michail. Their accompany made the life in the lab more enjoyable. I have also learnt a lot from their patience and proficiency. Very grateful to them all. I would also like to thank Dr. Linus Villiger and Markus Rast for their patient discussion with me in the course of this thesis.

Special thanks would be also given to my dear mom and dad. Sometimes I am too submerged in my studies and neglect their care for me. Thank you so much for always supporting my decisions!

I would also express my thanks to Rui Wu, who has been very supportive for me during the course of my masters study. He has given me many informative suggestions both in academic studies and in badminton.

The two years I spent in Zurich have been exciting and rewarding. I have greeted friends from different culture backgrounds, tried things that I have never done before. I think I really adore this peaceful city and will always miss my life here.

Abstract

During the exploration of geothermal energy, fluids are often injected into the high temperature host rocks in the upper lithosphere for efficient heat or electricity production. It is known that large-scale injection activity will perturb the subsurface stress field, resulting in nucleation and propagation of fractures or reactivation of the existing faults. These mechanisms damage the rock and are accompanied by both static (aseismic) and dynamic (seismic) deformation of the subsurface materials. The related dynamic processes are associated with induce seismicity that are continuous to raise the public safety concerns for the geothermal projects. Mitigation of the injection-related seismic hazards has become a major challenge to geoscientists and geothermal engineers. Solutions to the problem rely on the in-depth understanding of how aseismic and seismic deformation are correlated during the progressive failure of rocks. While the injection is conducted at the scale of meters to decameters, nucleation of the dynamic fault propagation might initiate from failure at millimeter-scale or even lower. Laboratory studies have been instrumental in developing a fundamental understanding of rock deformation and failure processes and continues to expand our insight.

This study performed three tests on intact specimens of Rotondo granite in a triaxial configuration which aimed to fill the gap between lab-scale and field-scale observations of the physical processes during the progressive failure of rocks. A toolbox for events localization, moment tensor inversion, stress inversion and seismic statistics analysis is developed for the seismic data collected from the broadband PCT-LBQ acoustic emission (AE) sensors. Seismic analysis is combined with the cutting-edge distributed strain field measurement with fiber optics (FO) cables. Results and interpretations of the data in the experiments can be summarized as follows: (1) Aseismic deformation is the predominant process during the failure of rock in the confined compression test. Seismic deformation only accounts for $[0.07 \text{ to } 4] \times 10^{-2}$ percent of the total anelastic deformation. (2) Fractal dimension (D_q) and b-value in Gutenberg-Richter relation decrease as the sample approaches failure in general sense. The correlation between D_q and b-value is rather complex and can be correlated to the details on how the faults nucleate and propagate. The angles between normal and slip vectors of moment tensors drop from ~ 108 degrees to ~ 87 degrees, indicating the change from compressive to expansive seismic events. (3) At the early stage of failure prior to the formation of large-scale fractures, the perturbation on the strain field is found to be nearly inversely proportional to r^{-n} , where r is the distance to seismic sources and n is found to be around 4, which follows the theoretical estimation of the strain field perturbation from a point source dislocation. (4) Preliminary efforts into unstructured 3D stress inversion, derived from the seismicity clouds, has been validated by the distributed strain field determined using fiber optics technologies. The combination of AE and FO proves promising in revealing how seismicity is related to the progressive failure of the rock.

Contents

Acknowledgements	i
Abstract	ii
1 Introduction	1
1.1 Induced seismicity in the field	1
1.2 Down-scaling from field to laboratory	3
1.3 Aims of this study	4
2 Background	6
2.1 A historical recap on acoustic emission testing	6
2.2 Proposed developments in AE methodology	9
2.3 Rotondo granite	10
2.3.1 Mineralogical composition	10
2.3.2 Mechanical Properties	12
2.4 Experimental Facility	12
2.4.1 Calibration station	12
2.4.2 LabQuake	13
2.4.3 Elsys data acquisition system (DAQ)	14
2.4.4 Acoustic emission sensors	14
2.4.5 Fiber optics technology	16
3 Methodology	18
3.1 Experimental procedures	18
3.1.1 System stiffness calibration	18
3.1.2 LBQ0	20

3.1.3 LBQ1	21
3.1.4 LBQ2	22
3.2 Data reduction and processing	25
3.2.1 Static properties of the sample	25
3.2.2 Spectrum analysis for signals and noises	25
3.2.3 Events detection and data reduction	29
3.2.4 Arrival picking	30
3.2.5 Ultrasonic tomography	35
3.2.6 Localization	35
3.2.7 Sensor calibration	37
3.2.8 Moment tensor inversion	40
3.2.9 Stress inversion	42
3.2.10 Fiber optics technique	45
3.2.11 Methods of statistical analysis	46
4 Results	48
4.1 Change of velocity structure	49
4.1.1 Velocity change during the cyclic loading	49
4.1.2 Ultrasonic tomography during the failure test	49
4.2 Localized events	49
4.3 Magnitudes and types of moment tensors	52
4.4 Stress inversion	54
4.5 Strain field	56
5 Discussion	60
5.1 The relationship between the seismic moment release and the anelastic deformation across the sample	60
5.2 What occurs on the spatio-temporal front	61
5.3 Orientation of the strain/stress field and that of the cracks	63
5.4 Perturbation of the stress field by AE events	66

6 Conclusions	68
6.1 Summary	68
6.2 Outlook	69
A Accuracy of localization with ball drop experiments	A-1
B Detailed steps in calibration with the capillary fracturing source	B-1
C Declaration of Originality	C-1

List of Tables

2.1	Physical and mechanical properties of the Rotondo granite under zero confining pressure (David et al., 2020).	13
3.1	Summary of the sample sizes in the three experiments.	18
3.2	The list of parameters for ultrasonic tomography during the Stage I of LBQ2. . . .	23
3.3	The list of parameters for ultrasonic tomography and DAQ during the Stage II of LBQ2. .	23
3.4	Parameters of the DAQ for the recording of the AEs.	26
3.5	Summary of the parameters used for ultrasonic tomography and events localization in FaATSO.	37

List of Figures

1.1	Industrial activities that can trigger seismicity from Grigoli et al. (2017). (a) This illustrates how fault shear stress τ , fault normal stress σ and pore pressure p on the fault are distributed on the fault. The injected fluids can reach the pre-existing fault through diffusion in rocks with relatively uniform permeability (b) or more effectively through a layer with high permeability (c). (d) This shows that fractures and seismic events can also be generated during hydraulic fracturing in intact rocks.	2
1.2	Adapted from Obara and Kato (2016). Schematic depiction of seismic and aseismic slip locations on the Nankai subduction zone. Red boxes depict the approximate environmental condition attainable in LabQuake facilities.	3
2.1	Adapted from Scholz (1968). A schematic diagram that shows how Mogi (1966) recorded the acoustic emission signals using one piezoelectric transducer.	7
2.2	(a) Transformation from relatively smooth increase of frictional force along the fault in slow stable sliding to a sudden drop when dynamic rupture occurs (Rubinstein et al., 2007). Before each large stress drop, precursory decrease of seismic b-values (b) and spatial correlation dimensions (c) are systematically observed (Dresen et al., 2020). (d) Complex fault geometry and heterogeneous mechanical properties across the fault zone. The macroscopic failure induced in the majorshock is marked by a red curve and some of the micro failures that possibly occur in foreshocks are marked by yellow curves.	8
2.3	(a) A general schematic of calibration station, which consists of electromagnetic holder, steel balls with different diameters, steel transfer plate, PZT sensor array, extruded aluminum framework, etc (Wu et al., 2020). (b) is the calibrated PCT-MCXLBQ sensor. (c) is modified from Brantut (2018) and Kwiatek et al. (2016), is the framework of the package that combines FaATSO and HybridMT to do source relocation, rock tomography, moment tensor and stress inversion. (d) This shows the verification of stress inversion. Normal vectors (blue arrows) of the clustered events (circles) and the local weak planes (red arrows) predicted by stress inversion results and Mohr-Coulomb's law, with internal friction angle set to 44°. Colored circles are nodes of each cluster. The color indicates the number of single events in each cluster (darker color corresponds to more single events). And the zig-zag curves at the tips of initial flaws are macro-cracks observed in the experiment.	9
2.4	Adapted from Hafner et al. (1975); Berger et al. (2016); Rast (2020). Main map: geological overview of the area around the Bedretto tunnel (the dashed gray curve). Coordinates outside of the map correspond to the Swiss Grid (CH1903++). Large-scale map: tectonic overview of the Central Alps, the black rectangle represents the cutout of the main map.	11
2.5	Adapted from Rast (2020). Thin section cutouts of the equigranular Rotondo granite used in our experiments, crossed polarized light in all photomicrographs. (a) shows muscovite (Ms), Pl, Bt, Kfs and (b) shows Ms, Bt and Pl.	12

2.6	Adapted from Wu et al. (2020) and Selvadurai et al.. Structure of the calibration station using capillary fracturing (a, c) and ball drop (b).	14
2.7	Experiment setup that can be implemented in the LabQuake facilities. This shows how fluids are injected, how temperature, axial stress and confining pressure are loaded on the intact sample (I), naturally fractured sample (II) and saw-cut sample (III).	15
2.8	The photo of the Elsys DAQ (a) and the schematic diagram that shows the components and how they are connected (b).	15
2.9	Adapted from Selvadurai et al.. The schematic diagram that shows the inner structure of the PCT-LBQ piezoelectric sensor used in the experiments.	16
2.10	(a) The photo that shows how the acrylate and the polyimide cables are distributed on the surface of the sample. (b) Adopted from (Salazar et al., in preparation). The schematic diagram showing the geometry of the Acrylate (in green) and the Polyimide cables (in yellow).	17
3.1	The group of photos that shows how the FO, AE sensors and the rubber jacket are prepared. (a) Place jacket around plastic dummy sample and use extra set of adapters to ensure the sample is at the correct height. (b) Print the mapping of sensors distribution on a paper at 1:1 scale. (c) Wrap the printed map around the rubber jacket. (d) Punch the holes in the rubber with plastic piece as the transfer material. (e) Squeeze the porthole adapter into the hole. It is fixed by the frictional snug and stays in place with no glue. (f) Use the rubber glue to tack the porthole adapters to the viton sleeve. (g) Do not fully cover the seam with glue, this allows for air to escape. (h) Use the applicator gun and stick to bead both the sensor to porthole and porthole to viton jacket using HySOL 9455. (i) Cure in oven.	19
3.2	(a) The aluminum sample for the calibration of the stiffness of the framework. While the region inside the red rectangle is involved in the calibration with respect to the displacement of the loading piston, the diagram beside the frame shows the part of the framework that the LVDTs measure. (b) The stiffness of the loading framework that changes with the confining pressure.	19
3.3	(a) The photo that shows the jacketed sample in LBQ0 and the connection of all the sensors to the framework. (b) The loading protocols in LBQ0.	20
3.4	(a) The map that shows how the AE sensors and FO fibers are distributed. (b) The jacketed sample in LBQ1.	21
3.5	The loading protocols in LBQ1. In Phase I, the deviatoric stress was cycled at different confining pressure while in Phase II the sample was loaded to failure.	22
3.6	The loading protocols in the Stage I of LBQ2. The confining pressure was cycled for three times and ultrasonic tomography was conducted in each cycle but with different surveying parameters listed in Table 3.2	23
3.7	The loading protocols in the Stage II of LBQ2. During the Phase I, the deviatoric stress was cycled between 5 and 100 or 120 MPa to generate some AE events and in Phase II the deviatoric stress was cycled in a lower range between 5 and 50 MPa at different confining pressure.	24
3.8	The loading protocols in the Stage III of LBQ2. The sample was directly loaded to failure.	25

3.9 (a) The photo that shows how jacket has been distorted in Stage I of LBQ2. (b) Photo that shows the failure of jacket and leakage. The crack is shown inside the red rectangle.	26
3.10 Static properties of the samples in LBQ0-2. (a) Change of Young's modulus with the confining pressure in LBQ0, computed from the measurement with the calibrated loading piston, LVDTs and FO. (b) Change of Young's modulus with the confining pressure in LBQ1, computed from the measurement with the calibrated LVDTs and FO. (c) Change of Young's modulus with the confining pressure in LBQ2, computed from the measurement with the calibrated LVDTs. Change of Young's modulus in LBQ1 is shown together for comparison with blue dots.	27
3.11 Time series (a) and frequency spectra (b) of the background noises and desired signals from LBQ0, LBQ1 and LBQ2. The spectra of signals are computed from signals of the weakest locatable events in all three experiments.	28
3.12 The change of maximum number of detections as a function of the window size. The proper window size should contain a maximum of 10 detections on the 10 channels and is shaded in green.	30
3.13 Signals of one seismic event recorded at two channels in LBQ0. The first P-wave arrivals (the color-coded stars) are picked with the AR-AIC algorithms with the varied length of variance window.	31
3.14 Signals recorded on 10 channels. The interval between two events is only around 100 microseconds so that the coda waves (shaded in blue rectangles) of Event 1 pollute the first arrivals of Event 2.	32
3.15 The bottom subplot (c) shows the time series of an example trace that contains seismic events but the arrivals can be wrongly picked with the AIC picker. (b) AIC series of the time series in (c). The blue dashed rectangle marks the local feature that may characterize the arrivals better than the global minimum. (a) Smoothed difference of the AIC series in (b).	33
3.16 (a) The diagram that shows the adapted AIC (Ada-AIC) picking algorithm. (b) Signals of one example event recorded on 10 channels. The arrivals picked with the Ada-AIC picker (red stars) perform better than the AIC picker (green squares) on three channels.	34
3.17 Arrival picking using the HOS picker. Sensor 2 is the recordings at the source sensor while signals at four receiver sensors are shown as examples. Blue rectangles are the starting positions of the window for statistical analysis that move from left to right. The picked arrivals are marked with red dots.	36
3.18 Set up of the calibration station. A structure consisting of a casing and three springs is designed to keep the sensors in good contact with the steel plate.	38
3.19 IR of the sensor PCT-LBQ-0103 calibrated before and after experiments with 20 dB gain and 40 dB gain. The blue dotted curve is the IR at 20 dB gain before LBQ0. The green dashed-dotted curve is the IR at 20 dB gain after LBQ0. The red dashed curve is the IR at 20 dB gain after LBQ0 and with welded nickel tip. The black solid curve with hollow circles is the IR at 20 dB gain after LBQ2. And the black solid curve with filled circles is the IR at 40 dB gain after LBQ2.	39

3.20	Adapted from Udiás et al. (2014). Source time function (STF) models for the scalar moment (M_0) and moment rate in the point representation of a seismic source. τ_T is the rise time of the scalar moment.	42
3.21	Example of the calibrated signals where the P-wave arrivals and first zero-crossings are marked with orange rectangles and green triangles. The P-wave Omega is computed by integrating the curve between the arrivals and the first zero-crossings.	43
3.22	The equal-area source type plot adapted from Hudson et al. (1989). The types of events represented by special points on the diagram are marked.	44
4.1	Change of the P-wave velocity with the confining pressure and with the deviatoric stress in LBQ0, which is also representative of the observations in LBQ1.	48
4.2	The change of the 3D velocity structure of the sample in LBQ1 as the axial stress increased from 5 MPa to around 300 MPa calculated with FaATSO. The times of tomography results shown in (b)-(e) are marked in (a) with four red dots.	50
4.3	The change of P-wave velocity between two selected sensor pairs in LBQ1 (left) and LBQ2 (right). While the ray paths between sensor 3 and sensor 8 in LBQ1 and between sensor 2 and senor 7 in LBQ2 cross the fault planes proposed according to the localization results, the other two ray paths are most likely not passing any major faults.	51
4.4	(a) Spatial distribution of the geometrical means of the changes at the 10 sensors (white dots) if the location of the event at a point is moved for 1 mm. (b) Spatial distribution of the geometrical mean of location errors resulted from 1 micro-second error in arrival picking at ten sensors.	52
4.5	Locations of events in LBQ1 (a) and LBQ2 (b). The events are color-coded according to their time of occurrence. The three dashed circles in (b) marks the clusters mentioned in Figure 4.6c.	53
4.6	(a) Fitting of the frequency magnitude distribution of the events with estimation of the magnitude of completeness. (b) The cumulative moment release in time. (c) The magnitude of all events over time. The three dashed circles in (b) marks the clusters mentioned in Figure 4.5b.	54
4.7	(a- to d-I) Hudson plots for the full seismic catalog (a-I) and the events in each seismic swarm (b- to d-I) marked in Figure 4.6c. Dots are plotted in colors corresponding to those in Figure 4.6c. (a- to d-II) The triangle diagrams for the full seismic catalog (a-II) and the events in each seismic swarm (b- to d-I) marked in Figure 4.6c. The orange beach ball and dots are categorized as normal faults, the cyan beach ball and dots as reverse fault and the red beach ball and purple dots as strike-slip fault. The gray beach balls and dots mark events that are mixtures of these three major types of DC events.	55

4.8 (a) Stress inversion results for the events occurs before 898 s in LBQ2. The color-coded events in the top-middle subplots show how the events are clustered for stress inversion. The other three subplots surrounding them give the orientations of each cluster viewing from three perspectives. “Principal vector 1” (green arrows) and “Principal vector 3” (red arrows) correspond to the direction of the largest (most tensile) and the smallest (most compressive) eigenvalues. (b) Stress inversion results for the events occurs after 898 s in LBQ2. (c) Temporal variation of orientation angles of the clusters in each one-second window. Average of the orientation angles is plotted in solid green curves, while the raw and smoothed standard deviations are plotted in dashed gray and black curves.	57
4.9 Comparison of the localization results at 890 s (a, b), 898 s (c, d), 906 s (e, f), 914 s (g, h) and 922 s (i, j) with surface hoop strain field measured with the optical fibers.	58
4.10 Variation of axial (a), hoop (c) and volumetric (e) strain with the time to failure. The black curves with error bars are the averaged total strain values across the sample and the green curves are the anelastic strain of each component. The variation of the above three components with the deviatoric stress is shown in (b), (d) and (f), respectively. Black circles mark the proposed elastic segment in deformation.	59
5.1 (a) Comparison between the averaged anelastic deformation and cumulative moment. The cumulative moment is converted to the same unit as strain through dividing it by divided by the bulk modulus times the volume of the sample. (b) Comparison between the averaged anelastic deformation and cumulative volumetric deformation estimated from the moment tensors.	61
5.2 (a) The cumulative number of events against the time to failure. (b) The occurrence rate against the time to failure at the log-log scale. The dashed gray curve is the raw occurrence rate computed from the full seismic catalog in LBQ2. The solid black curve smooths the variation for better visualization of the trend and red curve is fitted using the raw data against the modified Omori’s law.	62
5.3 (a) The change of deviatoric stress (black dots) and moment magnitude of events (blue dots) in time serving as the indicator of the loading stage as statistical variables varies. The pink dots indicate the start of nucleation and propagation of the first fault, while the green dots mark the failure of the sample (the time when the sudden stress drop occurs). (b) Temporal variation of the b-value and the fractal dimension. (c) Temporal variation of different components of the moment tensors (the solid and dashed curves) and of the angle between normal and the slip vectors (the red curve).	64
5.4 The correlation between b-value and fractal dimension (D_2). The values before 898 s (during the upward propagation of the first fault) are marked in black dots and data afterwards are color-coded from brown to yellow. The region where $D_2 = 2b$ is marked by dashed blue line for comparison. The green circle with error bars marks the b-value and the fractal dimension estimated with all the events.	65
5.5 Migration of the peaks in the surface strain field from around 882 s (left) to 906 s (right). The dashed white line is at the same position in both subplots, while the solid white line marks the position of the peaks at around 906 s.	65

5.6 Perturbations of the strain field by the AE events. The events from 890 to 922 s are divided into 4 clusters every eight seconds. The clusters are colored in blue, cyan, green and yellow. Events between 922 and 932 s (marked by orange dots in a and b) are not related to FO measurement due to lack of measurement then. Center of each cluster is marked by a filled square in (a and b). The change of the hoop strain field in these 8-second intervals are also computed and is averaged on a coarse grid on the sample surface with a grid-size of 16 mm. And the changes are plotted against their distances to the cluster center in the same time interval in (c-f). The color-coded solid circles are strain variations on the hanging-wall of the faults while the gray circles are on the foot-wall of the faults. The solid blue curves in (c-f) are linearly fitted in the log-log space.	67
A.1 Validation of the localization results with the adapted FaATSO package. The sensor positions are marked by circles and the ball drop positions from photos are marked by rectangles. The color-coded dots are localization results with FaATSO.	A-1
B.1 The flow chart that illustrates how the frequency spectra of the voltage signals and the theoretical displacement are computed.	B-1

Acronyms

Ada-AIC	Adapted Akaike Information Criterion
AE	Acoustic emission
AIC	Akaike Information Criterion
AR-AIC	Auto Regression - Akaike Information Criterion
CLVD	Compensated linear vector dipole
CT	Computerized tomography
DAQ	Data acquisition system
DC	Double couple
EGS	Enhanced geothermal system
FFT	Fast Fourier transform
FO	Fiber optics
FMD	Frequency magnitude distribution
FMM	Fast marching method
GR	Gutenberg-Richter
HF	Hydraulic fracturing
HS	Hydraulic shearing
IR	Instrument response
ISO	Isotropic
L2	Least square
LTA	Long time window
LVD	Linear vector dipole
LVDT	Linear variable differential transformer
Mc	Magnitude of completeness
ML	Local magnitude
MT	Moment tensor
Mw	Moment magnitude
RPMLab	Rock Physics and Mechanics Laboratory
SG	Strain gauge
STA	Short time window
UT	Ultrasonic tomography

CHAPTER 1

Introduction

1.1 Induced seismicity in the field

To reduce greenhouse gases and their negative impact on the environment, alternative and renewable energies, e.g. solar energy, wind turbines, hydropower and geothermal energy have become of interest to society. On top of this, Switzerland is also looking to phase out nuclear power in a safe, efficient and stepwise manner due to the Fukushima nuclear reactor crisis that followed the 2011 Tohoku-Oki Mw 9 EQ in Japan ([SFOE, 2018](#)). Among all the other alternatives, geothermal energy can contribute as an electricity provider (e.g. Enhanced geothermal systems, called EGS) and heat generator (e.g. shallow geothermal usage).

An unfortunate by-product of certain subsurface energy activities is anthropogenic earthquakes, also refer to as induced earthquakes. This phenomenon is a major obstacle for the safe extraction of geothermal energy and is a key factor that results in the decommissioning of viable projects due to unknown and unpredicted risks. During the Deep Heat Mining Project in Basel, 2006 and the geothermal project in St. Gallen, 2013, events with a magnitude of ML 3.4 and ML 3.5 respectively were induced and felt by the public. Following numerous studies, it was found that these were in fact induced earthquakes attributed to the injection of high-pressure fluids into the subsurface ([Deichmann and Giardini, 2009](#); [Bachmann et al., 2012](#); [Diehl et al., 2017](#)). The economic impact of the induced seismicity are often not so much the direct damages to buildings, but the impact on social and regulatory acceptance and subsequent loss of a license-to-operate ([Mignan et al., 2016](#); [Trutnevyyte and Wiemer, 2017](#)). In addition to geothermal energy exploration, induced earthquakes can be linked to a wide range of underground activities, like conventional and non-conventional hydrocarbon production, mining operations, water impoundment, CO₂ sequestration and natural gas storage operations, as in Figure 1.1. This makes mitigation through a better understanding of mechanisms leading to induced earthquakes emerges as a major new challenge to geoscience and the worldwide communities.

So far, it is known that induced earthquakes are the results of the sudden formation of new faults in intact rock or frictional instability resulting in the reactivation of pre-existing faults ([Villiger, 2015](#)). Faults are defined as fractures between two blocks of rock in geoscience. At macroscopic scale, the formation and propagation of faults can be derived using the Mohr-Coulomb failure criterion. The Mohr-Coulomb criterion dictates that faults fail or become reactivated when $\tau > C + \mu\sigma$, where τ is fault shear stress, C is cohesion coefficient, μ is friction coefficient and σ is fault normal stress (Figure 1.1a). During the extraction of geothermal energy, fluids are injected into rocks either to bring heat to the ground or to increase rock permeability. The fluids can be directly injected on to the existing fault planes (like in the Grimsel underground lab) or reach the fault planes along high permeability pathways (Figure 1.1b and c). σ in the above formula should, in these cases, be substituted by $\sigma_{eff} = \sigma - p$, where p is pore fluid pressure ([Garg and Nur, 1973](#); [Detournay and Cheng; King Hubbert and Rubey, 1959](#)). This mechanism is termed hydraulic shearing (HS) by [Villiger et al. \(2020\)](#). Faults can also form when tensile stress is larger than the tensile strength of rocks. When pore fluids are involved to achieve this failure condition (Figure 1.1d), the process is

called hydraulic fracturing (HF). While the Mohr-Coulomb failure criterion is useful for describing the macroscopic faulting ([Lockner and Beeler, 2002](#)), it is still unclear how the development of macroscopic faults is related to formation and coalescence of micro-cracks at subsidiary scales.

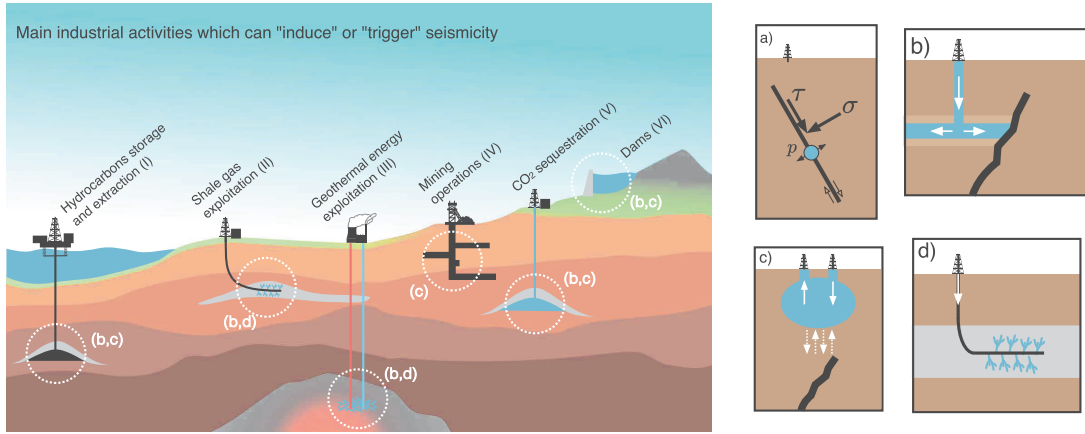


Figure 1.1: Industrial activities that can trigger seismicity from [Grigoli et al. \(2017\)](#). (a) This illustrates how fault shear stress τ , fault normal stress σ and pore pressure p on the fault are distributed on the fault. The injected fluids can reach the pre-existing fault through diffusion in rocks with relatively uniform permeability (b) or more effectively through a layer with high permeability (c). (d) This shows that fractures and seismic events can also be generated during hydraulic fracturing in intact rocks.

Apart from the mentioned mechanisms of rock failure under stress perturbation, understanding the quantitative nature of these perturbations is necessary for controlling the location and magnitude of induced earthquakes. The aforementioned external energy input via common methods, such as injection of water or gas, is indeed one of the most important cause of the perturbations. Source interaction is another critical physical process that might exist in both the propagation of the rupture front and the reactivation of existing fault. During the interaction, both seismic and aseismic processes are involved, governed by the first principle of thermodynamics. If the energy input from anthropogenic operations and material damage (e.g. generation of new surface and stress drop at the fault interface) cannot be consumed by the deformation of the materials and heating, kinematic energy will be released in the form of seismic waves. Otherwise, only aseismic deformation will be induced ([Hudson et al., 1971](#)). In case of fault reactivation, the above principle is specified as the friction laws. According to one of the most popular friction models, the rate-and-state model ([Dieterich, 1979](#); [Marone, 1998](#)), aseismic slip occurs at a rate-strengthening fault or the conditional stable creep of a rate-weakening fault; whereas seismic slip may only occur on a rate-weakening fault ([Rubin and Ampuero, 2005](#)).

While both seismic and aseismic deformation are present, the perturbation from aseismic deformation is hard to monitor at the field scale since the motions are too slow to be detected by most of seismic monitoring networks that exist to date. Evidence has been found that perturbations from aseismic slip during the fluid injection can be significant. For example, [Scotti and Cornet \(1994\)](#) has measured in an 800-meter-deep borehole that the distance of aseismic slip can induce an earthquake of magnitude larger than Mw 3 if released dynamically. [Guglielmi et al. \(2015\)](#) also detected considerable aseismic deformation that triggered earthquakes outside the predicted pressurized region in fluid injection ([Cappa et al., 2019](#)). At regional scale, aseismic deformation of the fault, i.e. where the slip rate between fault planes or the speed of rupture propagation is much lower than the speed of sound of the host rock, has also been found to be an important mechanism for energy dissipation ([Beroza and Ide, 2011](#)) and must interplay with the seismic component of deformation. A diversity in the mechanisms in which energy is dissipated has shown that slip

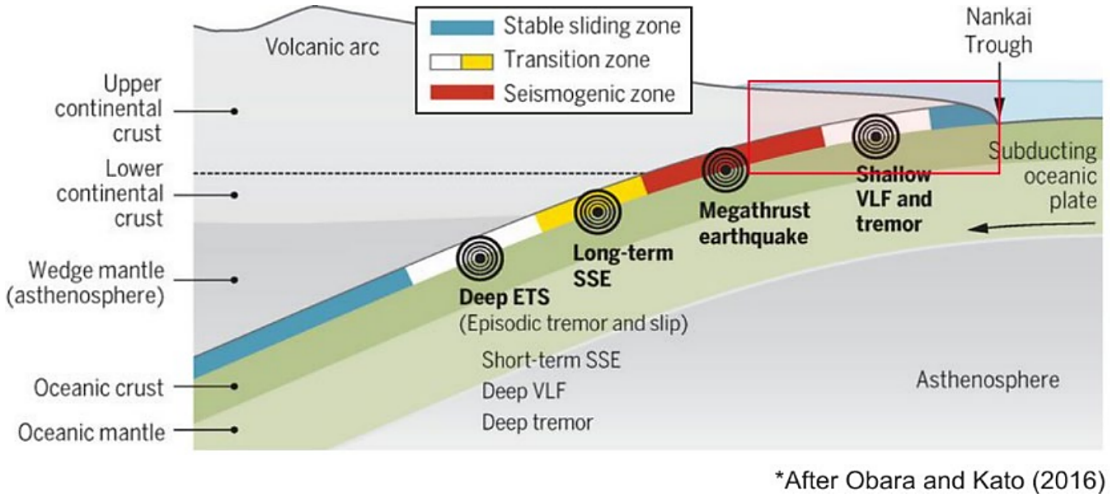


Figure 1.2: Adapted from [Obara and Kato \(2016\)](#). Schematic depiction of seismic and aseismic slip locations on the Nankai subduction zone. Red boxes depict the approximate environmental condition attainable in LabQuake facilities.

behavior along natural faults can occur in various forms, for example deep episodic non-volcanic tremor (NVTs) ([Obara, 2002](#)), low-frequency earthquakes (LFEs) ([Shelly et al., 2007](#)), very low frequency earthquakes (VLFs) ([Ito et al., 2007](#)), episodic tremor and slip (ETS) ([Rogers and Dragert, 2003](#)), and long-term/short-term slow slip events (SSEs) ([Kawasaki et al., 1995](#)), which occur at various time and length scales ([Peng and Gomberg, 2010](#)). Figure 1.2 schematically shows how different types of deformation can coexist in a subduction zone.

Aseismic deformation is not only observed across scales but has been found to play significant role in predicting the largest earthquake size ([McGarr, 2014](#); [Bhattacharya and Viesca, 2019](#); [Guglielmi et al., 2020](#); [Cornet, 2016](#)). [Galis et al. \(2017\)](#) proposed that it controls the injection-related seismicity through runaway rupture propagation and explains it with the rate-and-state model. Detailed understanding of the process requires better subsurface characterization of fault populations, statistical characterization of material and rheologic properties and more accurate estimates of the heterogeneity in stress, pressure and thermal fields ([Bhattacharya and Viesca, 2019](#)). However, although the above complexities are most relevant to geothermal exploration at field scale, physical processes at smaller scales are also important for revealing how large earthquakes are triggered.

1.2 Down-scaling from field to laboratory

To unravel the behavior of earthquakes and faulting at various scales, experiments in the larger setting than the traditional laboratory have been performed. Recent experiments conducted by the SCCER-SoE in the Grimsel underground lab in 2016 and 2017 ([Gischig et al., 2018](#); [Amann et al., 2018](#)) targeted $20\text{ m} \times 20\text{ m} \times 20\text{ m}$ foliated, crystalline rock volume intersected by two distinct fault sets and delivered unique multi-parameter observations (strain, pressure, flow) from a series of hydraulic stimulations. The project targeted well mapped faults and stimulated them while monitoring high precision hydraulic and mechanical characteristics while attempting to better understand their influence on the seismogenic expression of the rock mass. The findings are not yet fully understood but they highlight that, in the seismogenic response at scales of meters, heterogeneity is to be expected even in a rock mass on the order of 8000 m^3 with common geological structures. Coupled aseismic-seismic deformation has also been observed ([Villiger et al.,](#)

2020). These decameter-scale stimulations are crucial in understanding the bulk hydro-mechanical response of faults in relation to small scale seismicity and can potentially reveal effective methods to control induced seismicity (Villiger et al., 2020).

Recent bench-scale laboratory studies by Selvadurai (2019) found that many of the models used to quantify seismic source properties are scale invariant (Goodfellow and Young, 2014; Okada, 1992; McLaskey et al., 2015). This indicates that seismicity may be a phenomenon that is capable of linking physical scales and legitimizes the hypothesis that controlled and repeatable laboratory tests, in a traditional setting, can provide a greater understanding of the complexities associated with fluid injection and induced seismicity.

Studies at the laboratory scale have begun to highlight important mechanisms that are involved in the preparation phase of the major shock during sample failure. They are described as the progressive localization of strain (Goebel et al., 2013), the effect of stress heterogeneity due to fault roughness, evolving seismicity, dynamic rupture propagation (Goebel et al., 2017) and dependency of fault properties on temperature (Wang et al., 2020) and pore fluids (Dresen et al., 2020).

In these experiments, aseismic deformation of the samples is generally measured by pairs of strain gauges while locations and occurrence rate of micro-seismic events are obtained by recording dynamic motion with piezoelectric sensors at the surface of rock samples (Passelègue et al., 2017). These measurements are typically restricted by spatial and temporal deficiencies of the used apparatuses.

In seismic analysis, the frequency spectra of most piezoelectric sensors' instrument responses (IRs) have very narrow band. Therefore, correct shapes of displacement waveforms and magnitudes of seismic events are unattainable, significantly impeding the accurate characterization of source mechanisms of events.

In aseismic analysis, traditional strain gauges are only capable of recording aseismic movement at a few scattered points. Thus, strain field of the entire sample is rather poorly constrained, especially when strong fault heterogeneity is involved.

These limitations in the acquisition of seismic and aseismic measurements described above prevented us from precisely understanding how micro-cracks nucleate and coalescence into macro-fractures.

1.3 Aims of this study

Since the LabQuake facility only became operational at the beginning of this master thesis project, data processing tools that are adequate for the state-of-art equipment were not available. The primary goal of this study is, therefore, to develop the toolbox to process the seismic data and to combine it with cutting edge measurement from the fiber optics sensors implemented for the first time. A few pilot experiments will be conducted to test the tool box. Data from the experiments will also be used to re-examine the seismic and aseismic behaviors in the preparation phase of major failure. To the knowledge of the author, this is the first time that the seismic information can be related to non-linear strain behavior without treating the sample as a single force member, but as a fully deformable body quantified with the dense fiber optics measurements of the strain field on the periphery of the sample. Unstructured stress inversion in 3D geometry at laboratory scale is also preliminarily examined for the first time.

The results of the study were due to collaborative efforts with University of Applied Sciences of Eastern Switzerland (OST), the Swiss Seismological Service and were performed in the Rock Physics and Mechanics Laboratory (RPMLab) at ETH Zurich. This enabled the successful combination of acoustic emission and fiber-optic technology and will be summarized in Section 2. Three sets of compression tests with confining pressure on the Rotondo granite were conducted and the procedures of the experiments, as well as the methods to processing seismic and aseismic measurement will be described in Section 3. Results of each experiment will be shown in Section 4. Based on the results, the correlation between the heterogeneous strain field and the seismicity during the failure of the rock will be discussed in Section 5. Observations of this study will be summarized in Section 6, together with the outlook on the exciting works that can be extended from this thesis.

CHAPTER 2

Background

This section tries to make a summary on how the experiments conducted in this thesis fit in the development of the study on laboratory seismology and on how they are enabled by the fundamental work that have been conducted in RPMLab. In Section 2.1, theoretical and technical advancing in the laboratory seismology is introduced. Previous understandings of the seismic and aseismic processes before the failure of the rock based on the observations at the lab-scale are also reviewed. In Section 2.2, after commenting on the previous analysis, significance of the efforts in this thesis will be elaborated. Support from the previous study in the RPMLab is described in Section 2.3 and 2.4. While the former section focuses on the study of the Rotondo granite from which the samples in our experiments are extracted, the latter section introduces the experimental facilities in the RPMLab.

2.1 A historical recap on acoustic emission testing

Mogi (1966) took the initiative to test constitutive relationships of rocks under triaxial stress field. In the same year, Brace and Byerlee (1966) noticed the general stress-axial-strain and stress-volumetric-strain relations during the evolution of an intact granite to failure. The volume of the sample would first contract before it expands when approaching failure. At that time, it was already known that failure of sample was preceded by small cracking at around half the failure stress, suggesting the correlation between the dilation and the pre-failure cracking. However, measurement on cracks inside the sample was only made possible by Scholz (1968). He attached a single piezoelectric transducer to the sample and collected the electronic signals triggered by the dynamic displacement field emitted from seismic sources. The radiation of kinematic energy in the damage of solid materials is termed Acoustic Emission (AE). This term will show up many times in the thesis and will be the major method for analyzing the seismicity. Scholz's experiment on the Westerly granite showed that the rate of acoustic emission was closely related to the anelastic volumetric strain.

Since then, studies on the acoustic emissions have been further developed with the installation of more sensors, the improvement on the sensor techniques and the efforts on decreasing the background mechanical and electrical noise level. More sensors allowed for the localization of micro-seismic events, which further extended the study of acoustic emissions from temporal scale to both temporal and spatial scales (Lockner, 1993). AE hypocenters have been determined with a location error of a few millimeters (Lei et al., 2000a,b; Stanchits et al., 2006; Benson et al., 2010). Using the first motion polarization of some events, the focal mechanisms have also been constraint (Manthei, 2005). Recently, attempts on inverting the moment tensors using the amplitude information of the waveform have also been made. Li (2015) used the maximum amplitude of the recorded voltage, whereas Kwiatek et al. (2016) used the P-wave omega computed from the area below the first lobe of the waveform. However, due to the resonant-type AE sensors they used, only the so-called AE magnitude scales could be used to quantify the events and its true relationship to the physics-based

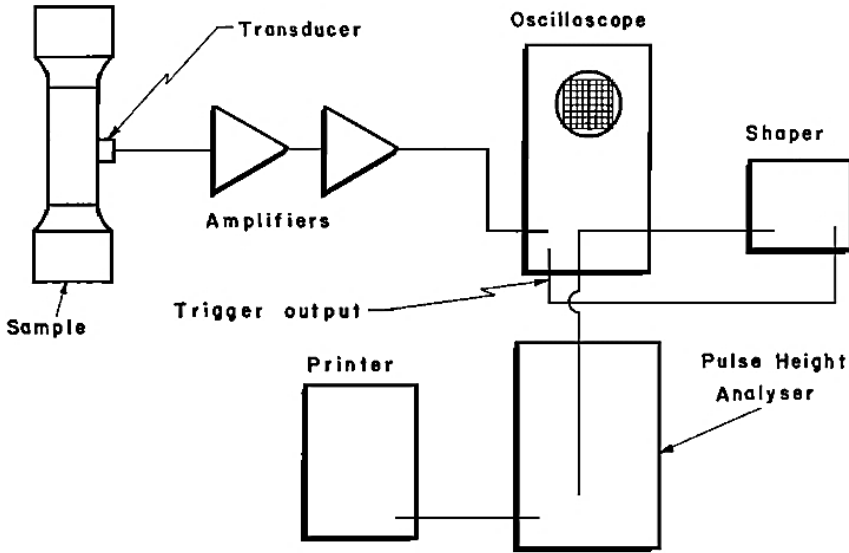


Figure 2.1: Adapted from Scholz (1968). A schematic diagram that shows how Mogi (1966) recorded the acoustic emission signals using one piezoelectric transducer.

moment magnitude scale (Aki, 1984) is unknown.

With the improvement on the experimental equipment, more and more advanced concepts in seismic statistics at the field or regional scales can recently be examined at the lab-scale. The power law observed in magnitude distribution of earthquakes at regional and field scales is the Gutenberg and Richter (GR) relationships Gutenberg and Richter (1944). Similar distribution seems also exist at the lab-scale and efforts have also been made to explain the b-values in GR relationships with a fractal distribution of the grain size and the pre-existing cracks (Main, 1996; Main et al., 1989; Sun et al., 1991; Lei et al., 2005). The temporal distribution of the foreshocks and aftershocks have been observed to follow similar relationships modified from Omori's law (Utsu, 1961; Utsu and Ogata, 1995). In analogy with the percolation phenomena due to the fractal complexities during the failure of rocks, such power laws in time domain may be explained with the concept of critical point behavior (Yamashita and Knopoff, 1989; Sornette and Sornette, 1990; Yu et al., 2004). In terms of the spatial distribution, the fractal dimension of rocks has been applied to explain the locations of AEs. It can be obtained from the generalized correlation-integral proposed by Kurths and Herzel (1987). According to some previous studies (Hirata et al., 1987; Lei et al., 1992; Lei and Satoh, 2007), localization of AE activity leads to a decrease of fractal dimension, and the latter was thus expected to be a possible indication of approaching failure.

The above quantification of seismic statistics lays the foundation for linking seismic and aseismic deformation. According to the previous aseismic measurements, a two-stage process, as shown in Figure 2.2a, has been observed. As the shear stress (F_s) on the fault increases, a series of small stress drops due to progressive micro failure in slow stable sliding is observed. When F_s increases to a certain threshold, dynamic rupture of the fault occurs accompanied by a large sudden stress drop. Such two-stage process has been both modeled (Ohnaka, 1992) and observed experimentally in stick-slip tests (Rubinstein et al., 2007). Statistical analysis on seismicity shows that such damage evolution across the fault zones and surrounding wall rocks is manifested by precursory decrease of seismic b-values (Figure 2.2b). B-value is also strongly dependent on rock properties. First, the b-value was found to be a function of grain size. A finer grain size tends to link with a higher b-value (Lei et al., 2005). Second, according to the damage laws, b-value ranges from 0.5 to 1.5 and is inversely correlated with the mean crack length. It was also found that samples of

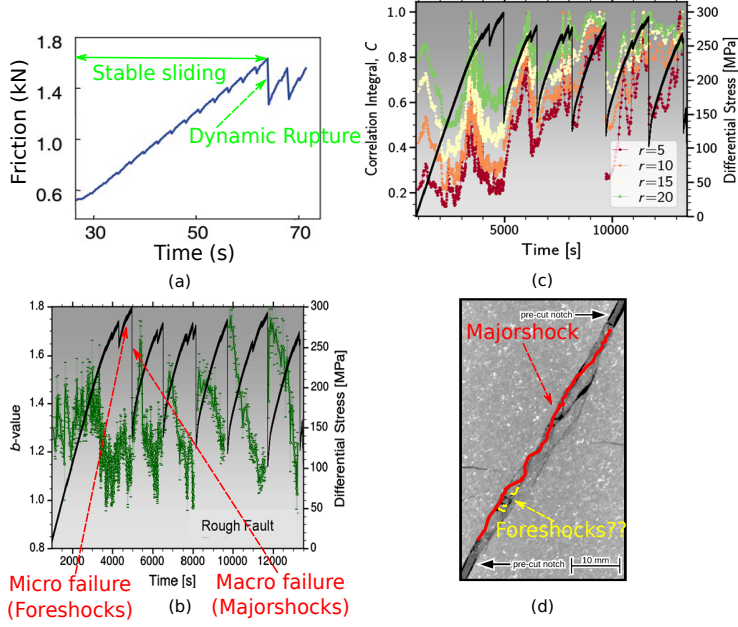


Figure 2.2: (a) Transformation from relatively smooth increase of frictional force along the fault in slow stable sliding to a sudden drop when dynamic rupture occurs (Rubinstein et al., 2007). Before each large stress drop, precursory decrease of seismic b -values (b) and spatial correlation dimensions (c) are systematically observed (Dresen et al., 2020). (d) Complex fault geometry and heterogeneous mechanical properties across the fault zone. The macroscopic failure induced in the majorshock is marked by a red curve and some of the micro failures that possibly occur in foreshocks are marked by yellow curves.

unfavorably oriented foliation and optimally oriented foliation shows a primary b -value of about 1.5 and about 1.0, respectively. The spatial distribution of seismicity can be quantified by a precursory decrease in spatial correlation (fractal) dimensions (Figure 2.2c) (Dresen et al., 2020). However, it is also noted that the chance to observe decreasing fractal dimension depends on the number of foreshocks which is somewhat determined by the critical size of the fault nucleation zone (over which the rock fails dynamically), as well as the growing velocity of the fault. In cases of a small nucleation zone or fast-growing velocity, a smaller number of foreshocks are insufficient to cause a notable change in fractal dimension (Lei et al., 2005).

Physics behind the variation of statistical variables has also been studied. According to Scholz (2019), preparation phase characterizes progressive strain localization that results in the formation of single or multiple slip zones embedded in less deformed damage zones. The key factor that controls strain localization is the complex fault geometry and heterogeneous mechanical properties across the fault zone, as shown in the CT scan image of a fault zone in Figure 2.2d. Such fault heterogeneities control inter-seismic loading and rupture dynamics, leading to heterogeneous distribution of slip, slip rate and stress drop (Goebel et al., 2013, 2017). In addition, existence of pore fluids can further increase the complexity of the fault nucleation and the induced seismicity (Shapiro et al., 2003; Miller et al., 2004). Experiments have been conducted to study how pore fluid pressure and injection rate influence stability and stick-slip behavior of faults (Xing and Zhu, 2019; Wang et al., 2020) and how fluid pressure is changed due to frictional heating and shear dilatancy (or compaction) (Proctor et al., 2020). However, none of them has managed to relate the observed phenomena in fluid injection to spatial and temporal evolution of micro-crack coalescence, making detailed description of what happened at the fault zone impossible.

2.2 Proposed developments in AE methodology

The novel LabQuake facilities located in the RPMLab at ETH Zurich allows us to take a step forward. A workflow to invert moment tensors and local stress field of seismic sources is developed and described in Figure 2.3.

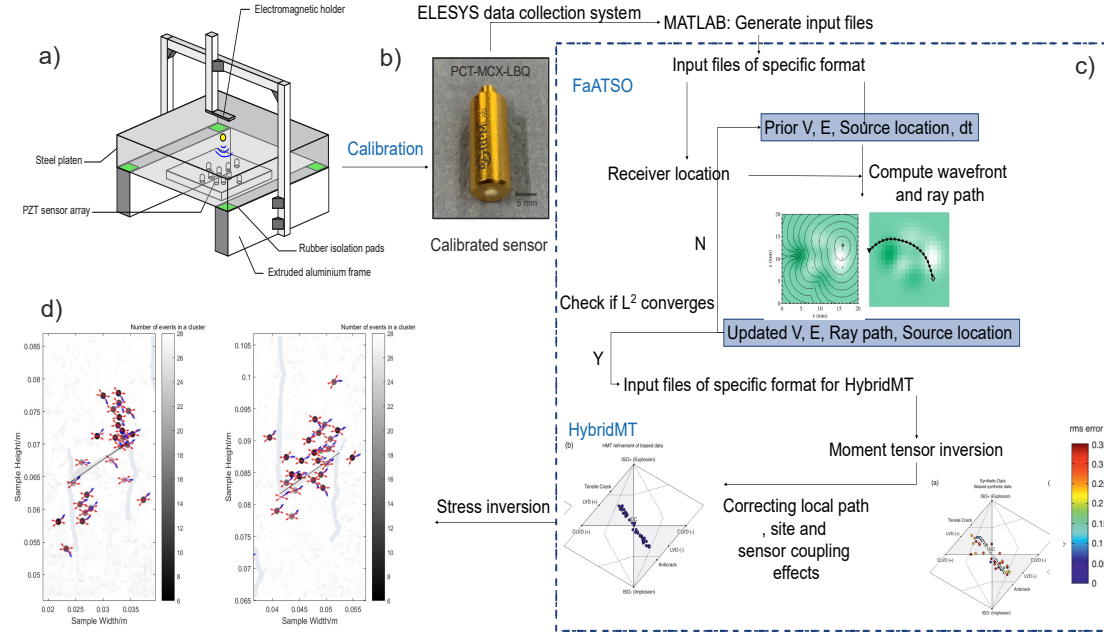


Figure 2.3: (a) A general schematic of calibration station, which consists of electromagnetic holder, steel balls with different diameters, steel transfer plate, PZT sensor array, extruded aluminum framework, etc (Wu et al., 2020). (b) is the calibrated PCT-MCXLBQ sensor. (c) is modified from Brantut (2018) and Kwiatek et al. (2016), is the framework of the package that combines FaATSO and HybridMT to do source relocation, rock tomography, moment tensor and stress inversion. (d) This shows the verification of stress inversion. Normal vectors (blue arrows) of the clustered events (circles) and the local weak planes (red arrows) predicted by stress inversion results and Mohr-Coulomb's law, with internal friction angle set to 44° . Colored circles are nodes of each cluster. The color indicates the number of single events in each cluster (darker color corresponds to more single events). And the zig-zag curves at the tips of initial flaws are macro-cracks observed in the experiment.

An important improvement on the equipment is the use of the conical-shaped PCT-LBQ sensors (Figure 2.3b) in recording AE signals. The sensor has a conical head made of PZT (lead-titanate-zirconate) crystal, which is pressed against the surface of the specimen. Seismic events occurring on the surface or within the body create elasto-dynamic stress waves, that propagate through the body generating a wave field that can be mathematically computed using Green's function solutions. As stress waves pass the PZT crystal contact point, it compresses and converts mechanical energy into electrical energy. Based on this mechanism, PCT-LBQ sensors are specifically designed for LabQuake environment and features broadband instrument frequency response (from 70 kHz to 1.5 MHz) and little distortion to the physical interpretation of the wave field from sources with incidence angle as large as 60 degrees.

A package is developed to obtain highly accurate amplitudes and shapes of waveforms based on the calibration procedures developed at the RPMLab (Wu et al., 2020) using ball drop or capillary fracturing experiments. Setup of the calibration station is shown in Figure 2.3a. The force-time function of both sources is highly repeatable. This enables us to absolutely calibrate sensors by averaging sensor responses in a few ball drop trials.

The calibrated sensors can be later used to collect waveforms from induced seismic events using an Elsys acquisition system. A key measurement extracted from the waveforms is the absolutely calibrated P wave. Its amplitude and arrival time can be taken as the input for source localization, tomography, moment tensor inversion and stress inversion. Detailed workflow of the inversion is shown in Figure 2.2c. Previous experiments have observed that intact rock samples will become more heterogeneous and anisotropic as micro-cracks nucleates and coalesces (Brantut, 2018). This can significantly change the Green's function from sources (seismic events) to AE sensors. To increase accuracy in source relocation in the rock samples whose mechanical properties vary in time, we have used a pre-existing C++ package FaATSO (Fast Marching Acoustic Emission Tomography using Standard Optimisation) Brantut (2018). FaATSO is capable of performing seismic tomography and source localization simultaneously in heterogeneous and anisotropic media, providing the ray path and the location of each single seismic event and the velocity model of the rock sample.

Beyond locations, focal mechanisms and magnitudes of the events can provide information about the source physics and local stress field. The pre-existing moment tensor inversion code HybridMT developed by Kwiatek et al. (2016) is employed, which inverts for the moment tensor solution in heterogeneous anisotropic rock samples. It can also partially correct errors introduced from local path, site and sensor coupling effects in moment tensors inversion. Additionally, the inverted moment tensors of seismic events can be used to constrain local heterogeneous stress field using a third package that applies stress inversion techniques by Li and Du (2020). The seismic events are first clustered according to their spatial distribution. Then, stress field around each cluster is estimated using each single event in the cluster. The reliability of the stress inversion package has been verified by the author against experimental results from Moradian et al. (2016) and is demonstrated in Figure 2.3d. They provide the possibility of linking seismic signals to stress fields across the fault zones and the results will be compared to the strain field measured by fiber optics cables at the sample surface.

2.3 Rotondo granite

The rock samples used in the experiments of this thesis are cut from the Rotondo granite in the characterization/monitoring borehole 2 (CB/MB 2) drilled from the Bedretto Underground Laboratory for Geosciences and Geoenergies (BULGG) at tunnel meter (TM) 2043.3. The geological map of the tunnel is shown in Figure 2.4. The Rotondo granite, which defines ~80% of the lithology in the Bedretto tunnel, consists mainly of an equigranular, fine-grained granite (Labhart, 2005). However, a porphyritic granite with sharp contact to the equigranular granite is exposed in the central part of the Bedretto tunnel (Schneider, 1985). Uranium–lead (U-Pb) dating with zircons from a single site suggests an intrusion age of 294 ± 1.1 Ma (Sergeev et al., 1995). The main part of the Rotondo granite is located in the central part of the Gotthard massif and has an extent of about 25-30 km. Four granite bodies further to the northeast are also traditionally classified as Rotondo granite, although they are not connected at the surface (Labhart, 2005).

2.3.1 Mineralogical composition

According to Rast (2020), the geology around the borehole CB/MB 2 is dominated by the equigranular granite, one of the two major types of the Rotondo granite. It is equigranular, fine-grained granite ('aplitic granite') with a mineral content of quartz (qz) (25-35%), alkali feldspar (Kfs) (20-40%), plagioclase (Pl) (10-25%), biotite (Bt) (3-8%) and garnet (Grt), phengite, chlorite (Chl),

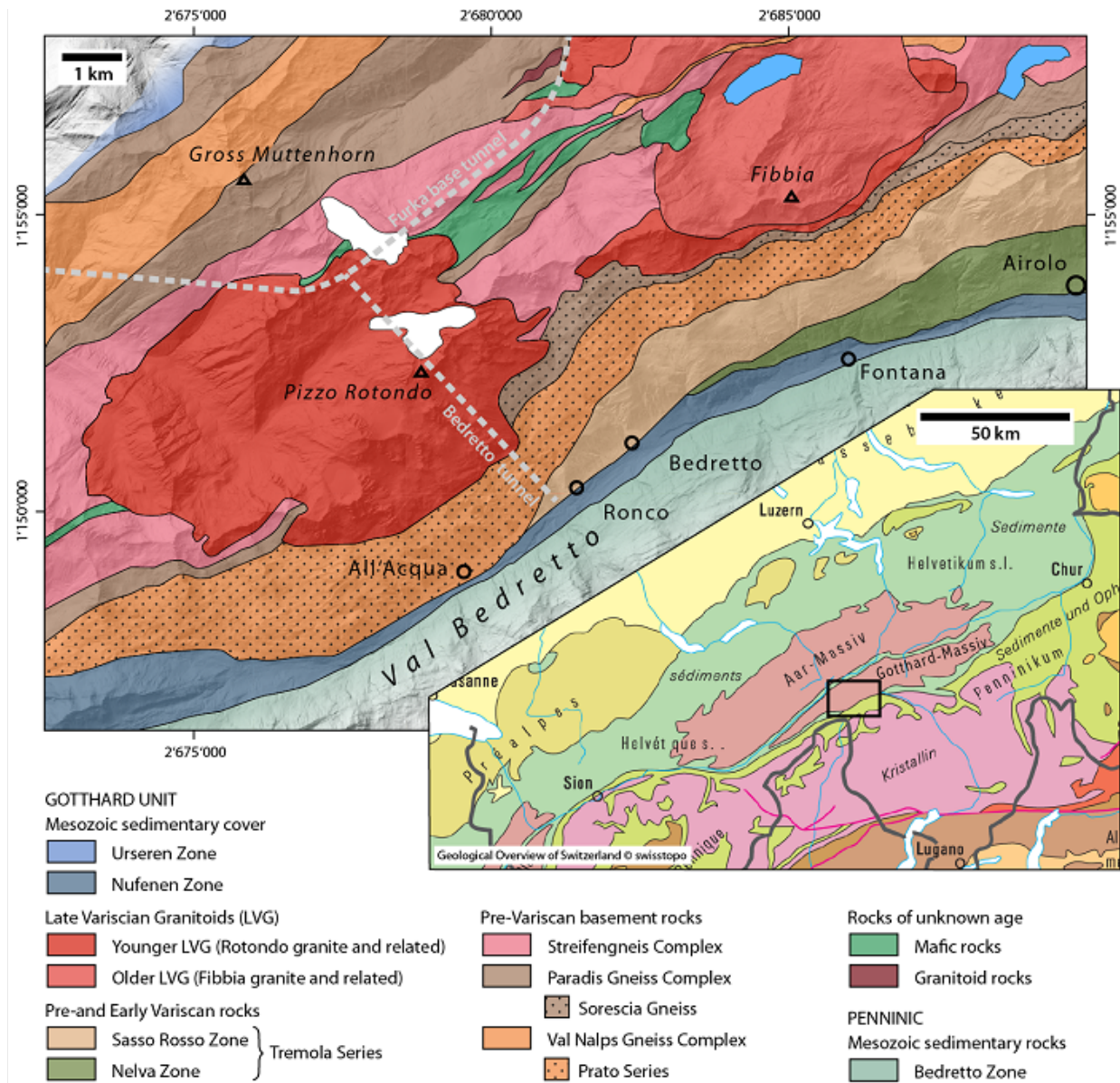


Figure 2.4: Adapted from Hafner et al. (1975); Berger et al. (2016); Rast (2020). Main map: geological overview of the area around the Bedretto tunnel (the dashed gray curve). Coordinates outside of the map correspond to the Swiss Grid (CH1903++). Large-scale map: tectonic overview of the Central Alps, the black rectangle represents the cutout of the main map.

epidote (Ep), apatite (Ap) and zircon as accessory minerals (Hafner, 1958; Steck, 1976; Labhart, 2005). However, the granite is not homogeneous over its entire extent, as shown by a zone of biotite-rich granite with feldspar porphyroclasts in the Bedretto tunnel.

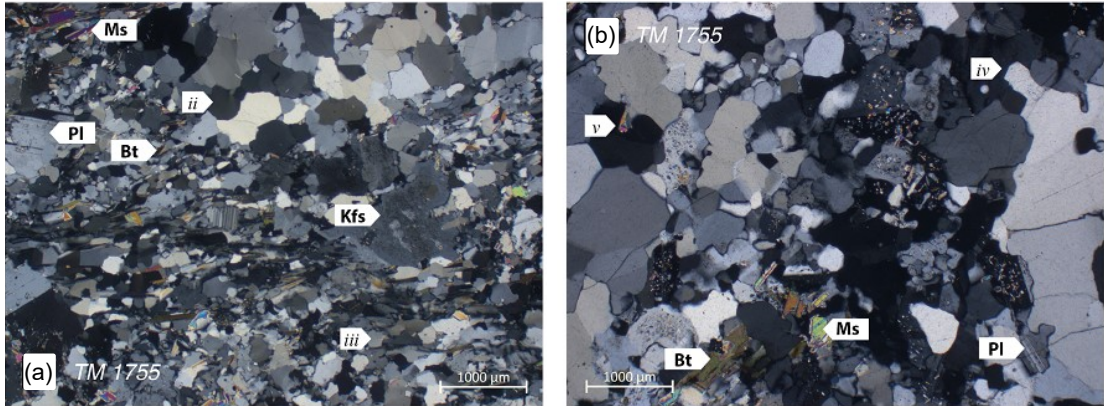


Figure 2.5: Adapted from [Rast \(2020\)](#). Thin section cutouts of the equigranular Rotondo granite used in our experiments, crossed polarized light in all photomicrographs. (a) shows muscovite (Ms), Pl, Bt, Kfs and (b) shows Ms, Bt and Pl.

Figure 2.5 shows photomicrographs of thin sections from the Rotondo granite. Thin sections of the granite have usually an equigranular to inequigranular, interlobate texture. Three types of quartz with different grain size ranges and different grain boundary shapes occur. Alkali feldspar in the granite forms grains in the mm-range, which have anhedral shapes (Figure 2.5a). Plagioclase commonly forms anhedral grains in the mm-range, and lamellar twinning is widespread (e.g. Figure 2.5). Biotite crystals form ~ 1 mm wide sub- to anhedral grains. The shapes and mechanical properties of each type of minerals, as well as the cohesion strengths between the grains determines the mechanical heterogeneities of the sample and will influence where micro-cracks form and where seismic waves are emitted. According to [Manthei and Plenkers \(2018\)](#), the seismic events at this scale typically have the magnitude of around Mw -8.

2.3.2 Mechanical Properties

Physical and mechanical properties of the Rotondo granite have been systematically studied with 28 samples a 100 m long cavern at distances between 2000 and 2100 m from the southern entrance of the Bedretto tunnel, that is a 5.2 km long access gallery to the Furka railway tunnel and summarized by [David et al. \(2020\)](#). Table 2.1 lists the properties that are important for seismic and aseismic deformation of the dry rock sample. The anisotropy factor here is calculated for each sample as the difference between the maximum and minimum velocities over the average velocity of the three directions.

2.4 Experimental Facility

2.4.1 Calibration station

The instrument responses (IRs) of the PCT-LBQ sensors are obtained from the surface displacement at the bottom of the steel plate excited by an active source (ball drop or capillary fracturing)

Table 2.1: Physical and mechanical properties of the Rotondo granite under zero confining pressure (David et al., 2020).

Properties	Values
Density (kg/m ³)	2606
Porosity (%)	1.75
P-wave velocity (m/s)	3501 ± 301
S-wave velocity (m/s)	1785 ± 117
P-wave anisotropic factor (%)	20 ± 9
P-wave anisotropic factor (%)	10 ± 7
Dynamic Young's modulus (GPa)	22.6 ± 2.7
Dynamic shear modulus (GPa)	8.3 ± 1.1
Dynamic bulk modulus (GPa)	27.3 ± 3.7
Dynamic Poisson's ratio (-)	0.36 ± 0.03

at the top of the plate. The plate (35 cm × 35 cm × 5 cm) is held by an extruded aluminum frame and is assumed to be isotropic and homogeneous. Small nitrile butadiene rubber (NBR) pats, which have low mechanical impedance (~1/11 of that of steel), were used to block the re-fraction of the elastic wave into the aluminum frame. The upper crossbeam of the frame is built to hold the structure that applies the active sources. In the case of the ball drop experiments, an electromagnetic holder can be mounted on it. The holder holds balls of different sizes until the power is turned off. In the case of the capillary fracturing experiments, the beam holds a force transducer that is moved up- and downward by tuning a micrometer screw (see Figure 2.6c). As it moves downward, the loading pin attached to the transducer can apply force to break a thin-walled capillary tube (0.3 mm in diameter and 0.01 mm thick, Freiderick and Dimmock, Inc.) placed on the top surface of the steel plate.

2.4.2 LabQuake

LabQuake is designed for the geo-mechanical testing of both soft and hard rocks with a number of unique capabilities targeted at enhancing laboratory seismology. Its loading cell is depicted in Figure 2.7. LabQuake can be used for systematic experimental investigations of the effects of pore-fluid variation in fractured media by measuring poroelastic, mechanical, hydraulic and thermal properties, as well as acoustic emissions of intact and fractured rocks, considering various stress regimes and different fracture orientations representative of the upper crust conditions. The system will have the ability to achieve confining pressures up to 170 MPa, pore pressures up to 170 MPa, and exhibit a minimum frame stiffness of 2500 kN/mm. All tests will be adaptable to environmental conditions with temperatures ranging from room temperature to 170 °C, controlled by an internal heating coil. Highly dense sensor network in the apparatus (will be introduced in Section 3) combined with improved processing workflows (Figure 2.3) will greatly improve precision, accuracy and completeness resulting hopefully in the highest-fidelity seismic lab data to date, allowing us to overcome many of the limitations of past studies and enable new kind of research –bridging seismology across scales. Intact (Figure 2.7-I), naturally fractured (Figure 2.7-II) and saw-cut rock samples (Figure 2.7-III) are going to be tested under several different loading schemes, e.g. confined compression and unconfined hydro-fracturing (Villiger, 2015). The thesis is going to focus on the failure of intact rock sample in the confined compression test.

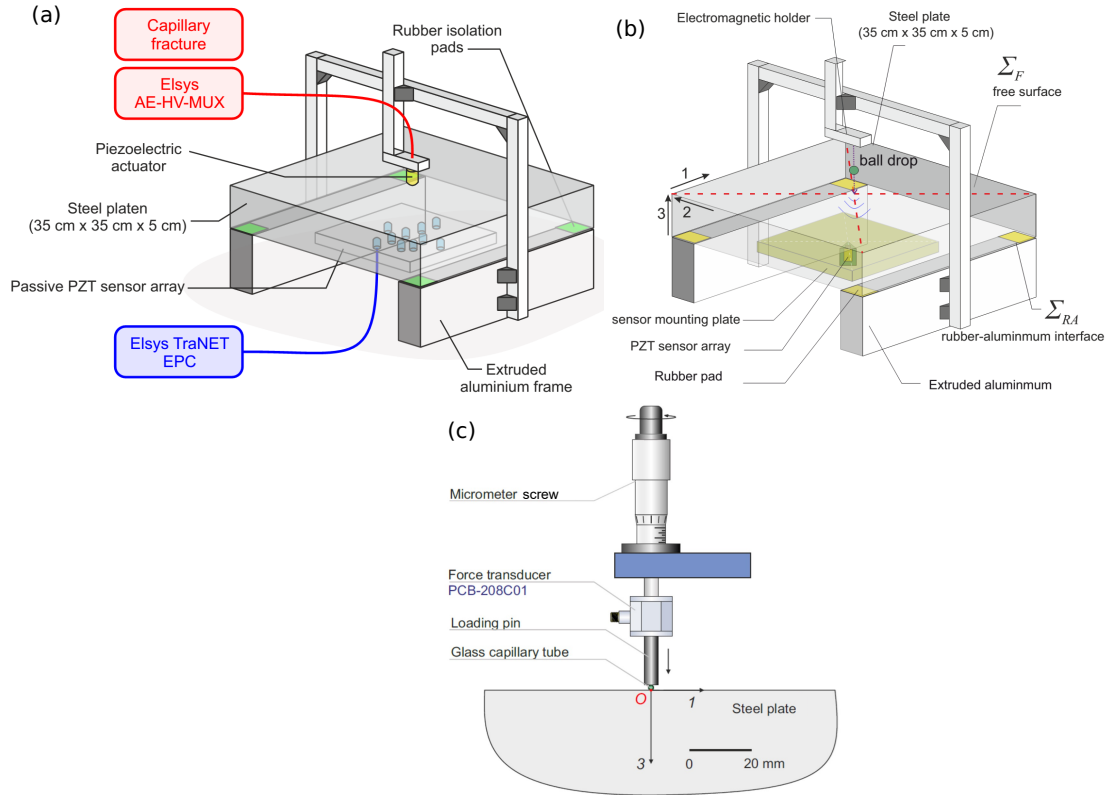


Figure 2.6: Adapted from Wu et al. (2020) and Selvadurai et al.. Structure of the calibration station using capillary fracturing (a, c) and ball drop (b).

2.4.3 Elsys data acquisition system (DAQ)

A 32-channel data acquisition system was purchased from the Swiss Company Elsys AG and is operational. As shown in Figure 2.8, the hardware of the system is composed of the TraNET EPC DAQ module, the AE-AMP module and the AE-HV-MUX module. The TraNET EPC DAQ module is characterized by TPCE-2016-4s high precision high speed (up to 20 MHz) digitizer modules (Elsys, 2017). The AE-AMP module is an amplifier with selectable gains among 0, 20, 40 and 60 dB. The amplifier will also filter the signals with a low cut at 5 kHz and a high cut at 5 MHz, 3 MHz, 2 MHz and 700 kHz respectively for each gain with a -3 dB fall-off. The high voltage pulser HVP1000/200 has been designed to drive special Piezocomposite Actuators or other suitable loads with very high charging currents for pulse-wise operation in the square-wave mode. The output amplitude ranges between 40 and 1000 V.

The software of the Elsys system includes TranAX and AE-LabAX. The TranAX 4.1 is the tool for controlling TraNET and TPCE for measurement, data acquisition tasks and signal pre-processing. To control the pulser and to process the AE data in real time, AE-LabAX is required.

2.4.4 Acoustic emission sensors

Figure 2.9 shows the cross-section of the custom-built PCT-LBQ acoustic emission sensor, which follows the design of other point contact sensors (Eitzen et al., 1981; Eitzen and Wadley, 1984; Glaser et al., 1998; Proctor et al., 2020). The crystal in the sensor uses a 2.5 mm tall truncated

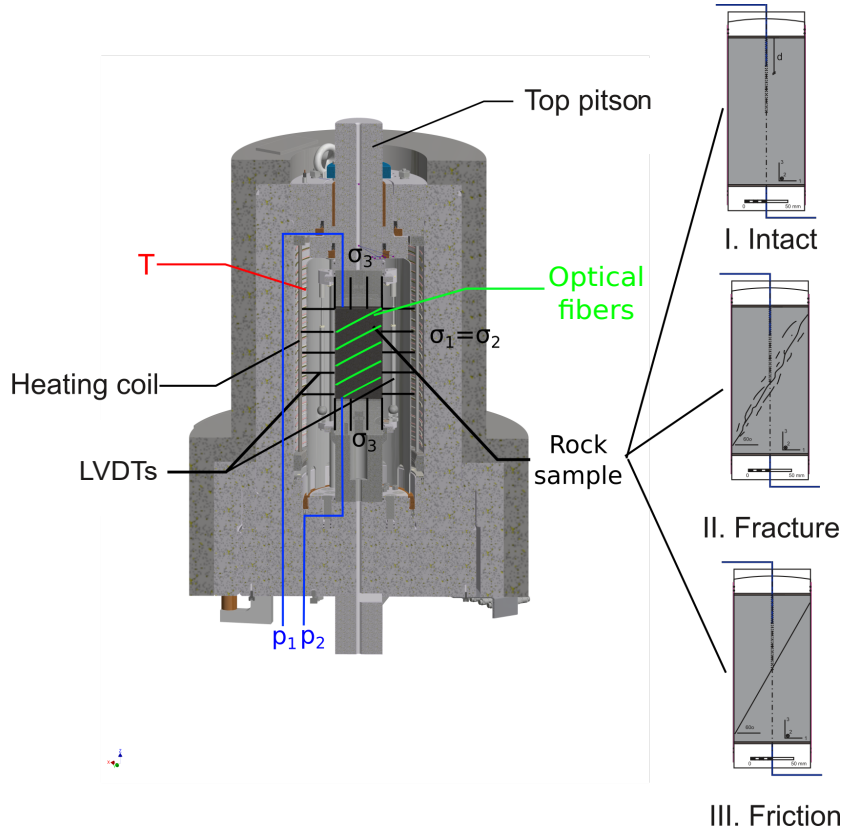


Figure 2.7: Experiment setup that can be implemented in the LabQuake facilities. This shows how fluids are injected, how temperature, axial stress and confining pressure are loaded on the intact sample (I), naturally fractured sample (II) and saw-cut sample (III).

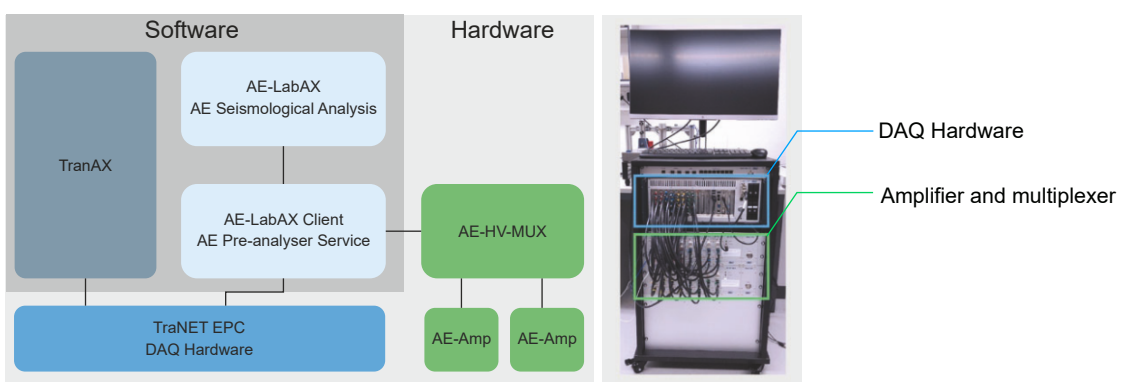


Figure 2.8: The photo of the Elsys DAQ (a) and the schematic diagram that shows the components and how they are connected (b).

cone of PZT-5a (a lead-zirconate-titanate composite). The tip of the cone (or aperture) is 1.5 mm in diameter with a base of 6.5 mm diameter. The crystal geometry follows that detailed by the National Institute of Standards and Technology (NIST), which is widely used for wideband acoustic emission sensors ([Eitzen and Wadley, 1984](#); [Proctor et al., 2020](#)). This design has two advantages. First, it minimizes the aperture effect by keeping the contact tip small and thus resolves the higher frequencies of the seismic waves. Second, the conical shape also reduces the normal modes common to disc shaped PZT elements due to its sensitivity to motion along the axial direction. The backing mass was also carefully chosen since it is a critical component of the acoustic emission sensor ([Glaser et al., 1998](#); [Proctor et al., 2020](#)). It was fabricated from brass following the methods of [Glaser et al. \(1998\)](#) and was machined from a rod of 7 mm diameter with a height of 15 mm. Multiple cuts were taken on the back end of the mass with respect to the longitudinal axis, which reduced symmetry and prevented direct reflections from re-exciting the piezoelectric element ([Proctor et al., 2020](#)). The backing mass was bonded using a thin layer of two-component silver conductive epoxy resin adhesive (APS EP-01A/B) that had a resistance of 0.3×10^{-4} to $1 \times 10^{-3} \Omega\cdot\text{cm}$. The conductive epoxy resin was used in other assembly processes including: connecting the radio frequency (RF) pin (Coaxial PCB MCX-50-0-19/111-N-1) to the backing mass and connecting the thin nickel face plate (0.03 mm thick) to the tip of the piezoelectric element and the steel housing canister and the amount used was reduced to minimize the gaps that completed the electrical circuit; this was found to reduce the noise floor of the sensors. The outer casing was threaded (M14 × 1.25) and was used to mount the sensors to the array on the bottom of the steel plate.

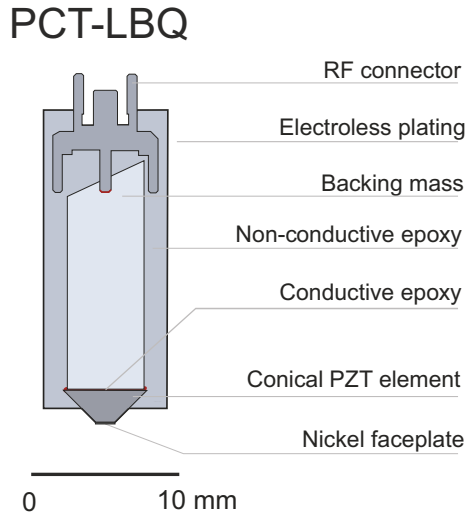


Figure 2.9: Adapted from [Selvadurai et al.](#). The schematic diagram that shows the inner structure of the PCT-LBQ piezoelectric sensor used in the experiments.

2.4.5 Fiber optics technology

The most commonly used strain measurement technologies are the linear variable differential transformer (LVDT) and the strain gauge (SG). However, these point measurement methods fail to identify strain heterogeneities, resulting in the dependence of the interpretation for rock's mechanical behavior on the position where the sensors are attached ([Salazar et al., in preparation](#)). Such deficiencies prompted us to apply distributed strain measurement based on the fiber optics technology to triaxial tests on rocks. The fiber optics interrogators used in the present experiments were developed following the Rayleigh-based optical frequency domain reflectometer (c-OFDR)

from Luna Innovation (OBR 4000). The OBR is able to measure with a spatial resolution of 10 micrometers and a gauge length of 2 mm. In practice, we have one measurement every 2 mm. Two types of fiber optics coatings were used in LBQ0-2 (see Figure 2.10b). They were made of acrylate (the green cable on the left) and polyimide (the yellow cable on the right) and have been tested in triaxial test environments by [Salazar et al. \(in preparation\)](#). While the polyimide cable can stand up to 300 °C and up to a confinement of ~60 MPa, acrylate works up to 80 °C and 200 MPa.

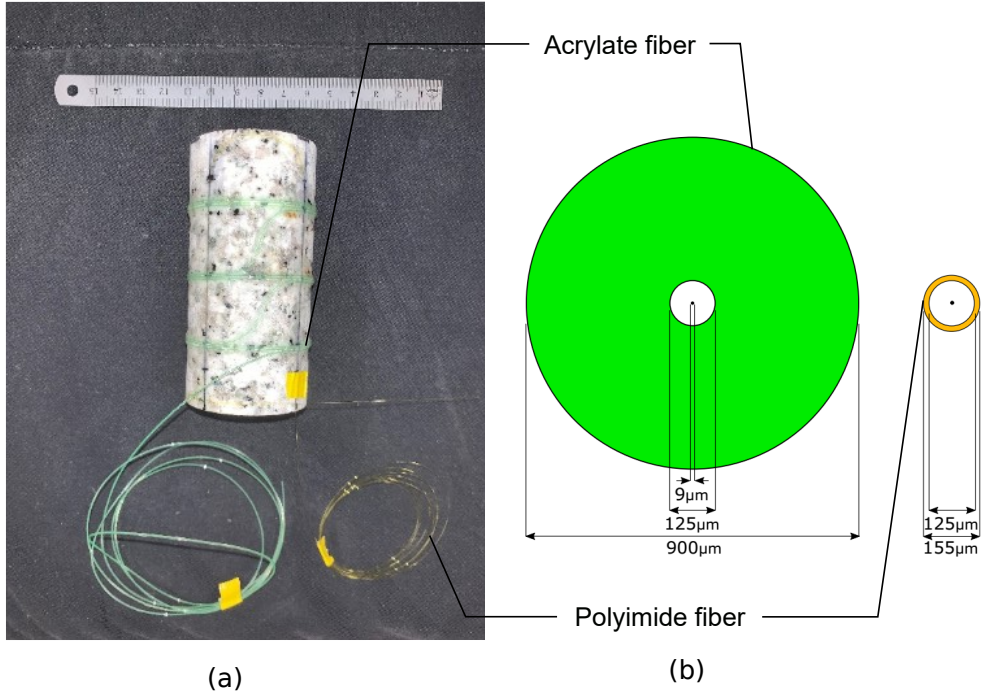


Figure 2.10: (a) The photo that shows how the acrylate and the polyimide cables are distributed on the surface of the sample. (b) Adopted from ([Salazar et al., in preparation](#)). The schematic diagram showing the geometry of the Acrylate (in green) and the Polyimide cables (in yellow).

In the experiments described next, the polyimide cable was wrapped around the sample radially at three levels of heights and the acrylate cable was wound vertically at four genetrices of the cylinder with uniform spacing (see Figure 3.4a). The fiber optics technology provided the possibility to measure the strain field with higher resolution, compared with strain gauges. This enabled the observation of the heterogeneous strain field as the cracks nucleate and propagate across the sample.

Methodology

This section will explain the conducting of experiments and the processing of data in details. In Section 3.1, sample preparation and loading protocols in three compression tests are elaborated. As an important preparation for the tests, calibration of the loading frame is also described. Appropriate data processing methods are the keys to understand physical processes in the experiments. In Section 3.2, the seismic deformation is analyzed with ultrasonic tomography, source localization, moment tensor inversion and statistical characterization of seismicity; whereas the aseismic deformation is evaluated with interpolation for fiber optics measurement and stress inversion.

3.1 Experimental procedures

The sample used in the three experiments are cylindrical Rotondo granite samples (~ 50 mm in diameter and ~ 100 mm in height). The exact sample sizes are summarized in Table 3.1. Before putting samples into the load cell, considerable efforts have been made to ensure that the optical fibers can resist high confining pressure, that the AE sensors are in reliable contact with the sample surface and that the sensors and the samples are sealed from the oil that transfers hydraulic pressure. The best solution we propose so far is explained in Figure 3.1 following the sequence from (a) to (i).

3.1.1 System stiffness calibration

Before testing on rocks, the stiffness of the system has been calibrated under different temperatures and confining pressure using a cylindrical aluminum sample, whose modulus under different confining pressure is well known (Torić et al., 2017). The loading system is calibrated with respect to two cell stiffness - first the frame stiffness (k_{frame}) from the loading piston to the top and the bottom of the sample (inside the red rectangle) and second the partial cell stiffness ($k_{partial}$) of the part only between the LVDTs (inside the dashed blue rectangle). In either case, the stiffness can be computed according to Eq.(3.1).

Table 3.1: Summary of the sample sizes in the three experiments.

Experiments	Height (mm)	Diameter (mm)
LBQ0	101.7	49.5
LBQ1	98.7	49.6
LBQ2	101.6	49.5

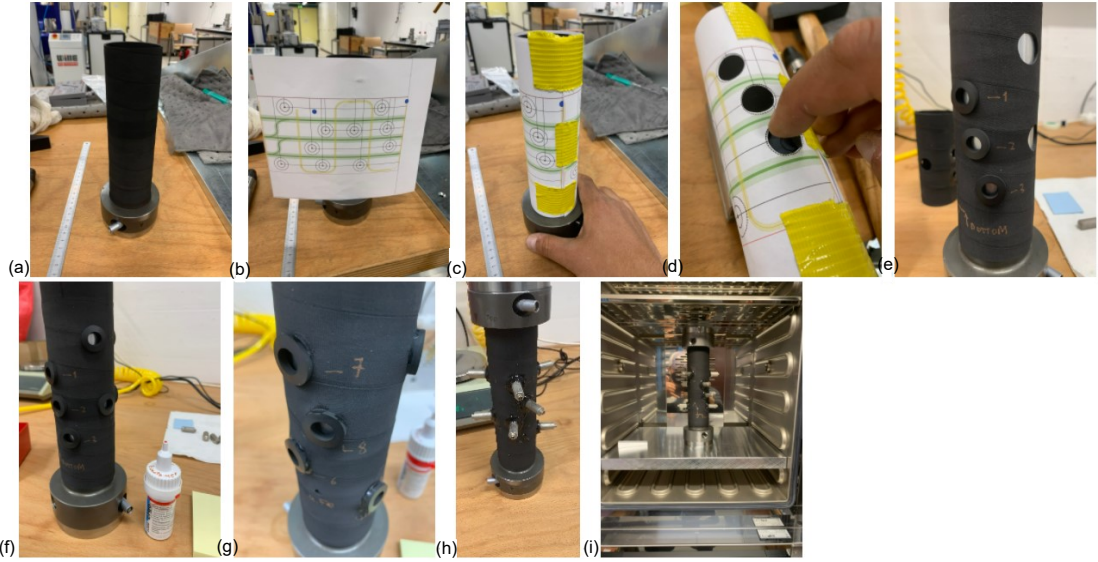


Figure 3.1: The group of photos that shows how the FO, AE sensors and the rubber jacket are prepared. (a) Place jacket around plastic dummy sample and use extra set of adapters to ensure the sample is at the correct height. (b) Print the mapping of sensors distribution on a paper at 1:1 scale. (c) Wrap the printed map around the rubber jacket. (d) Punch the holes in the rubber with plastic piece as the transfer material. (e) Squeeze the porthole adapter into the hole. It is fixed by the frictional snug and stays in place with no glue. (f) Use the rubber glue to tack the porthole adapters to the viton sleeve. (g) Do not fully cover the seam with glue, this allows for air to escape. (h) Use the applicator gun and stick to bead both the sensor to porthole and porthole to viton jacket using HySOL 9455. (i) Cure in oven.

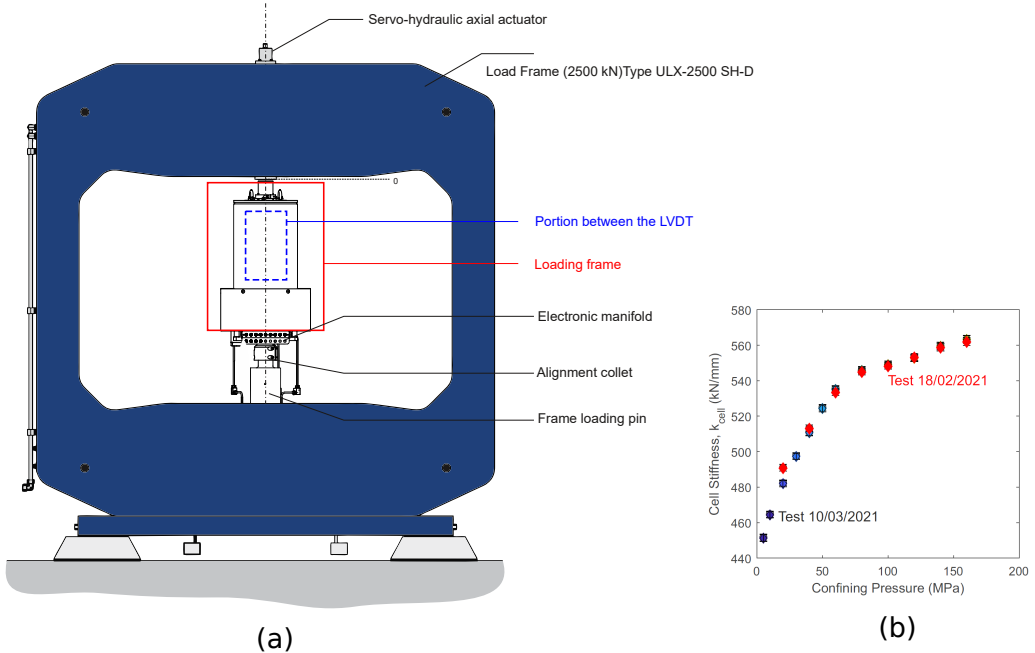


Figure 3.2: (a) The aluminum sample for the calibration of the stiffness of the framework. While the region inside the red rectangle is involved in the calibration with respect to the displacement of the loading piston, the diagram beside the frame shows the part of the framework that the LVDTs measure. (b) The stiffness of the loading framework that changes with the confining pressure.

$$\frac{1}{k_{measured}} = \frac{1}{k_{frame}} + \frac{1}{k_{partial}} \quad (3.1)$$

where $k_{measured}$ is the apparent sample stiffness directly computed from measurement from piston displacement when $i = frame$ or from LVDTs when $i = partial$.

3.1.2 LBQ0

This is a pre-test to examine the functionality of the facilities and the entire procedures on rock with the following principal objects:

- Test the sealing of the jacket and the functionality of the different sensors – strain gauges, acoustic emission sensors, LVDTs and optical fibers;
- Test the loading and monitoring protocols and acquisition parameters;
- Quantify the static and dynamic mechanical properties of the rock;
- Providing data for designing the processing routines.

In LBQ0, the loading was divided into two phases. During the Phase I, confining pressure was increased stepwise at 5, 10, 15, 20 and 25 MPa. While holding the confining pressure at these values, the deviatoric stress cycled between 5 and 50 MPa at 25, 35, 45 MPa/min in each of the three cycles. While applying the above loading schemes, ultrasonic tomography (UT) was conducted by shooting each of the 5 sensors every 20 seconds (group shot interval). To avoid the interference of waves induced by the sources, sensor $n+1$ was pulsed 700 ms after sensor n . The sampling rate of the receiver sensors are set to 20 MHz. Phase I was designed to explore the static properties of the rock sample and the change of P-wave velocity with both the confining pressure and the deviatoric stress.

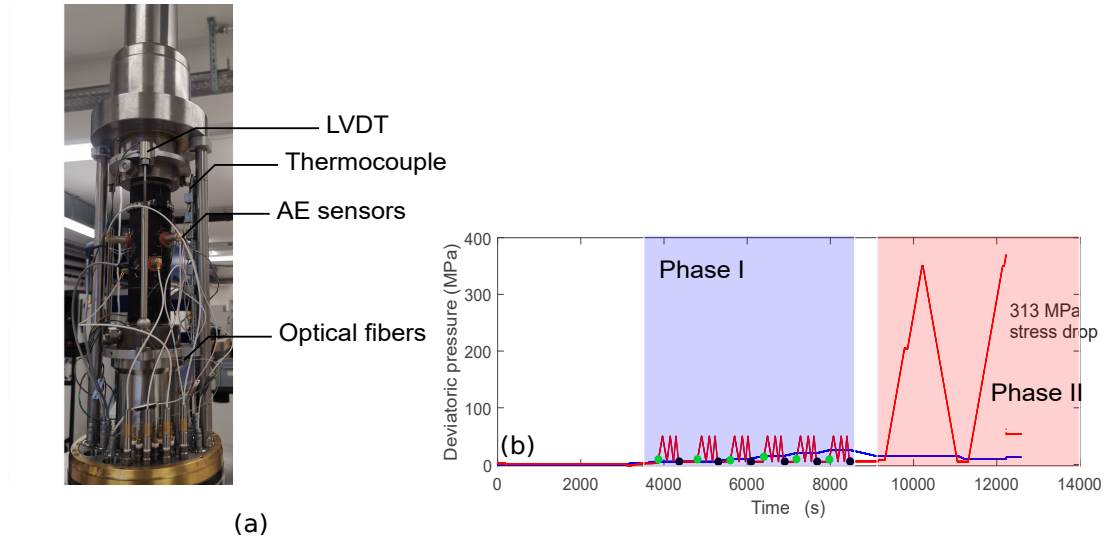


Figure 3.3: (a) The photo that shows the jacketed sample in LBQ0 and the connection of all the sensors to the framework. (b) The loading protocols in LBQ0.

During the Phase II, the confining pressure was brought back to 15 MPa. Then, the deviatoric stress was raised at a speed of 25 MPa/min from 5. At 8.4 MPa and 204.4 MPa, the deviatoric stress was held for a short period of time to check the loading parameters in the software. During the first ramp up, the sample did not fail at the deviatoric stress of 355 MPa. We decided to lower the confining pressure to 10 MPa. At this confining pressure, the sample failed at 369.8 MPa and

a large stress drop of around 313 MPa was observed. In Phase II, ultrasonic tomography was not activated and the AE sensors were continuously recording the motion on the surface of the sample at a sampling rate of 10 MHz instead of 20 MHz to reduce the size of the data. It will be found in the following part of the thesis that our accuracy in signal analysis does not require a too high sampling rate so far.

The large stress drop of 313 MPa at the end of the experiment indicates an unstable crack growth. During this process, the macro-cracks can propagate extremely fast and the induced seismic waves can strongly interfere with each other, bringing difficulties to events detection and to the understanding of physical process. Attempts to solve this problem have been made in the following two experiments.

3.1.3 LBQ1

In LBQ1, the number of AE sensors was increased to 10 for a higher accuracy in localization and moment tensor inversion. Horizontal FO fibers were moved closer to the middle of the sample since according to LBQ0 most events occurred in the middle of the sample. The strain heterogeneities in this part were perceived to be more closely related to AE events from the results in LBQ0.

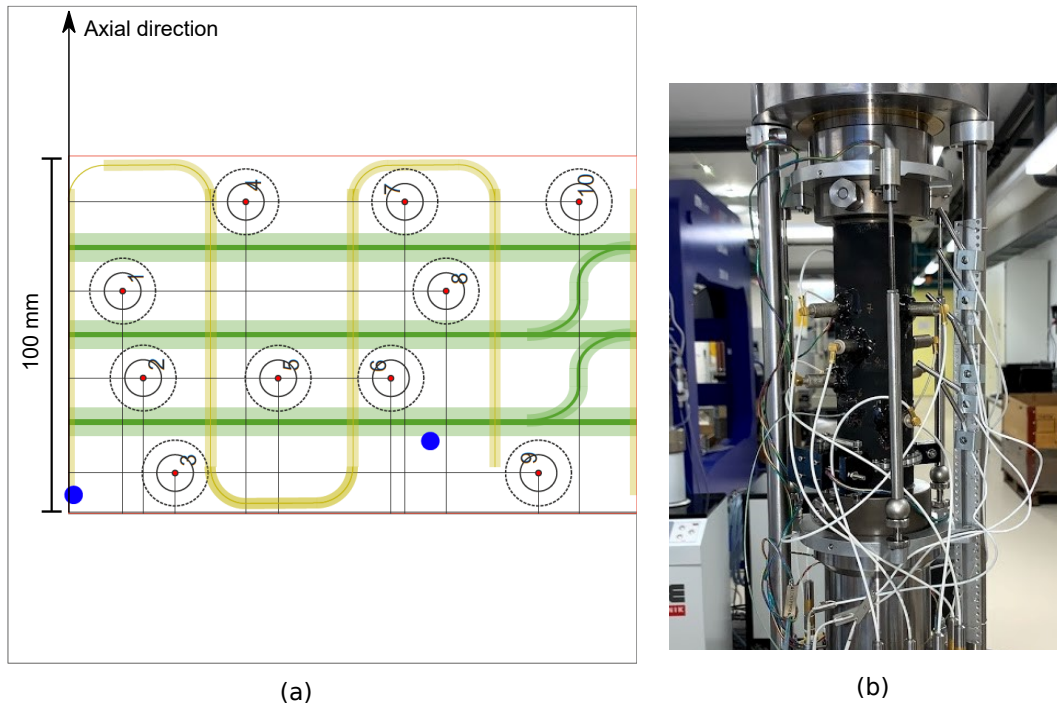


Figure 3.4: (a) The map that shows how the AE sensors and FO fibers are distributed. (b) The jacketed sample in LBQ1.

The loading scheme of LBQ1 is similar to that of LBQ0 and only the differences between the two experiments are explained. In Phase I, the sampling rate of the AE receivers are set to 10 MHz again to save disk space. In Phase II, we kept the confining pressure at 10 MPa from the beginning based on our experience in LBQ0 and, therefore, don't need to bring down the load in the middle. But the deviatoric stress was held at 295 MPa ($\sim 80\%$ of the failure stress estimated from LBQ0) for 10 minutes to capture the creeping of the rock. Another difference is that the loading is controlled by displacement (0.140 mm/min), which is almost equivalent to 25 MPa/min during the elastic deformation. This time, ultrasonic tomography was also conducted during the

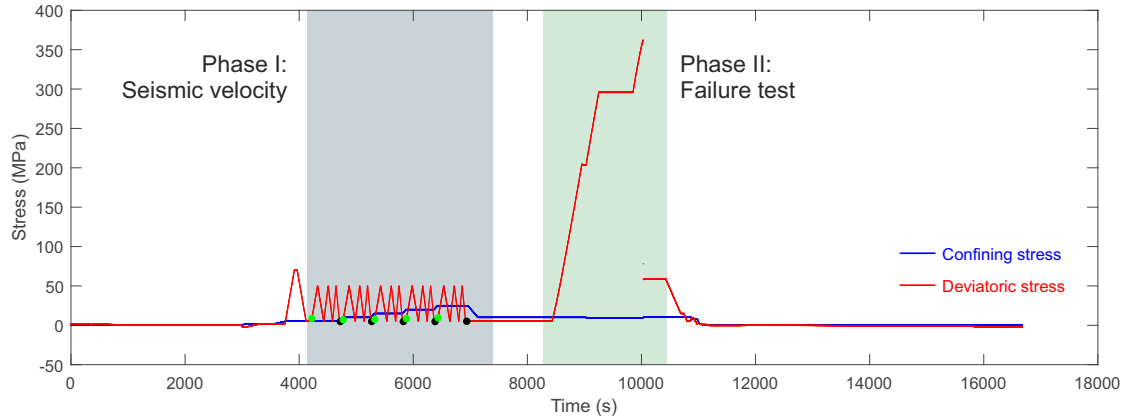


Figure 3.5: The loading protocols in LBQ1. In Phase I, the deviatoric stress was cycled at different confining pressure while in Phase II the sample was loaded to failure.

Phase II. Each sensor shot every 100 seconds and a total of 17 groups of shots are collected during the failure test to observe how the velocity of the rock varied with the load and the occurrence of micro-seismic events.

Switching to displacement control mode does not effectively stabilize the fracture growth. A Stress drop of around 300 MPa was still observed. In the next experiment, the position of the loading piston would be held as the stress approaches failure level.

3.1.4 LBQ2

The same sensor configuration was employed as LBQ1 and the jacket, which was still in good condition in terms of sealing property and of the bonding to AE sensors, was also recycled to save the preparation time.

To understand the capability of our software, hardware and the properties of the sample better, the full experiment was conducted in three stages (I-III).

In Stage I, there were three major goals:

- Check if stacking in ultrasonic tomography would allow picking arrivals accurately using picking algorithms;
- Check if lowering the audible noises from the intensifier for hydraulic pressure in the cell would also suppress the noise in the recorded signals;
- Understand how the P-wave velocity in the new sample would change with the variation of confining pressure.

Bearing the above goals in mind, the experiment in Stage I experienced three phases. In each phase, the deviatoric stress was held at 5 MPa as the confining pressure stepped up among 5, 10, 15, 20 and 25 MPa and then went down among 25, 20, 15, 10, 5 MPa sequentially. Among the three phases, the number of stacks in ultrasonic tomography varied between 5 and 20, while the pressure at the intensifier varied between 290 bars and 70 bars.

However, an accident occurred at the end of Phase I. Due to an erroneous operation in the Geosys software, the piston was held back to the initial position creating a null contact between the loading

Table 3.2: The list of parameters for ultrasonic tomography during the Stage I of LBQ2.

Stack	Voltage (V)	Gain (dB)	Intensifier HF
5	200	40	290 bars
5	200	40	70 bars
20	200	40	70 bars

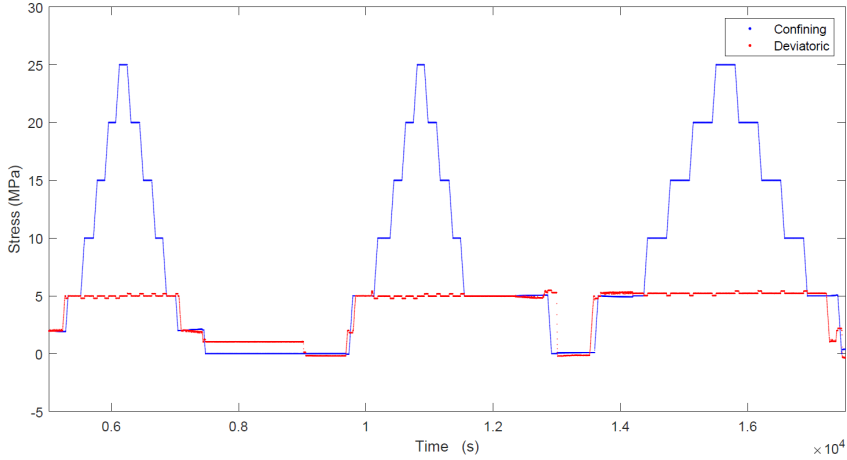


Figure 3.6: The loading protocols in the Stage I of LBQ2. The confining pressure was cycled for three times and ultrasonic tomography was conducted in each cycle but with different surveying parameters listed in Table 3.2

platen and the top surface of the sample while the confining pressure was still around 0.5 MPa. The latter pushed the jacket into the interval. Then, in the second and the third cycle, that part of the jacket was also pressed and distorted. After the experiment of the first day, the loading cell was disassembled and the jacket was brought back to its normal position. No visible crack in the rubber was noticed then.

In Stage II, three goals were set:

- Check the pollution of AEs by the ultrasonic tomography;
- Find the effective method to separately analyze ultrasonic tomography and AE data;
- Check if increasing impulse voltage and the gains at the amplifier during the ultrasonic tomography can make arrival picking easier.

To achieve the targets, a two-phase experiment was conducted. During the phase I, the deviatoric stress cycled between 5 and 100 MPa (110 MPa in the fifth cycle) for five times at a loading rate of

Table 3.3: The list of parameters for ultrasonic tomography and DAQ during the Stage II of LBQ2.

Phase/Cycle	Stack	Voltage (V)	Gain (dB)	Intensifier HF
Phase I, Cycle 1	5	200	40	70 bars
Phase I, Cycle 2	5	300	40	70 bars
Phase I, Cycle 4	5	200	60	70 bars
Phase I, Cycle 5	5	300	60	70 bars
Phase II	5	300	40	70 bars

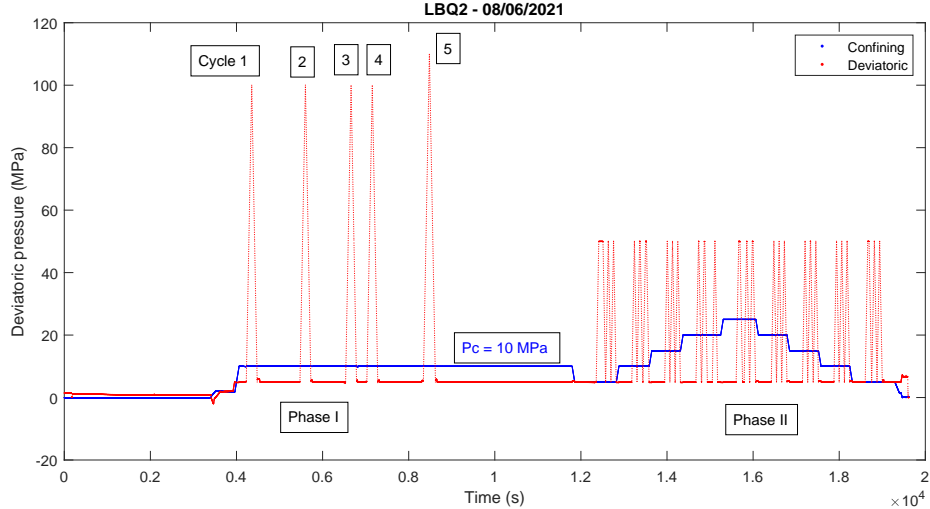


Figure 3.7: The loading protocols in the Stage II of LBQ2. During the Phase I, the deviatoric stress was cycled between 5 and 100 or 120 MPa to generate some AE events and in Phase II the deviatoric stress was cycled in a lower range between 5 and 50 MPa at different confining pressure.

45 MPa/min. The confining pressure was held at 10 MPa, as all our previous failure test in LBQ0 and LBQ1. In the first three cycles, ultrasonic tomography is activated with a group interval of 45 seconds while AE sensors are recording AEs continuously at a sampling rate of 10 MHz. During the first three cycles, the gain at the amplifier was set to 40 dB whereas the impulse voltage varied between 200 V and 300 V. Due to logistic problems, the data during the third cycle is saved and, therefore, also not shown in the Table 3.3. In the fourth and the fifth cycle, the gain is raised to 60 dB with the impulse voltage of 200 V and 300 V, respectively. Then, to see if P-wave velocity in the sample would still vary with the confining and deviatoric stress after the 5 cycles in Phase I, the same loading scheme as that of Phase I in LBQ0 and LBQ1 was employed in the Phase II of LBQ2 in Stage II. In this phase, the parameters of ultrasonic tomography are shown in Table 3.3.

After this experiment, the sample was left in the cell (with zero loads) for one full day to allow for data pre-processing before the starting of the Stage-III experiment.

Then, the main goal of Stage III is to study the seismic and aseismic deformation of the sample before and during the failure of the sample.

The loading rate has been dropped from 0.14 mm/min to 0.10 mm/min to slow down the approaching of the rock sample to failure. Ultrasonic tomography was conducted every 100 s as in LBQ1. Again, due to checking of parameter settings, the loading stopped for around 20 seconds when deviatoric stress reached ~ 204 MPa. The peak stress of ~ 225 MPa was reached at around 893 s after the starting of the ramp up. The instant when the stress started to drop, the loading system was set to hold position. This enabled us to observe a less violent stress drop of about 48.4 MPa for around 40 seconds.

Compared with LBQ0 and LBQ1, more parameters of the system in measurement were explored in LBQ2. Increasing the gain of the amplifier from 20 dB to 40 dB can observably raise the SNR, and the quality of the data is good enough so that the arrivals can be picked manually with an accuracy of $\pm 5 \times 10^{-7}$ s even for the sensors that are as close as 20 mm away from each other. The stacking of signals can suppress noises, which is significant for 20 dB gain. But it is not necessary to stack for 40 dB gain for tomography.

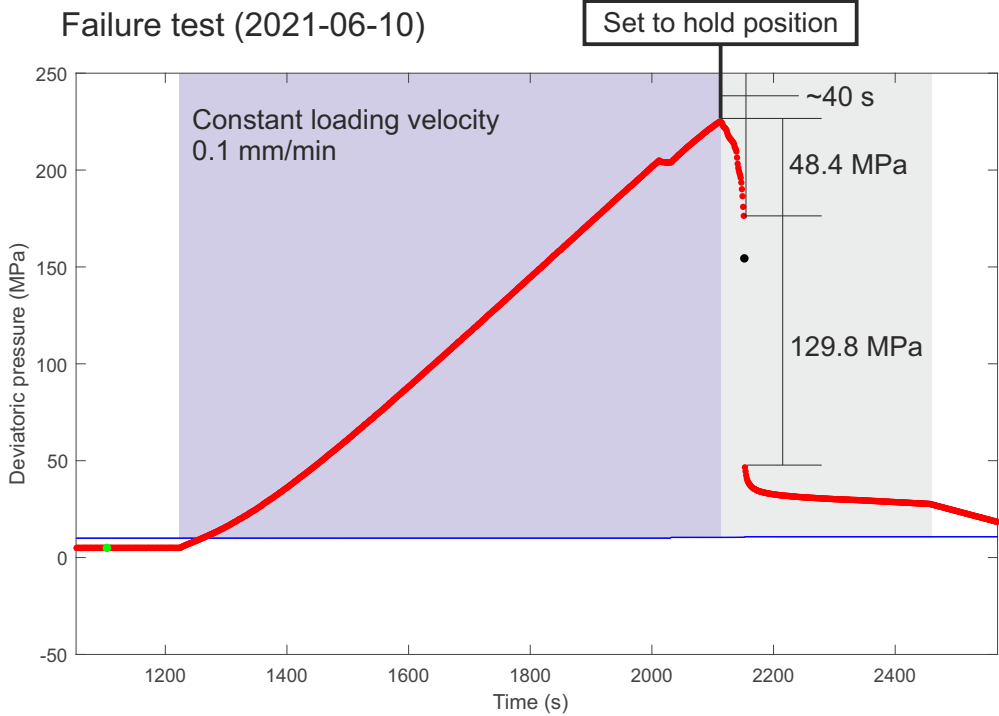


Figure 3.8: The loading protocols in the Stage III of LBQ2. The sample was directly loaded to failure.

Albeit with good care and experience from the previous two experiments, two accidents still took place in the experiment. First, after the Phase I in Stage I, the axial loading piston was brought back and lost contact with the sample while confining pressure was about 0.5 MPa. This caused the jacket to slip off from the cap and the confining fluid to get in contact with the sample. Probably due to the serious distortion of the jacket, it lost its sealing capabilities and leakage of the sample to confining oil in the load cell took place during the experiment in Stage II and III.

3.2 Data reduction and processing

3.2.1 Static properties of the sample

In experiments LBQ0-2, cyclic loading of deviatoric stress under different confining pressure has always been conducted. Since the loading system has been calibrated for both the measurement of the loading piston displacement and the displacement of LVDTs', the Young's modulus computed from the two methods can be cross-validated (see Figure 3.10). Fiber optics can further validate the measured static modulus, as shown in Figure 3.10.

3.2.2 Spectrum analysis for signals and noises

As will be elaborated in the following sections, background noises sometimes need to be filtered from the recorded time series. The filtering process is usually based on the difference in frequency spectra between the seismic signals and the background noises (Margrave, 1998). Such difference is thus investigated for the reported experiments (LBQ0-2). Frequency spectra of seismic signals

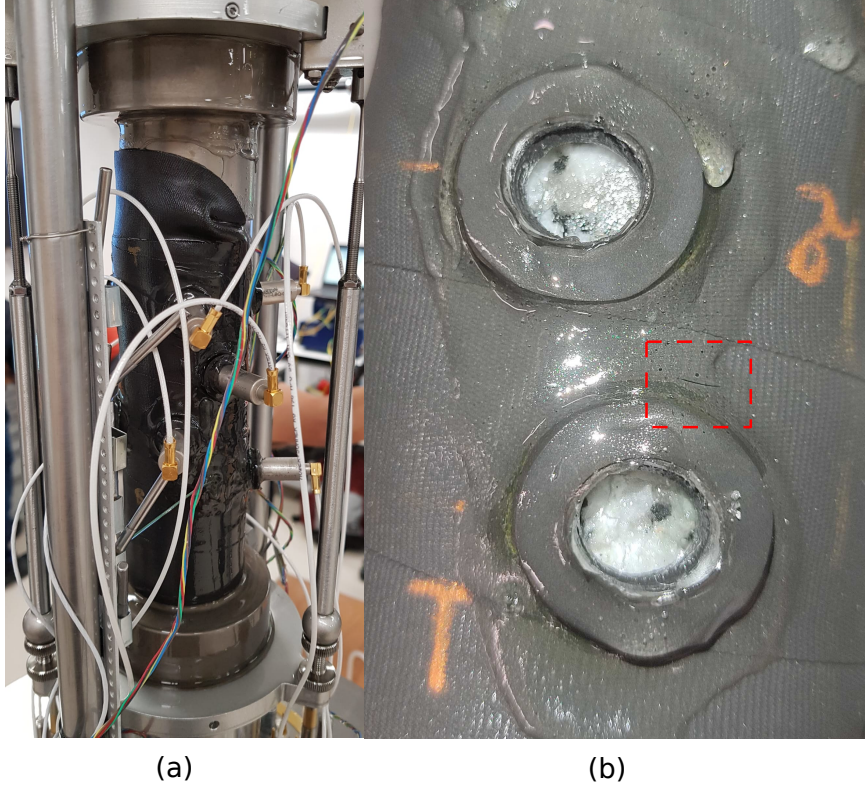


Figure 3.9: (a) The photo that shows how jacket has been distorted in Stage I of LBQ2. (b) Photo that shows the failure of jacket and leakage. The crack is shown inside the red rectangle.

Table 3.4: Parameters of the DAQ for the recording of the AEs.

Experiment	Gain (dB)	Dynamic range (V)	Intensifier HF
LBQ0	20	± 1	290 bars
LBQ1	20	± 2.5	70 bars
LBQ2	40	± 25	70 bars

and background noises may be influenced by many factors, e.g. different settings on the acquisition system Elsys. The settings used during the three experiments are summarized in Table 3.4.

One example trace of each experiment is analyzed (see Figure 3.11) to demonstrate the general features of the frequency spectra of the signals and the noises in all the experiment. The traces are picked at the early stage of the failure test when seismic events only occur sporadically. Frequency spectra of 100-microsecond-long time series in the noise part and signal part of the traces are then computed with Fast Fourier Transform (FFT). From Figure 3.11, the most important feature is that signals have higher amplitude than noises below 1 MHz in all three experiments. It is also found that the frequency of noises in LBQ0 and LBQ1 oscillate around 0.02 V/Hz whereas around 0.1 V/Hz in LBQ2. This difference is most likely due to the different amplifier gains given that dynamic range settings do not seem to influence the noise level according to LBQ0 and LBQ1 (see Table 3.4). The relative amplitudes of the signals' frequency spectra are not comparable since the magnitude of each event is different. However, as predicted by the Omega model (Hanks, 1979), the shapes of the spectra show a flat low-frequency platform and a corner frequency of around 500 kHz.

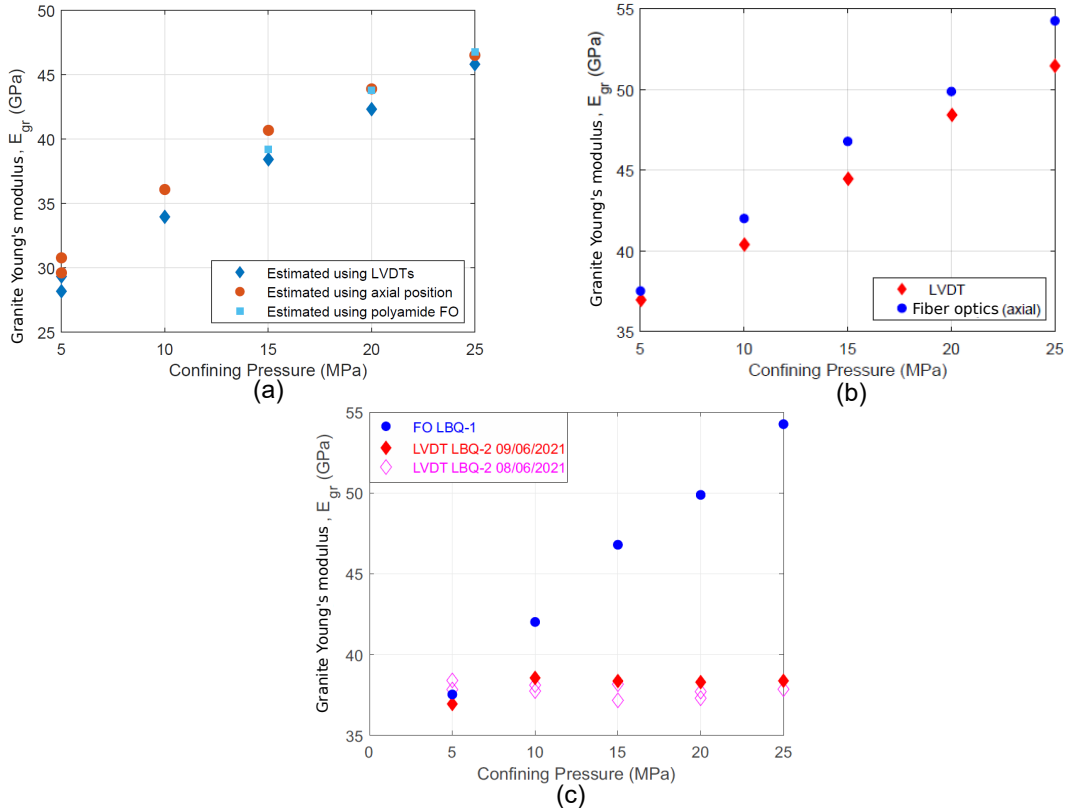


Figure 3.10: Static properties of the samples in LBQ0-2. (a) Change of Young's modulus with the confining pressure in LBQ0, computed from the measurement with the calibrated loading piston, LVDTs and FO. (b) Change of Young's modulus with the confining pressure in LBQ1, computed from the measurement with the calibrated LVDTs and FO. (c) Change of Young's modulus with the confining pressure in LBQ2, computed from the measurement with the calibrated LVDTs. Change of Young's modulus in LBQ1 is shown together for comparison with blue dots.

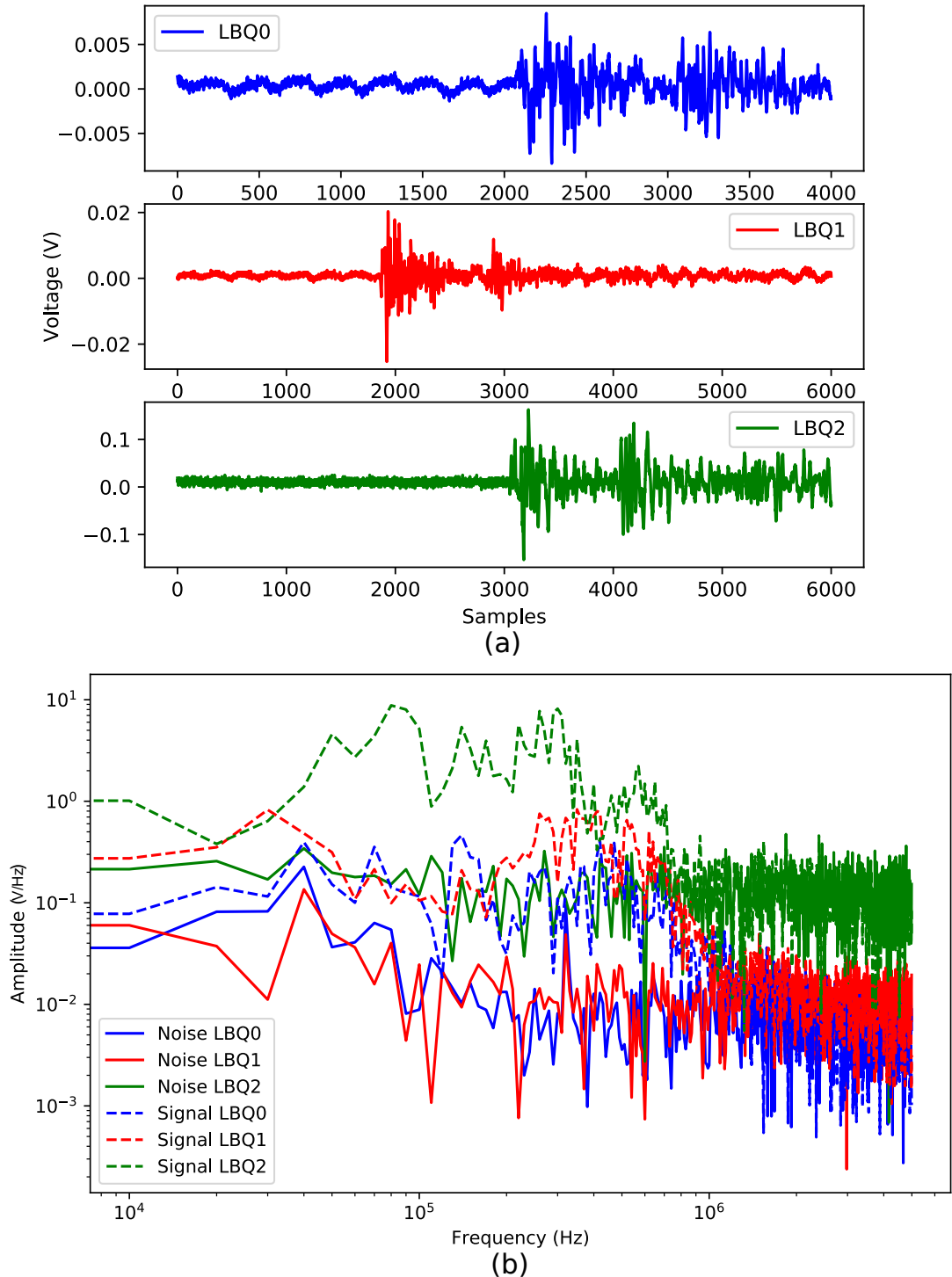


Figure 3.11: Time series (a) and frequency spectra (b) of the background noises and desired signals from LBQ0, LBQ1 and LBQ2. The spectra of signals are computed from signals of the weakest locatable events in all three experiments.

3.2.3 Events detection and data reduction

Processing AE data starts from dealing with continuously recorded electrical signals from the piezoelectric sensors. Only the portion of signals where seismic waves are recorded with sufficient amplitudes can be useful for analyzing seismicity. Such process of extracting useful signals from the raw AE data is called event detection and data reduction. In this research, the event selection is done with the short-time average/long-time average (STA/LTA) algorithm ([Trnkoczy, 1998](#)). The algorithm is sensitive to weak seismic signals and can, to some extent, adjust to changing background noise levels. Such features enable the reduction of data size while keeping most of the events that can potentially be analyzed at a later stage. It, therefore, serves well for the purpose of events detection and data reduction.

The STA/LTA algorithm processes the seismic signal by employing two moving windows – a short time window average (STA) and a long time window average (LTA). The STA measures the change of signals in a short period and is sensitive to the occurrence of seismic events, whereas the LTA is designed to be only sensitive to the change in background noise levels.

In practice, absolute amplitudes of the incoming signals are calculated and averaged in both windows. The STA/LTA ratio is then derived and continuously compared with a threshold value. If the ratio on a channel is larger than the threshold $\mu(STA/LTA) + a \cdot \sigma(STA/LTA)$, the channel will be triggered. $\mu(STA/LTA)$ and $\sigma(STA/LTA)$ are the mean and standard deviation of the STA/LTA ratio, respectively. In this step, a and the lengths of STA and LTA are variables to be probed. Once these variables have been determined, seismic events on a single channel can be detected.

However, each channel has different trigger times for the same event because of the difference in the travel times from a seismic source to AE sensors. The triggering at one sensor also does not always ensure a usable event for many reasons, e.g., electronic noises at a few channels or weak recordings at some other channels due to wave attenuation. These two factors necessitate an additional detection classifier that accounts for the triggering times at all channels. The classifier should be able to pick out events that trigger enough number of channels within a short time window.

In this classifier, the temporal distribution of trigger times on all the channels are represented by a histogram. The bin-width of the histogram is defined as the time window size, which should be both long enough so that one event can trigger all channels and short enough so that any channel is not triggered by different events. In this step, the bin-width is a key parameter for event classification and should not be selected randomly. Figure 3.12 shows how the width is determined using ten seconds of the recorded AE data. The width is varied from 1 microsecond to 120 microseconds with the increment of 1 microsecond and the maximum number of detections among all the bins in the histogram of trigger times is computed. Given that the proper bin-width should contain a maximum of 10 detections on the 10 channels, a plausible window size should, therefore, be set between 25 and 61 microseconds.

The final results of the above parameter study in event detection are summarized hereafter. The STA and LTA window lengths are 5×10^2 and 1×10^4 microseconds, a is 1 or 0.5 and the bin-width for the histogram is between 25 and 61 microseconds.

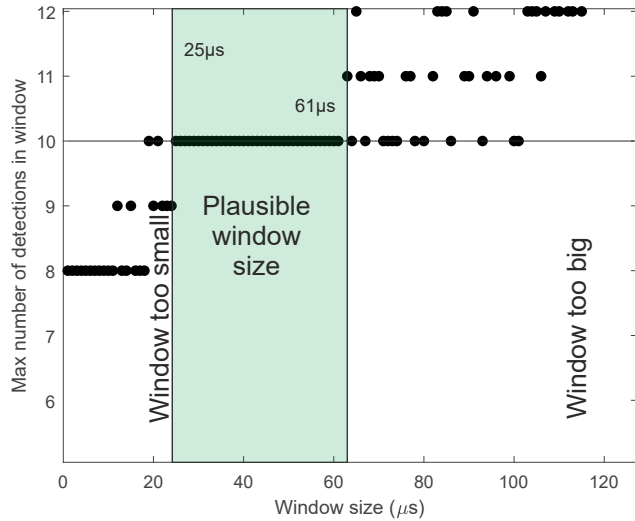


Figure 3.12: The change of maximum number of detections as a function of the window size. The proper window size should contain a maximum of 10 detections on the 10 channels and is shaded in green.

3.2.4 Arrival picking

In LBQ0, 2102 events on 5 amplified channels are selected using the methods in Section 3.2.3. It is assumed that all the events are locatable and arrivals are tentatively picked with different picking algorithms – AIC picker, AR-AIC picker and cross-correlation.

AIC picker is based on the Akaike information criterion (AIC) that reads (Akaike, 1974):

$$AIC(t_w) = (t_w - t_0) \log(var(R_w(t_0, t_w))) + (T_w - t_{w+1}) \log(var(R_w(t_{w+1}, T_w))) \quad (3.2)$$

where t_w is the time at data point w , t_0 is the time at the start of the waveform, T_w is the time at the end of the waveform and $var(R_w(t_0, t_w))$ is the variance of all the voltages from t_0 to t_w . The minimizer of this function is determined to be the first P-wave arrival. This picker is widely employed in AE studies (Kurz, 2015; Li, 2015) and was found to work well on the majority of the traces. However, when an error occurs due to the complex noises in the signals, we could not find the proper tuning of the parameters to make for adequate results.

The AR-AIC picker is a picking function built-in the Python package – ObsPy (Beyreuther et al., 2010). The algorithm picks onset times using an Auto Regression - Akaike Information Criterion (AR-AIC) method (Akazawa, 2004). Unlike the original AIC picker, four parameters can be tuned to account for different noise levels. However, on the other hand, it is difficult to decide on a parameter set that is suitable for all the traces. An example that shows how the picked arrivals change when the length of variance window for the P-wave arrival (l_p) is shown in Figure 3.13.

As observed in Figure 3.13, picking results for the P-wave arrival are very sensitive to l_p . This indicates that the parameters need to be chosen trace by trace. Extra efforts on extracting adequate features of the signals (e.g. SNR) are, therefore, required to guide the automatic choice of picking parameters. Such effort is beyond the scope of this thesis and will be discussed in Section 6.2.

Apart from the above two pickers, cross-correlation between traces has also been an effective method to increase the accuracy of arrival picking in the field. However, since the azimuthal

angles between the events and the sensors and the focal mechanisms of events can vary a lot in the experiment. This method does not currently work in our analysis but has shown potential in the past (Chen et al., 2011).

Testing with the AE data from LBQ0, the AIC picker was chosen since it is comparatively more accurate for most of the traces. However, localization with only five sensors can be very inaccurate and it is impossible to invert for moment tensors according to Kwiatek et al. (2016). The results from LBQ0 are therefore not looked at in detail in this dissertation.

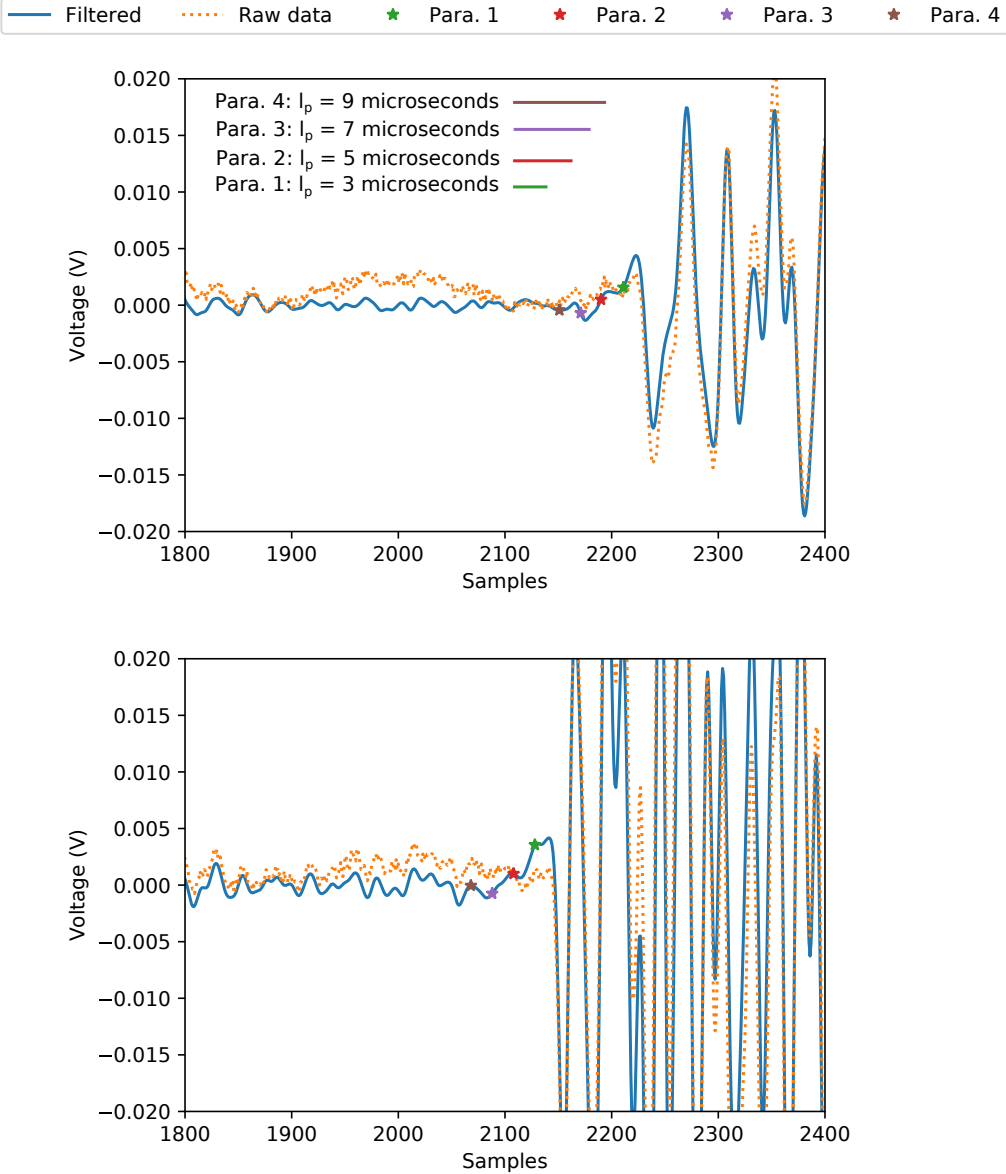


Figure 3.13: Signals of one seismic event recorded at two channels in LBQ0. The first P-wave arrivals (the color-coded stars) are picked with the AR-AIC algorithms with the varied length of variance window.

In LBQ1, the parameter a in the threshold of STA/LTA algorithm was lowered to 0.5 to decrease the magnitude completeness of the AE catalog. This means some traces may have too low signal to noise ratio (SNR) where the P-wave arrivals will not be picked accurately. Another problem in the preliminary detection based on the STA/LTA algorithm is that as the sample approaches failure, recorded seismic waves from a single large event (e.g. the event of magnitude larger than

Mw -6.5) can last as long as 1 millisecond because the released energy need sufficient time to be attenuated. The coda waves of such events can, as a result, render the arrival picking impossible in this interval (see Figure 3.14). Another problem with the persistence of coda waves is that they can trigger the STA/LTA detection multiple times in the same seismic events. These problems are dealt with by constraining a temporal resolution in detection. Since the attenuation of large events can take as long as 1 ms, the entire duration of the experiment is divided into 2-ms-long intervals. In each interval, the trace with the highest averaged amplitude is chosen as the representative event. This also means if more than one event occurs in the same interval, the largest among them, representing the event that releases the most energy is kept. After this process, the number of events for localization drops from 4521 to 2896.

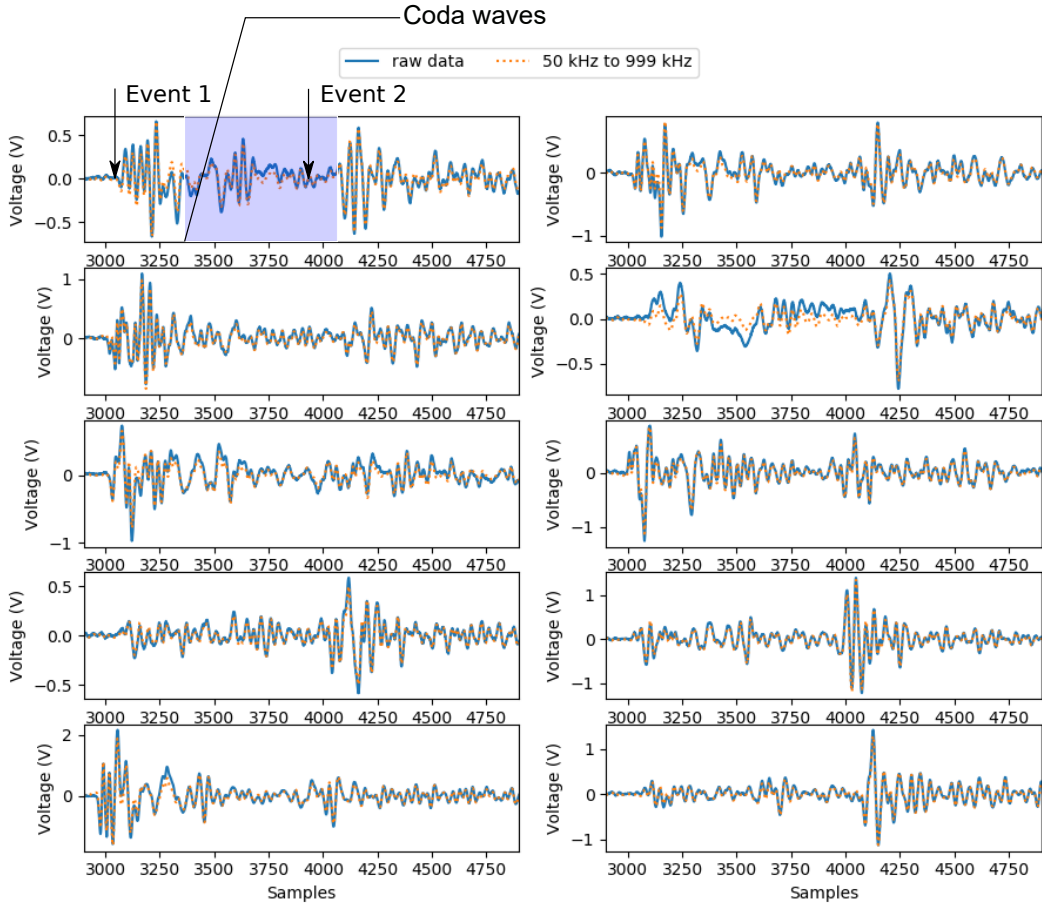


Figure 3.14: Signals recorded on 10 channels. The interval between two events is only around 100 microseconds so that the coda waves (shaded in blue rectangles) of Event 1 pollute the first arrivals of Event 2.

Once events were selected, first P-wave arrivals are isolated on all the traces. Some additional efforts have been made to improve the AIC picker. To find the reasons for the inaccuracy of the AIC picker, some example traces where the AIC picker does not work well have been studied. They can be represented by the trace in Figure 3.15. Two problems with the AIC picker were found. The first problem is that when one smaller event takes place less than 100 microseconds before a larger event, the SNR of the smaller event can vary at different sensors due to the different source-receiver distances (see Figure 3.15c). If the SNR is high enough, the AIC picker will pick the arrival of the smaller event; otherwise, the AIC will only be sensible to the larger event. Such inconsistency in the picked event causes the inaccuracies of the AIC picker. The second problem

is harder to explain but is also more frequently observed in our database – the global minimum of the AIC time series is not necessarily the arrival of an event (see Figure 3.15b).

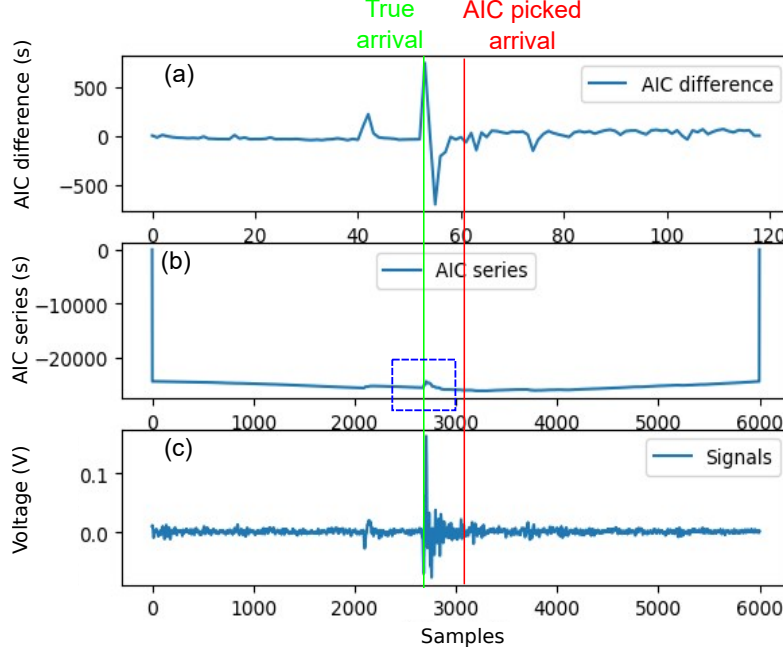


Figure 3.15: The bottom subplot (c) shows the time series of an example trace that contains seismic events but the arrivals can be wrongly picked with the AIC picker. (b) AIC series of the time series in (c). The blue dashed rectangle marks the local feature that may characterize the arrivals better than the global minimum. (a) Smoothed difference of the AIC series in (b).

We propose a possible analysis here. Regardless of the above problems of multiple events and complex background noise level, a more omnipresent feature than the global minimum of the AIC series is found – as long as the SNR is high enough, a local minimum (inside the dashed blue rectangle in Figure 3.15b) shows up in the AIC series at the arrival of an event and the stronger the event, the stronger the change of the slope at the local minimum. The difference of the AIC series is computed to amplify this feature, where the local minimum will show up as an impulse. Smaller scale variation in the time series due to noises can be suppressed by down-sampling before taking difference. The details of this algorithm are delineated in Figure 3.16a. The algorithm is called the adapted AIC picker (Ada-AIC picker). This Ada-AIC picker significantly improved the accuracy of arrival picking (e.g. Figure 3.16b).

Based on the picked arrivals, events that can potentially be located accurately are further selected. When the arrivals of an event are picked accurately, the difference in arrivals at different channels shall be smaller than 20 micro-seconds. Using this criterion, most of the incorrectly picked arrivals can be further filtered out. The minimum number of sensors on which the arrivals are picked accurately are specified to increase accuracy in events localization. In LBQ1, if the number is set to 8, the number of locatable events is 2746; while the locatable events drop to 2146 if the number is set to 10.

Analysis with the data in LBQ0 and LBQ1 improves the procedures for event detection, classification and arrival picking. The procedures and the parameters are employed in LBQ2.

In LBQ2, the parameter a in the threshold of STA/LTA algorithm was 0.5. After the event selection and classification, 6767 events are left for arrival picking. We use the Ada-AIC picker to get the

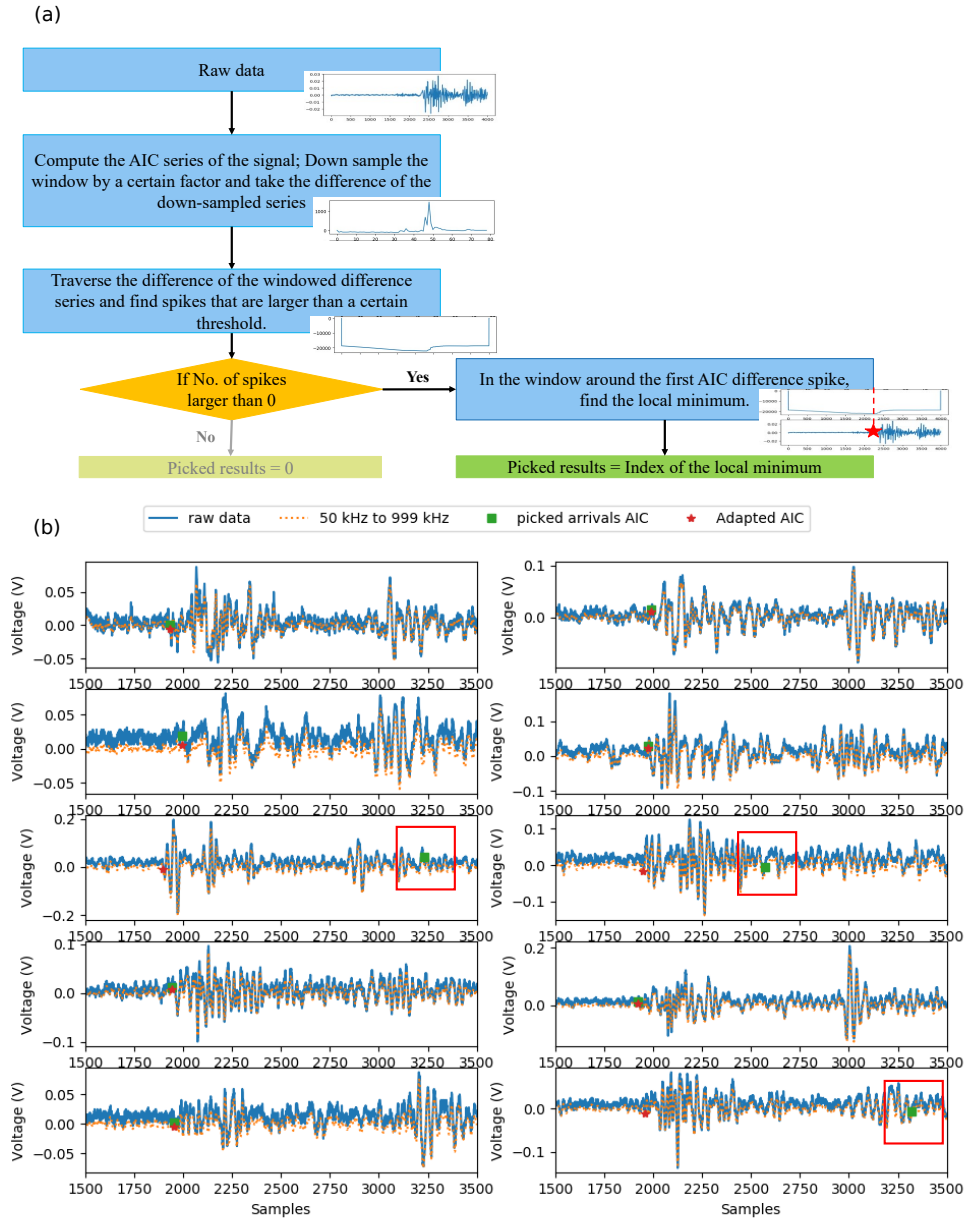


Figure 3.16: (a) The diagram that shows the adapted AIC (Ada-AIC) picking algorithm. (b) Signals of one example event recorded on 10 channels. The arrivals picked with the Ada-AIC picker (red stars) perform better than the AIC picker (green squares) on three channels.

P-wave arrivals on all the traces, rule out the events that are not picked accurately and reduced the temporal resolution in detection to 2 ms. The above procedures eventually leave us with 1978 events whose locations and moment tensors can be inverted.

3.2.5 Ultrasonic tomography

The goal of ultrasonic tomography is studying the change of velocity structure with loading and constraining the initial velocity for seismic events localization with FaATSO.

Ultrasonic tomography is conducted by applying high-voltage pulse to sensors sequentially and recording signals at all sensors at the same time. The first step is again picking first arrivals on the receiver sensors. However, there are several differences in the signals recorded in ultrasonic tomography from those in AEs. Since the source sensor is activated by high pulse voltage of 300 V, the signal to noise ratio is high enough for arrival picking. The biggest influence on accurately picking the P-wave arrivals is the cross-talk between the sensors due to the electrical interference in the acquisition system. The cross talk can last for around 7 microseconds, during which the P-wave can travel about 3 cm inside the sample. If the distance between the source and the receiver is smaller than 3 cm, it will be hard to accurately pick the arrivals. Accuracy of the AIC picker also decreases because the voltage time series before the P-wave arrivals are too short after trimming the cross-talk. To increase the accuracy of P-wave arrival picking on the seismic waves in UT, a picker that is based on the high-order-statistics (the HOS picker) ([Lokajíček and Klima, 2006](#)), is employed. It takes a parameter (S_6) computed from the sixth order moment of the seismic waves inside a small time-window that slides along the entire trace from left to right. If S_6 is larger than a certain threshold, the point is picked as the first P-wave arrival. In the HOS picking algorithm, the window length and the threshold are two parameters that can be tuned according to the shape of the waveform, which is principally determined by where the source-receiver pair is placed on the rock sample surface.

Using the picked P-wave arrivals, the velocity between each source-receiver pair and the velocity structure of the sample can be inverted with the FaATSO algorithm ([Brantut, 2018](#)). The theory of the inversion in FaATSO is discussed next. It combines ultrasonic tomography and localization. For ultrasonic tomography explained in this section, the localization related variables in Eq.(3.4) are omitted.

3.2.6 Localization

FaATSO is an inversion code that is capable of simultaneously localizing seismic events and performing ultrasonic tomograph ([Brantut, 2018](#)). Only a brief summary of the methodology is offered here. We also detailed some minor changes needed to adapt to our experimental setup.

The localization and tomography are realized by solving the following non-linear optimization problem:

$$\underline{d} = g(\underline{m}) \quad (3.3)$$

where $\underline{d} = (T_j^{i,UT}, T_j^{i,AE})^T$, $\underline{d} = (V^h, E^h, x_j, y_j, z_j, t_{0,j})^T$. The theoretical arrivals are computed using the fast marching method (FMM) for the eikonal equations in elliptical and weakly anisotropic

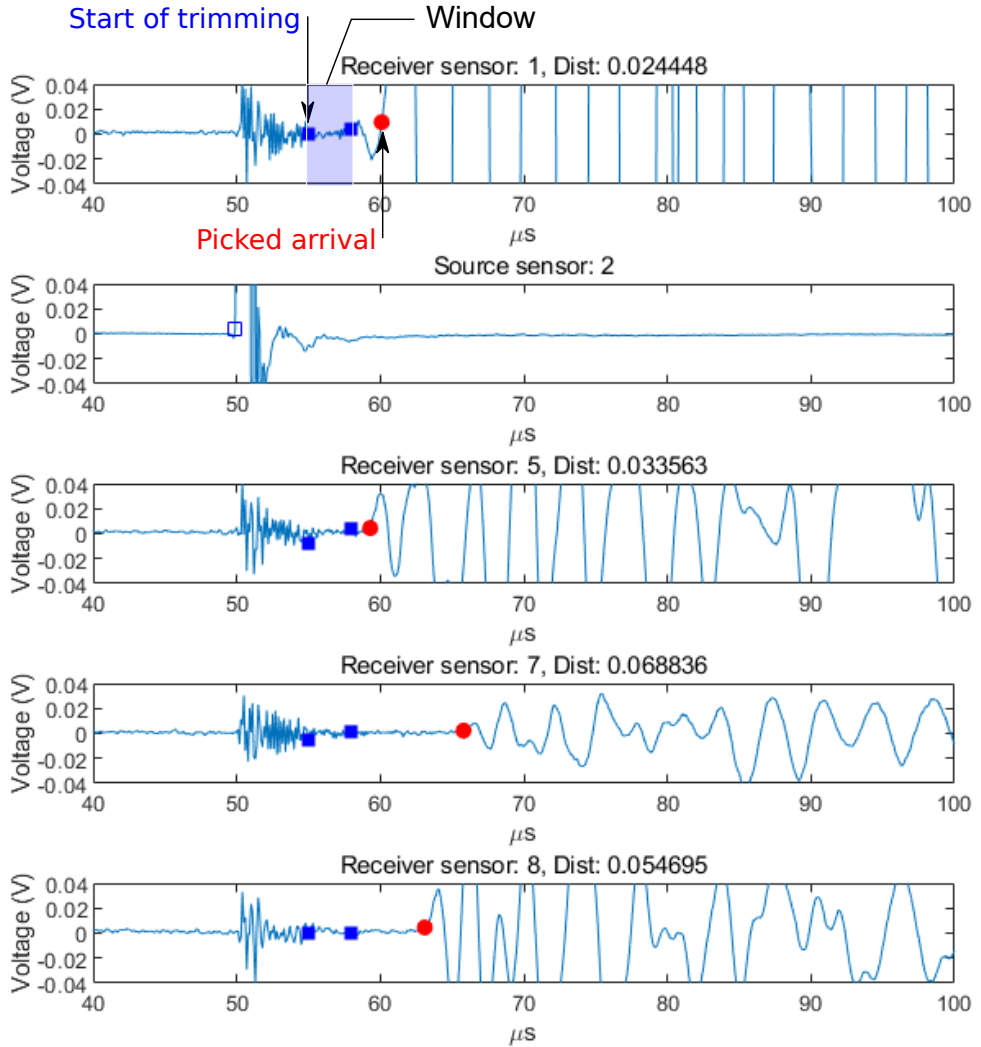


Figure 3.17: Arrival picking using the HOS picker. Sensor 2 is the recordings at the source sensor while signals at four receiver sensors are shown as examples. Blue rectangles are the starting positions of the window for statistical analysis that move from left to right. The picked arrivals are marked with red dots.

Table 3.5: Summary of the parameters used for ultrasonic tomography and events localization in FaATSO.

Parameters	Values	Parameters	Values
σ_{UT}	1 μs	$\sigma_{\ln V}$	0.01
σ_{AE}	0.7 μs	σ_E	0.001
σ_x	0.028 m	$\lambda_{\ln V}$	0.03 m
σ_y	0.028 m	λ_E	0.03 m
σ_z	0.05 m	σ_{t_0}	40 μs

materials with vertical axis of symmetry (Thomsen , 1986). The heterogeneity of the rock sample is also considered in the algorithms. In anisotropic media, it is necessary to discriminate between group and phase velocities and the ray path is no longer perpendicular to the wavefront. The output V^h is the phase velocity and the incidence angle, which will be further discussed in Section 3.2.6, is computed directly from the phase angle.

During the optimization, a least square (L2) cost function is constructed, regularized by the prior knowledge on the model, smoothed by the correlation length for velocity and anisotropy and damped by the estimated variance of the errors in prior knowledge and in arrival recording and picking. The cost function is given as:

$$L2 = (\underline{d} - \underline{g}(\underline{m}))^T \underline{\underline{C}_D}^{-1} (\underline{d} - \underline{g}(\underline{m})) + (\underline{m} - \underline{m}^{prior})^T \underline{\underline{C}_M}^{-1} (\underline{m} - \underline{m}^{prior}), \quad (3.4)$$

where $\underline{\underline{C}_D} = \begin{bmatrix} C_{UT} & 0 \\ 0 & C_{AE} \end{bmatrix}$ and $\underline{\underline{C}_M} = \begin{bmatrix} C_{\ln V} & 0 & 0 \\ 0 & C_E & 0 \\ 0 & 0 & C_{x,y,z,t_0} \end{bmatrix}$. C_{UT} , C_{AE} and C_{x,y,z,t_0} are all

diagonal matrices with the estimated variance of errors in arrival picking for UT (σ_{UT}), for AE (σ_{AE}) and in the prior knowledge on locations (σ_x , σ_y , σ_z) and the times of occurrence of the events (σ_{t_0}). While $C_{\ln V}$ and C_E are full matrix with the expression

$$C_{k,ij} = \sigma_k^2 \left(-\frac{\sqrt{(x_i - x_j)^2 + (y_i - y_j)^2 + (z_i - z_j)^2}}{\lambda_k} \right), k = \ln V, E, \quad (3.5)$$

where i and j here are the grid indices for the meshes of P-wave velocity (V) and anisotropy (E). To make sure the inverted velocity is always positive, the logarithmic of it is used as the model parameters. The optimization is then solved with the Quasi-Newton algorithm with a variable step size μ_n .

The above is a general description of the original algorithm from Brantut (2018). To adapt to our experiment and needs for moment tensor inversion, minor revisions were made to the C++ source code that will be discussed later in result discussion. The parameters used for ultrasonic tomography and events localization are summarized in Table 3.5.

3.2.7 Sensor calibration

The sensors used in LBQ0, LBQ1 and LBQ2 were calibrated with the glass capillary fracture source. A one-centimeter-long, thin-walled glass capillary tube was placed on the top surface of

the steel plate and it was slowly loaded in the direction perpendicular to its longitudinal direction by turning a micrometer (see Figure 3.18). Since the micrometer was also connected to an in-line dynamic force transducer (PCB-208C01), the amplitude of the source-time function could be recorded. While, in practice, the exact shape of the force-time function was not fully captured due to that the frequency resolution of the force transducer was limited to 10 kHz, it could be compensated by the assumed dynamic source-time function of the capillary tube from Breckenridge (1990).

$$\begin{aligned} f(t) &= 0, t < 0 \\ f(t) &= \frac{f_{amp}}{2} \cdot (1 - \cos(\pi t/t_{rise})), 0 < t < t_{rise} \\ f(t) &= f_{amp}, t > t_{rise} \end{aligned} \quad (3.6)$$

where $t_{rise} < 200$ ns.

The above only explains how the source time function is known. To characterize the IR, there is longer story to tell. It started with assuming the IR to be linear and time-invariant. This means the recorded voltage time series $s(t)$ can be expressed as the convolution of the physical displacement at the sensor $u_k(x, t)$ with the IR $i_k(x, t)$:

$$s(t) = u_k(x, t) * i_k(x, t) \quad (3.7)$$

where k is vector index.

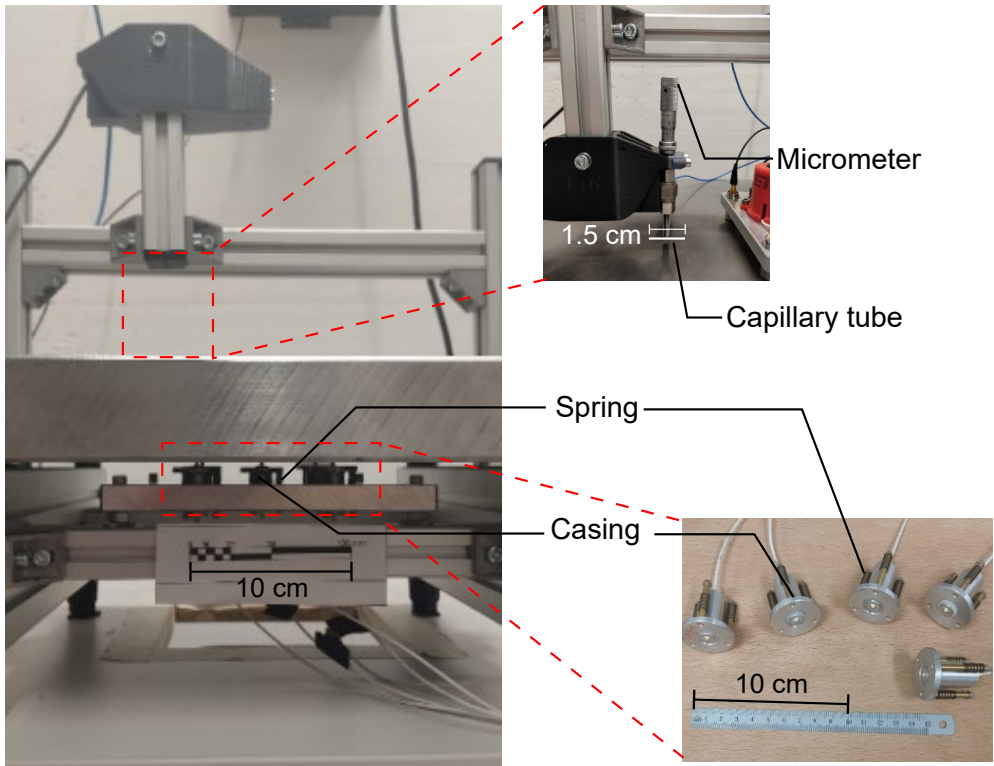


Figure 3.18: Set up of the calibration station. A structure consisting of a casing and three springs is designed to keep the sensors in good contact with the steel plate.

Whereas $s(t)$ can be recorded at the Elsys system, $u_k(\underline{x}, t)$ needs to be estimated from the known source and from how the kinematic motion propagates to the sensors. It is first assumed that point representations are valid at both the sensor and the source. Then, according to the classical theory of dynamic elasticity, the displacement $u_k(\underline{x}, t)$ can be related to the force at a point ξ and time τ through the Green's function $g_{ij}(\underline{x}, t; \underline{\xi}, \tau)$:

$$u_k(\underline{x}, t) = f_i(\underline{\xi}, \tau) * g_{ij}(\underline{x}, t; \underline{\xi}, \tau) \quad (3.8)$$

where the Green's function is computed following the method described in Wu et al. (2020).

Detailed steps on how the frequency spectra of the IR are explained in Appendix B. The IR is not only subjected to the sensor assembly itself, but to the contact mode at the sensor-platen interface and electrical effects (cabling, pre-amplifiers and digitization). Inside the loading cell, the sensors are kept in contact with the surface of the rock by the applied confining pressure. To keep the sensors in similar contact conditions during calibration as those in the experiments, special casings, that apply a known and constant force to the sensor tip via an array of springs, have been manufactured to hold the sensors (see Figure 3.18). In addition, to further flatten the high-frequency IR, a sharper nickel tip has been welded at the tip of the sensors after LBQ0.

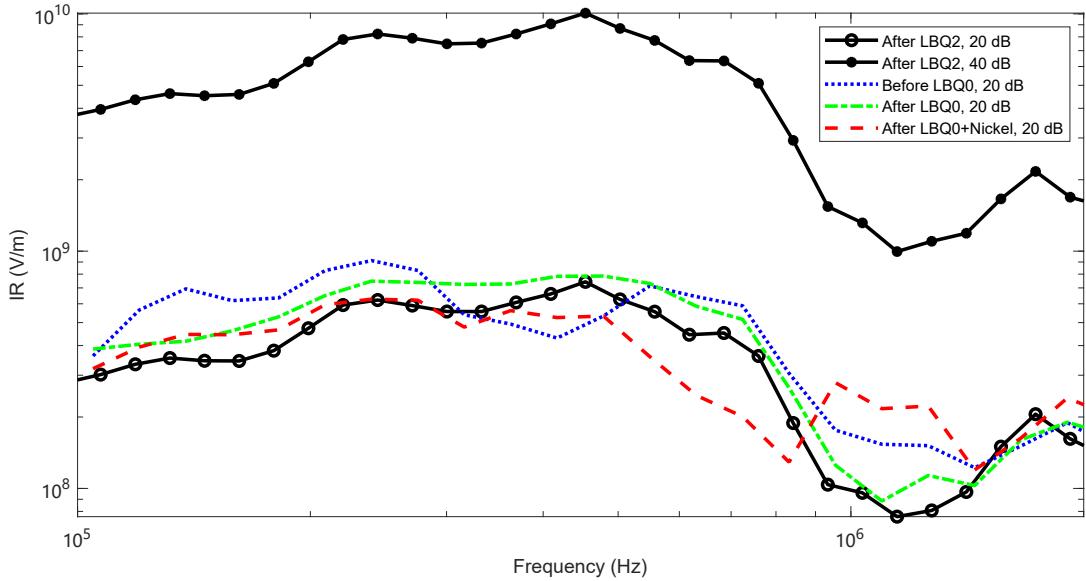


Figure 3.19: IR of the sensor PCT-LBQ-0103 calibrated before and after experiments with 20 dB gain and 40 dB gain. The blue dotted curve is the IR at 20 dB gain before LBQ0. The green dash-dotted curve is the IR at 20 dB gain after LBQ0. The red dashed curve is the IR at 20 dB gain after LBQ0 and with welded nickel tip. The black solid curve with hollow circles is the IR at 20 dB gain after LBQ2. And the black solid curve with filled circles is the IR at 40 dB gain after LBQ2.

Figure 3.19 shows the IR of one of the sensors (PCT-LBQ-0103) used in the experiments. The frequency band in calibration is between 100 kHz and 1 MHz. Before the experiment LBQ0, all the 10 sensors have been calibrated without nickel tips under 20 dB gain from the amplifier. To test the stability of the IRs when the sensors are subjected to loads and possible damage in the cell, the sensors are also calibrated after LBQ0 and LBQ2. Since the AEs were collected under 40 dB gain in LBQ2, the sensors were also calibrated at this amplification level. First, it can be observed that the IR (the dotted, the dash-dotted and the solid-circle curves) is only slightly changed after

LBQ0 and LBQ2. With the addition of the nickel tip applied (the dashed curve), IR around 1 MHz becomes more than two times larger, resulting in a flatter instrument response.

3.2.8 Moment tensor inversion

Moment tensors are analyzed to describe the focal mechanism at the seismic with the point source assumption. The most general condition for the point representation is that the scale of the source should be much smaller than the wavelength. Since the P-wave velocity of the Rotondo granite is usually larger than 3500 m/s and the corner frequency is smaller than 1 MHz, the wavelength would be larger than 3.5 mm. This means as long as the sources are smaller than 1 mm, the moment tensor can appropriately represent the focal mechanisms.

According to Aki and Richard (2002), the point representation of the seismic source in an elastic body is:

$$M_{ij} = C_{ijkl} \frac{A|u|}{2} (l_k n_l + l_l n_k) \quad (3.9)$$

where M_{ij} is moment tensor, C_{ijkl} is the elastic tensor of the medium at the source region, and l_i and n_j are the slip and the normal vector of the fault plane. Convolving it with the analytical Green's function in an elastic, isotropic and homogeneous infinitely large medium, the displacement field reads

$$\begin{aligned} u_n &= M_{pq} * G_{np,q} \\ &= \left(\frac{15\gamma_n\gamma_p\gamma_q - 3\gamma_n\delta_{pq} - 3\gamma_p\delta_{nq} - 3\gamma_q\delta_{np}}{4\pi\rho} \right) \frac{1}{r^4} \int_{r/\alpha}^{r/\beta} \tau M_{pq}(t - \tau) d\tau \\ &\quad + \left(\frac{6\gamma_n\gamma_p\gamma_q - \gamma_n\delta_{pq} - \gamma_p\delta_{nq} - \gamma_q\delta_{np}}{4\pi\rho\alpha^2} \right) \frac{1}{r^2} M_{pq}(t - \frac{r}{\alpha}) \\ &\quad - \left(\frac{6\gamma_n\gamma_p\gamma_q - \gamma_n\delta_{pq} - \gamma_p\delta_{nq} - 2\gamma_q\delta_{np}}{4\pi\rho\beta^2} \right) \frac{1}{r^2} M_{pq}(t - \frac{r}{\beta}) \\ &\quad + \frac{\gamma_n\gamma_p\gamma_q}{4\pi\rho\alpha^3} \frac{1}{r} \dot{M}_{pq}(t - \frac{r}{\alpha}) - \frac{\gamma_n\gamma_p - \delta_{np}}{4\pi\rho\beta^3} \gamma_q \frac{1}{r} \dot{M}_{pq}(t - \frac{r}{\beta}) \end{aligned} \quad (3.10)$$

where γ_n is the direction vector from source to receiver, r distance from source to receiver, α is the P-wave velocity, β is the S-wave velocity and ρ is the density of the medium. When the sensors are far away from the sources (when the distance is much larger than the wavelength), only the terms proportional to $1/r$ dominates. Since only the P-wave is of interests to us so far, Eq.(3.10) simplifies to:

$$u_n = \frac{\gamma_n\gamma_p\gamma_q}{4\pi\rho\alpha^3} \frac{1}{r} \dot{M}_{pq}(t - \frac{r}{\alpha}). \quad (3.11)$$

Assuming that the first arrival P-wave displacement at the sensors can be singled out from the recorded waveforms, the moment tensor can then be related to the displacement time series by taking integral on both side of the Eq.(3.11):

$$\Omega_P = \left\| \frac{\gamma_p\gamma_q}{4\pi\rho\alpha^3} \frac{1}{r} \gamma M_{pq}(t - \frac{r}{\alpha}) \right\|, \quad (3.12)$$

where $\Omega_P = \int_0^{\tau_T} \|u\| dt$ is the integration of the norm of the displacement vector over the rise time (τ_T) of the seismic source. The moment tensors can be inverted with the focimt (Fitch et al., 1980) algorithm embedded in HybridMT (Kwiatek et al., 2016).

The above equations are derived based on the assumption of homogeneity and isotropy. To account for the heterogeneity and the anisotropy considered in tomography and localization, the following assumptions are made:

- In heterogeneous media, the amplitude decays proportional to the inverse of the length of the ray path. More accurately, the geometric spreading of the wave shall be proportional to the inverse of the square root of the multiplication between the ray Jacobian and the group velocity according to Cerveny (2005). However, this value along the ray path is not computed in the package FaATSO that we are using for ray tracing. Adding this to the code could improve the analysis but is not in the scope of this master thesis and is a potential future work that will be further discussed in Section 6.2.
- In anisotropic media, the take-off angle at the source should be taken as the angle between the group velocity vector and the unit vector that is pointing to the negative direction of z -axis since the amplitude of particle movement is changing along the ray path, which follows the direction of the group velocity. Whereas the incidence angle should be taken as the angle between the polarity with the unit vector normal to the surface given that the aim is to compute the magnitude of the displacement at the location of sensors. However, the two angles are still approximated by the angles of the phase velocity. This is also a potential future work that will be further discussed in Section 6.2.

So far, we have discussed how the moment tensors can be inverted in theory. In practice, we also need to extract and collect the input for the inversion from the AE time series. As mentioned in Section 3.2.6, the take-off angle, the incidence angle, the azimuth and the length of the ray paths can be computed by FaATSO leaving the only unknown Ω_p described in Eq.(3.12).

According to Udiás et al. (2014), to account for the rise of the moment tensor from zero to its final value, different shapes of moment release rate (\dot{M}_0) model has been proposed. In our analysis, none of the above shapes of Omega are presumed. The only assumption made is that the moment release rate is kept positive. After calibrating the signals using the method described in Section 3.2.6, the part of the calibrated signals between the P-wave arrival and the first zero-crossing afterwards is considered as the shape of the P-wave. By simply integrating this portion of the signal, we obtain P-wave Omega.

The features of a moment tensor can be represented by its magnitude and its orientation. The magnitude is quantified with the scalar moment $M_0 = (M_1 + M_2 + M_3)/3$, where $M_1 \leq M_2 \leq M_3$ are the three eigenvalues of a moment tensor (Vavryčuk, 2015). The scalar moment shares the same unit as energy and is theoretically related to the volumetric deformation in the emission of seismic waves by Eq.(3.13) (Aki and Richards, 2002).

$$V_{vol} = u \cdot S \cdot \cos \theta_{MT} = \frac{M_0}{K}, \quad (3.13)$$

where V_{vol} is the volumetric deformation, u is the slip length, S is the surface area of the fault, M_0 is the scalar moment, K is the bulk modulus of the rock and θ_{MT} is the angle between the normal and the slip vector given in Eq.(3.14).

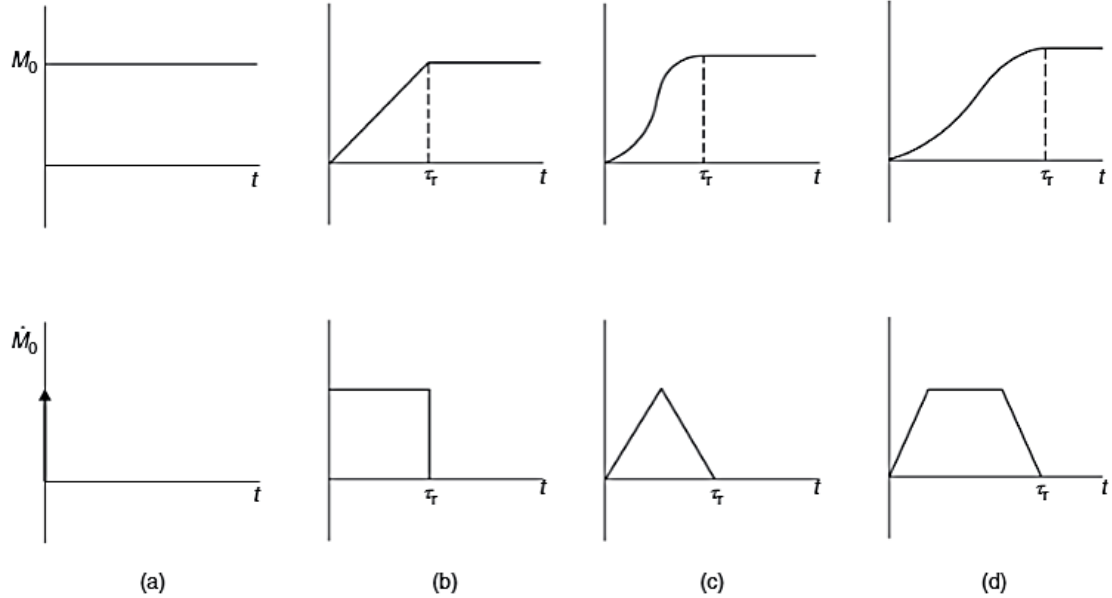


Figure 3.20: Adapted from Udías et al. (2014). Source time function (STF) models for the scalar moment (M_0) and moment rate in the point representation of a seismic source. τ_T is the rise time of the scalar moment.

While the magnitude of the moment tensor indicates the energy released by the source, the latter is related to the source's mechanical properties and to how the fault planes move against each other and, therefore, defines the source type Vavryčuk (2011). To visualize the source type distribution, Hudson plot was proposed (Hudson et al., 1989). It is an equal-area source type plot where the a priori probability (assuming values of the three principal moments of the tensor are independent and uniformly distributed) of the type of the moment tensor is proportional to the geometrical area that this type covers.

For the convenience of the coming discussion, one of the major ways of quantifying the type of source is introduced here. It is elaborated by Vavryčuk (2015) where a moment tensor is decomposed into isotropic (ISO), double couple (DC) and compensated linear vector dipole (CLVD). Each represents a 3-by-3 diagonal matrix with its diagonal being (1,1,1), (1,0,-1) and $1/2 \times (2,-1,-1)$. The ISO component shows the proportion of volume change and the combination of DC and CLVD tell the proportion of constant-volume variation. A source with pure DC component means the fault is slipping along its plane and any source with non-zero ISO or CLVD component will, therefore, contain closing or opening of the fault.

3.2.9 Stress inversion

The notion that the orientations of the fractures nucleating and propagating in rocks are subjected to the stress field dates back to Anderson (1951). Wallace (1951) and Bott (1959) then propose that the slip vector is parallel to the tangential shear traction on the fault. Following this idea, Michael (1984), Gephart and Forsyth (1984), and Jacques (2002) develop commonly used methods to solve for the stress tensor given a set of focal mechanisms. These methods assumed that all of the focal mechanisms developed under the same stress field. However, the validity of this assumption depends on the relationship between the scale of stress heterogeneity and the size of the faults. To deal with the heterogeneous stress field, the method has been extended to invert stress field on

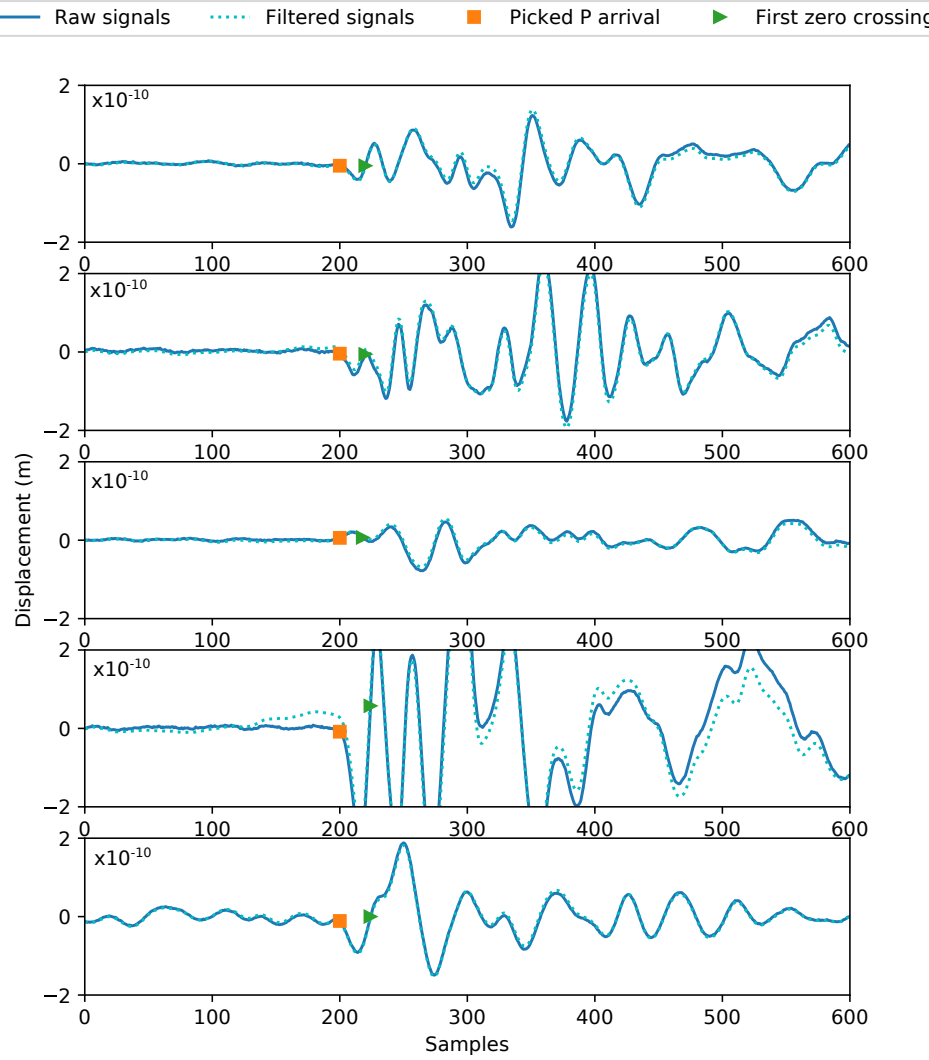


Figure 3.21: Example of the calibrated signals where the P-wave arrivals and first zero-crossings are marked with orange rectangles and green triangles. The P-wave Omega is computed by integrating the curve between the arrivals and the first zero-crossings.

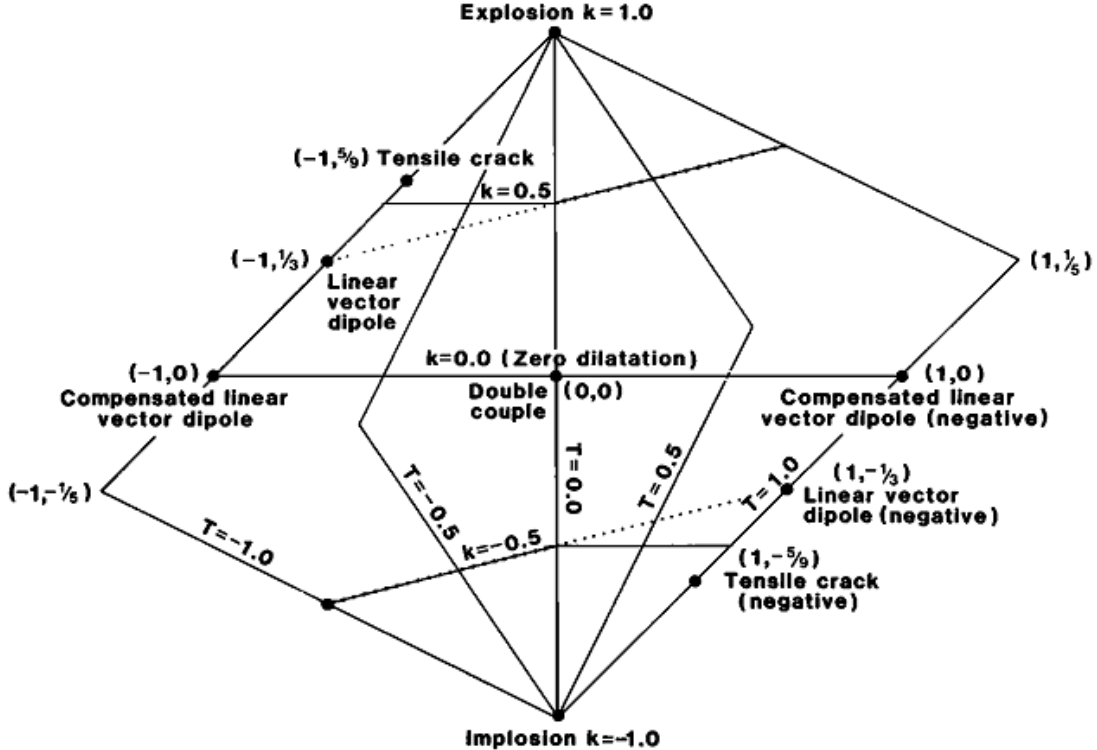


Figure 3.22: The equal-area source type plot adapted from [Hudson et al. \(1989\)](#). The types of events represented by special points on the diagram are marked.

structured ([Hardebeck and Michael, 2006](#)) and unstructured ([Li and Du, 2020](#)) grids. The most prominent advantage of the latter method is that it can account for the non-uniform distribution of seismic events during the failure of the rocks. The unstructured stress inversion is therefore adopted here to estimate the stress field around the micro-seismic events. Like all the stress inversion that based on the physics proposed by [Wallace \(1951\)](#) and [Bott \(1959\)](#), only the deviatoric component of the stress tensor, representing the orientation of the stress field, can be estimated.

The methods of unstructured stress inversion proposed by ([Li and Du, 2020](#)) are introduced here. Nodes of the unstructured grid according to the distribution of events are placed at the center of the clusters derived using the k-mean clustering algorithm ([Hartigan and Wong, 1979](#)). The inputs for the stress inversion are the slip vectors of each micro-seismic events. In 3D geometry, they can be related to the moment tensors by the following equations when assuming isotropy of the elastic tensor:

$$\begin{aligned} n &= \sqrt{\frac{M_1 - M_2}{M_1 - M_3}} e_1 \pm \sqrt{\frac{M_3 - M_2}{M_3 - M_1}} e_3 \\ l &= \sqrt{\frac{M_1 - M_2}{M_1 - M_3}} e_1 \mp \sqrt{\frac{M_3 - M_2}{M_3 - M_1}} e_3 \end{aligned} \quad (3.14)$$

where e_1 and e_3 are the eigenvectors of a moment tensor corresponding to M_1 and M_3 , respectively. Due to the interchangeability of the normal and slip vectors, supplementary information on the micro-seismic event is required. [Vavryčuk \(2014\)](#) proposed that the two vectors can be differentiated from each other using the local stress field with the instability factor.

$$\begin{aligned}
I &= \frac{\tau - \mu(\sigma_n - 1)}{\mu + \sqrt{1 + \mu^2}} \\
\sigma_n &= n'_1^2 + (1 - 2R)n'_2^2 - n'_3^2 \\
\tau &= \sqrt{n'_1^2 + (1 - 2R)^2n'_2^2 + n'_3^2 - [n'_1^2 + (1 - 2R)n'_2^2 - n'_3^2]^2}
\end{aligned} \tag{3.15}$$

where μ is the coefficient, σ_n and τ are the normalized normal and shear stress, $R = (\sigma_1 - \sigma_2)/(\sigma_1 - \sigma_3)$ is the stress ratio and n'_i^2 is the projection of the direction of the i -th principal stress on the normal vector of the source.

The instability factor in Eq.(3.15) renders the slip vectors and the stress field interdependent and means that they should be solved at the same time. The following algorithm has been proposed to solve them iteratively. A first attempt is that stress field around the events in the same cluster is uniform. Since the orientation of a stress tensor can be determined with 5 elements and each seismic event can provide one constraint, at least 5 events should be included in each cluster. In our implementation, each cluster consists of at least 10 events. The formulation that relates slip vectors to stress field is derived from the least square cost function with a smoothing term:

$$(G_{ALL}^T G_{ALL} + e^2 D^T D) \underline{\underline{m}_{ALL}} = G_{ALL}^T \underline{\underline{d}_{ALL}} \tag{3.16}$$

where G_{ALL} is a blocked diagonal matrix in which each block is a $3w \times 5$ matrix that relates the stress field to the moment tensors in a events cluster, w being the number of events in this cluster. D is a blocked damping matrix that regularize stress difference between different clusters by their distances. The assumption behind the regularization is that the closer the two clusters, the smaller the stress should vary. e^2 is the parameter that controls the level of stress regularization that needs to be adjusted in the analysis.

To solve this equation, slip vector of an event is initially arbitrarily chosen between the two vectors in Eq.(3.14). The solved stress tensors are then used to compute the instability factors for the two possible slip vectors of every event. The vectors that result in larger instability factors are then substituted into Eq.(3.16) to get ready for the next iteration. During the iteration, the stress ratio R is selected as the indicator for convergence. Once the change in R is less than 5% between two subsequent iterations, the algorithm will stop and return the inverted stress tensors at each node and the differentiated slip vectors of each event.

3.2.10 Fiber optics technique

While distributed fiber optics strain mapping in tri-axial configuration significantly increases the spatial resolution of strain field (Salazar et al., in preparation), interpolation algorithms are still required to represent the continuous strain field with the FO measurements. Due to existence of AE sensors, the fiber optics cables cannot cover the entire surface of the rock sample. The interpolation in space is completed with a piecewise cubic, continuously differentiable and approximately curvature-minimizing polynomial surface (Nielson, 1983). In terms of temporal resolution, the sampling intervals of the fiber optics were 8 seconds in LBQ0-2.

The axial and radial fiber optics cables directly measure the axial (ε_{zz}) and hoop ($\varepsilon_{\theta\theta}$) strain distribution. Assuming equal radial (ε_{rr}) and hoop strain, the volumetric surface strain field (ε_{vol}) can then be estimated using Eq.(3.17) from the interpolated data in the measured two directions.

$$\varepsilon_{vol} = \varepsilon_{rr} + \varepsilon_{\theta\theta} + \varepsilon_{zz} \quad (3.17)$$

The results of FO measurements will be shown in Section 4.5 and will be compared with the localization, moment tensor inversion and stress inversion results in the Discussion part of the thesis.

3.2.11 Methods of statistical analysis

From the MT analysis, each AE event is characterized by a moment tensor with six independent variables (M_{pq}). The study of seismic statistics consists of understanding how these six variables are distributed in time and the 3-dimensional space. In this thesis, the seismicity is analyzed from the following three aspects.

1) Frequency magnitude distribution (FMD) is an important feature of a seismic catalog. It has been found to follow the Gutenberg and Richter (GR) relationship (Gutenberg and Richter, 1944) in Eq.(3.18).

$$\log_{10} N = a - bM \quad (3.18)$$

where N is the number of events larger than the magnitude M . The analysis in this thesis will focus on the moment magnitude ($Mw = 2/3 \log_{10} M_0 - 6.03$ according to Kanamori (1978)) in the discussion of FMD. While the value of a reflects total seismicity rate of the region, b -value is an important factor that may indicate probability of occurrence of strong events and is observed to probably depend on many factors, e.g. the fault type (Petrucelli et al., 2018), stress field (Scholz, 2015), fractal dimension of seismicity (Lei and Ma, 2014). GR relationship assumes a self-similar scaling but due to the noise level, the frequency band of AE sensors or the poor sensor coverage, FMD can deviate at a certain magnitude (M_c), which is usually called the magnitude of completeness. A quantitative criterion can be applied to assess M_c , where the goodness of fit to an assumed power law is measured (Wiemer and Wyss, 2000).

2) Modified Omori's law:

$$\begin{aligned} R_a &= K_a(c_a + t - t_m)^{-p} \\ R_f &= K_f(c_f + t - t_m)^{-p'}, \end{aligned} \quad (3.19)$$

where R_a and R_f are aftershock and foreshock occurrence rate, $t - t_m$ is the time to failure and the other parameters are to be fitted with data (Utsu, 1961; Utsu and Ogata, 1995). Since in the compression of an intact rock the entire rock fails during the major shock and no aftershock seismicity is measured, only temporal distribution of the foreshock sequence is studied. The foreshock occurrence rate is plotted against the time to failure and the coefficients in the equation are probed with curve fitting at the log-log scale.

3) Fractal dimension: In terms of spatial distribution, the concept of fractal dimension of the event locations is incorporated. To compute the fractal dimension, the q -th order correlation integral is defined as a function of the threshold distance between events (r):

$$C_q(r) = \frac{1}{N} \left[\sum_{j=1}^N \left(\frac{N_j(R \leq r)}{N-1} \right)^{q-1} \right]^{\frac{1}{q-1}}, q = -\infty, \dots, -1, 0, 1, \dots, \infty, \quad (3.20)$$

where N is the total number of AE events, $N_j(R \leq r)$ is the number of hypocenter pairs separated by a distance equal to or less than r . If the distribution of AE events is fractal, C_q would be proportional to r^{D_q} , where D_q is the fractal dimension. For a uniformly distributed AE events on a 2D plane, the fractal dimension is expected to be 2, while D_q will drop if clustering exists. The fractal dimension can also change in time due to various reasons associated with the nucleation and propagation of the fracture in the sample. To explore temporal distribution of the fractal dimension, a bin with 150 events, that moves from the first event in time to the final one, is chosen in our analysis. In each bin, the fractal dimension is approximated using linear curve fitting at log-log scale and the time is determined from the mean of the events in the bin ([Goebel et al., 2017](#)).

Comparison between the accumulated moment and moment release rate using these metrics will be shown and discussed in Section 4 and 5.

Results

In this section, results from the three experiments will be summarized to shed light on how aseismic and seismic deformation are correlated with the progressive failure of the Rotondo granite. The focus of this section is on LBQ2 since LBQ0 and LBQ1 were mainly conducted to optimize acquisition parameters as discussed in Section 3.1. Though the P-wave velocity of Rotondo granite under zero confinement has been studied by David et al. (2020), the variation of velocity can be as much as ± 300 m/s and it is still unclear how the velocity structure changes with loading. This will be investigated in Section 4.1. We will also investigate changes in velocity with the progressive failure. We then use the understanding of the velocity structure to determine the spatio-temporal distribution of AE events in Section 4.2 and use the distribution to make a tentative deduction on the progressive failure and the formation of the macrocracks. Types and magnitudes of the events will be looked into in Section 4.3, 4.4 and 4.5 in combination with the high-resolution strain field measured with the fiber optics technology for the first time.

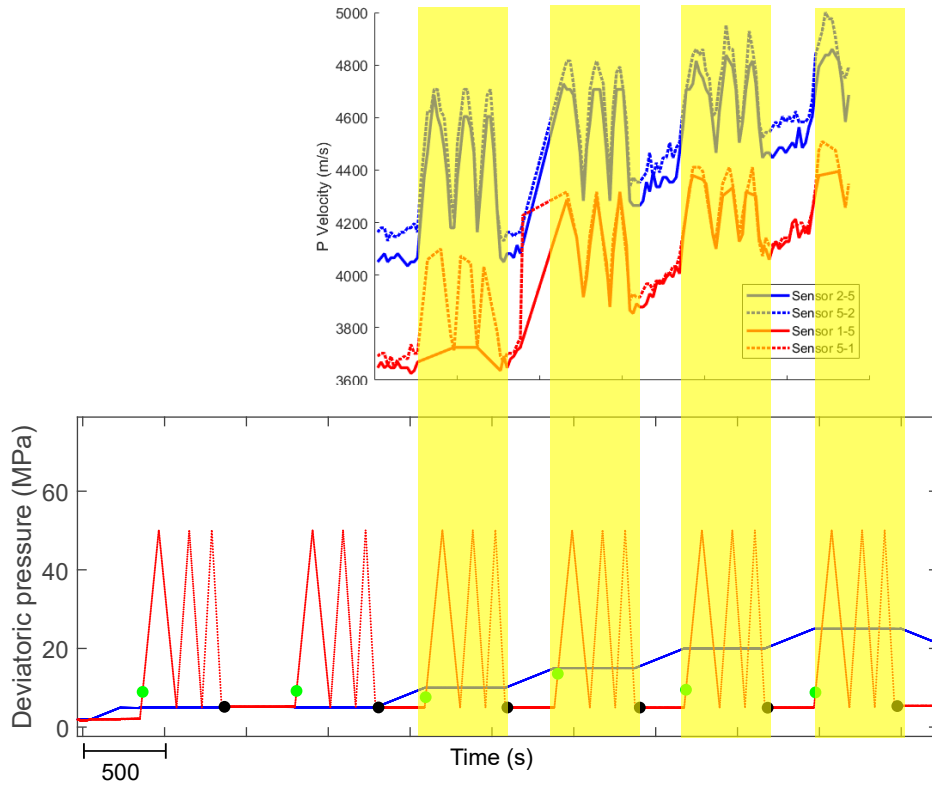


Figure 4.1: Change of the P-wave velocity with the confining pressure and with the deviatoric stress in LBQ0, which is also representative of the observations in LBQ1.

4.1 Change of velocity structure

4.1.1 Velocity change during the cyclic loading

In LBQ0 and LBQ1, cyclic loading at different confining pressure steps is conducted at the beginning of the experiments. We investigated how the P-wave velocity of the intact Rotondo granite changes with confining pressure and with the cyclic loading of the deviatoric stress. Figure 4.1 shows how P-wave velocities vary between two example sensor pairs in LBQ0, which can also represent results in LBQ1. We can tell that as the deviatoric stress increase from 5 MPa to 50 MPa, the P-wave velocity can increase by as much as 500 m/s; whereas every 5 MPa increment in the confining pressure can lead to a 100 to 200 m/s rise in P-wave velocity. The velocity is more than 2 times as sensitive to the confining pressure as to the deviatoric stress. The increase in velocity is majorly due to the closure of micro-cracks inside the rocks (Nasseri et al., 2013). It is also observed that as the confining pressure increases, the sensitivity of velocity to loads drops. Shapiro (2003) explained such non-linear dependency of the velocity on confining pressure with the theory of poroelasticity.

4.1.2 Ultrasonic tomography during the failure test

Figure 4.2 shows how the velocity structure in LBQ1 has changed during the failure test. With the closure of cracks, the velocity increased until the deviatoric stress reached around 100 MPa. As the deviatoric stress further increased, the velocity did not change too much until the deviatoric stress rose up to around 300 MPa at around 1500 s when it started to drop and the level of heterogeneity continued to increase until the failure of rock at around 1630 s.

Ultrasonic tomography was performed every 100 s in both LBQ1 and LBQ2. Due to the difference in loading history and in rock micro-structure, the variation of velocity structure is very different between two experiments. This is demonstrated in Figure 4.3. In LBQ1, the velocity can vary for more than 700 m/s (from 100 s to 1600 s) whereas the change is at most 400 m/s in LBQ2. Such difference between the two experiments will also manifest itself in the localization results and will be discussed in the following section.

4.2 Localized events

Accuracy of events localization with FaATSO is examined to assess the reliability of the distribution of events shown later. The tomography terms in Eq.(3.4) is neglected and the relation between the arrivals at the sensors and the location of an event is:

$$\delta T = \frac{\partial T}{\partial \underline{m}^{pos}} = \underline{\underline{G}}'(\underline{\underline{m}}^{pos}) \delta \underline{\underline{m}}^{pos}, \quad (4.1)$$

where $\underline{\underline{G}}'(\underline{\underline{m}}^{pos})$ can be computed in the following way:

- Generate a mutually orthogonal mesh in the cylinder and scatter events on the nodes of the mesh. The grid size of the mesh is chosen to be 1 mm;
- Compute the travel times, using the velocity structure inverted from the combined localization and tomography, between all the event-sensor pairs, which yields on the discretized

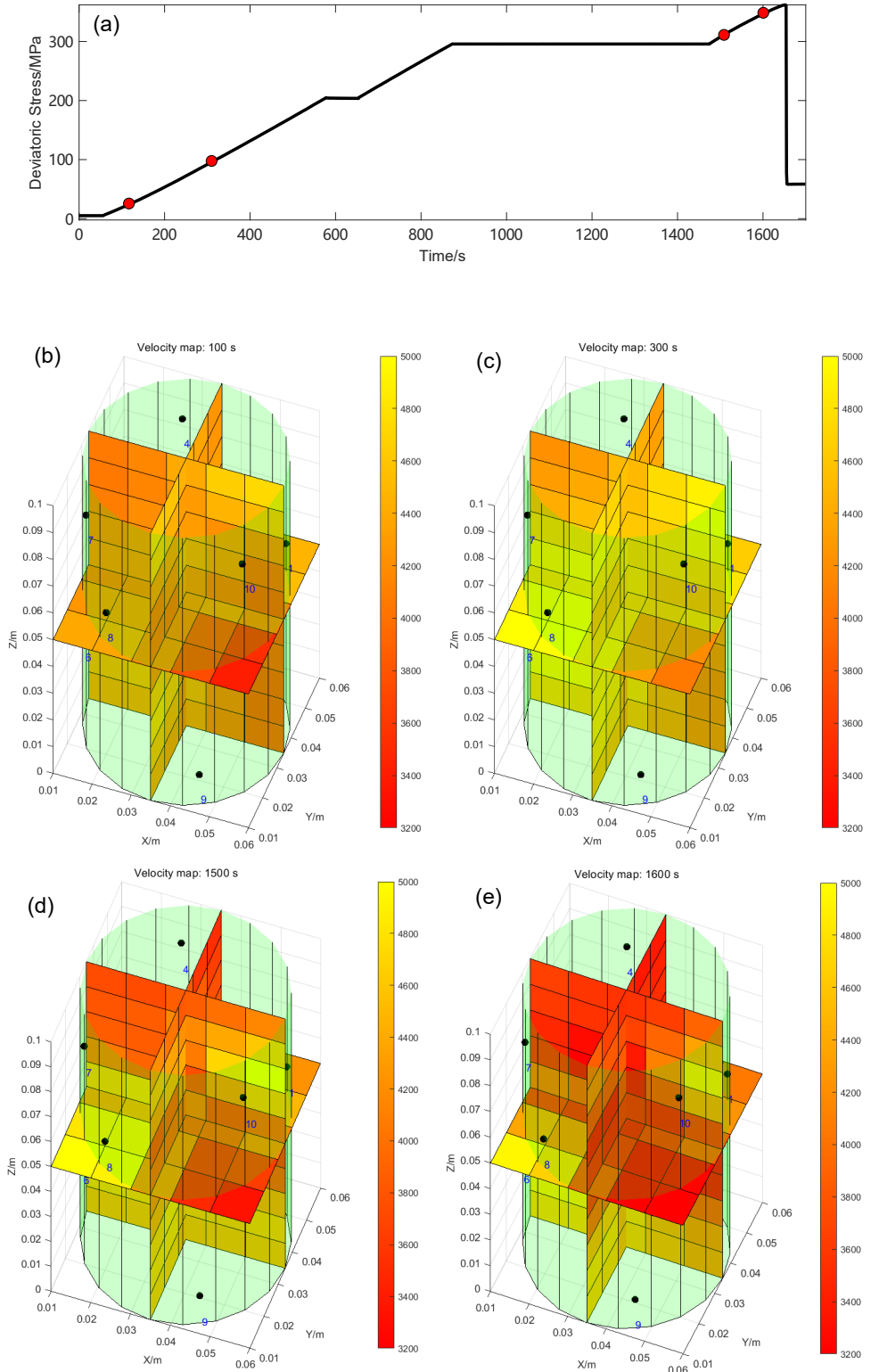


Figure 4.2: The change of the 3D velocity structure of the sample in LBQ1 as the axial stress increased from 5 MPa to around 300 MPa calculated with FaATSO. The times of tomography results shown in (b)-(e) are marked in (a) with four red dots.

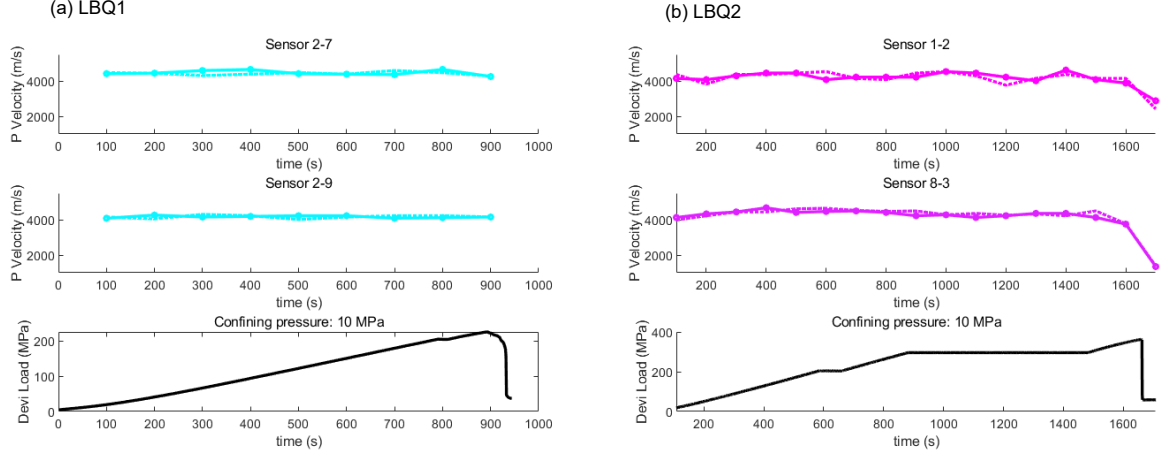


Figure 4.3: The change of P-wave velocity between two selected sensor pairs in LBQ1 (left) and LBQ2 (right). While the ray paths between sensor 3 and sensor 8 in LBQ1 and between sensor 2 and sensor 7 in LBQ2 cross the fault planes proposed according to the localization results, the other two ray paths are most likely not passing any major faults.

grids;

- Compute the derivatives of the arrival time at the i -th sensor to the change in location in all three directions at the body center of each unit cubic;
- The derivative as a function the locations of events can then obtained on the discretized field.

With $\underline{G}'(\underline{m}^{pos})$, a spatial distribution of how and δT are $\delta \underline{m}^{pos}$ interdependent can be obtained by solving a forward and an inverse problem. The forward problem gives how changes of the events locations influence arrivals at all the sensors, whereas the inverse problem solves how the errors in the arrival picking can influence the simplified version of localization.

The results of sensitivity analysis are shown in Figure 4.4. From Figure 4.4a, it is known that the arrival time is generally less sensitive to the location errors at the center of the sample. Errors of 1 mm in the location ($\delta \underline{m}^{pos}$) corresponds to errors between 0.2 and 0.3 microseconds at the sensors.

The localization errors that can be inferred from Figure 4.4b is more direct. If errors in the arrival picking is typically a few microseconds, errors in localization with 10 sensors will be around 1 mm. Apart from the above analytical evaluation, accuracy of FaATSO in localization was also tested using ball drop experiment and some details can be found in Appendix A. From this experiment, the localization errors are estimated to be less than 5 millimeters.

Localization results in LBQ1 and LBQ2

Theoretically, with carefully picked arrivals in Section 3.2.4, no event should be located outside of the cylinder. To strictly prevent this from happening, an additional step was implemented in the FaATSO code after the update of events locations in each iteration. If the events are updated outside of the cylinder, it will be pulled back to the closest point on the surface of the cylinder. Then, the direction of update in the next iteration will proceed with the corrected locations.

Data in LBQ1 and LBQ2 were collected with the same number and distribution of AE sensors; however, the spatial-temporal distribution of events was very distinctive. In LBQ1, the events were almost randomly scattered across the sample until around 1600 s. Such randomness and existence of AEs more than 100 seconds before the failure of the entire sample in LBQ1 might correspond to the observation of more apparent drop in P-wave velocity mentioned in Section 4.1. Since around

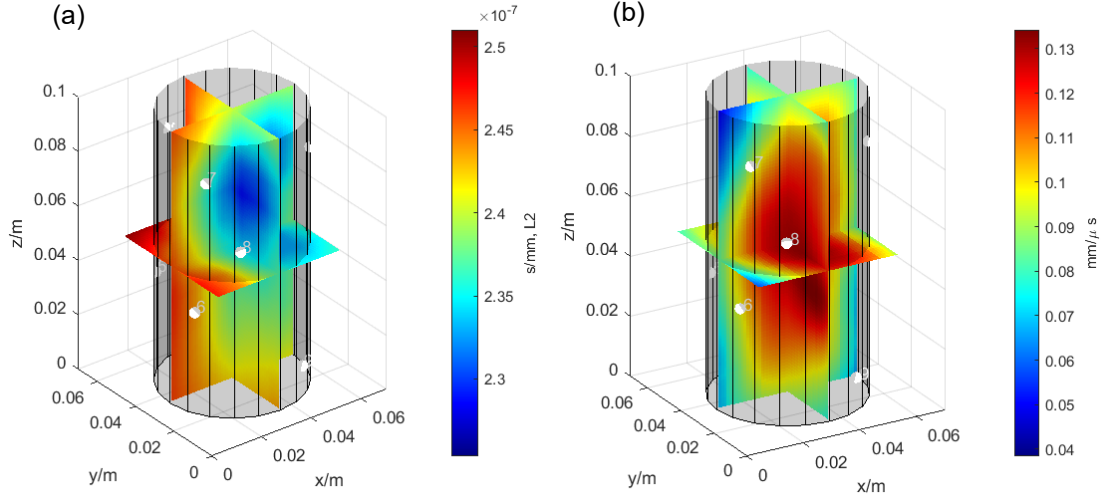


Figure 4.4: (a) Spatial distribution of the geometrical means of the changes at the 10 sensors (white dots) if the location of the event at a point is moved for 1 mm. (b) Spatial distribution of the geometrical mean of location errors resulted from 1 micro-second error in arrival picking at ten sensors.

1600 s, events start to concentrate at two regions (the clusters of yellow dots) near the surface of the sample. Within a few tens of seconds, events inside the two regions extended from the regional center and led to the failure of the sample.

Unlike LBQ1, events were already focused at a region near the center of the sample once they started to occur since around 850 s in LBQ2. The cluster propagated upward for around 50 seconds as the deviatoric stress reached its peak. The position of the loading piston was then held and the damage was allowed to develop without adding energy to the system. Within around 30 seconds, the cluster propagated downward along a different direction until a sudden drop of deviatoric stress occurred. Through the entire experiment, the distribution of events in LBQ2 is prominently more focused.

Such distinctive events distribution is the outcome of the difference micro-structure, the varied loading protocols and the potential leak in the jacket in LBQ2 (see Figure 3.9) that equalized the confining pressure applied to the inner and outer surface of the jacket.

Apart from the locations of the seismic events, information on the ray path is also an essential output of the FaATSO code for the following moment tensor inversion. While the ray path is already traced in the original code by Brantut (2018), writing of the necessary information into the readable format for MT inversion is added to the code. The information includes the take-off angles at the source, the incidence angles at the receivers and the length of the ray path.

4.3 Magnitudes and types of moment tensors

The magnitudes of the moment tensors from LBQ2 are shown in Figure 4.6. From the FMD plot, the b-value is estimated as 0.88 ± 0.02 with a magnitude completeness of Mw -7.9. This magnitude is at the same scale that grains of a few millimeters can generate (Manthei and Plenkers, 2018), which is the size of the most minerals in Rotondo granite (Rast, 2020). It is also observed that the data significantly deviates from the fitting results at the magnitude larger than around Mw -6.5.

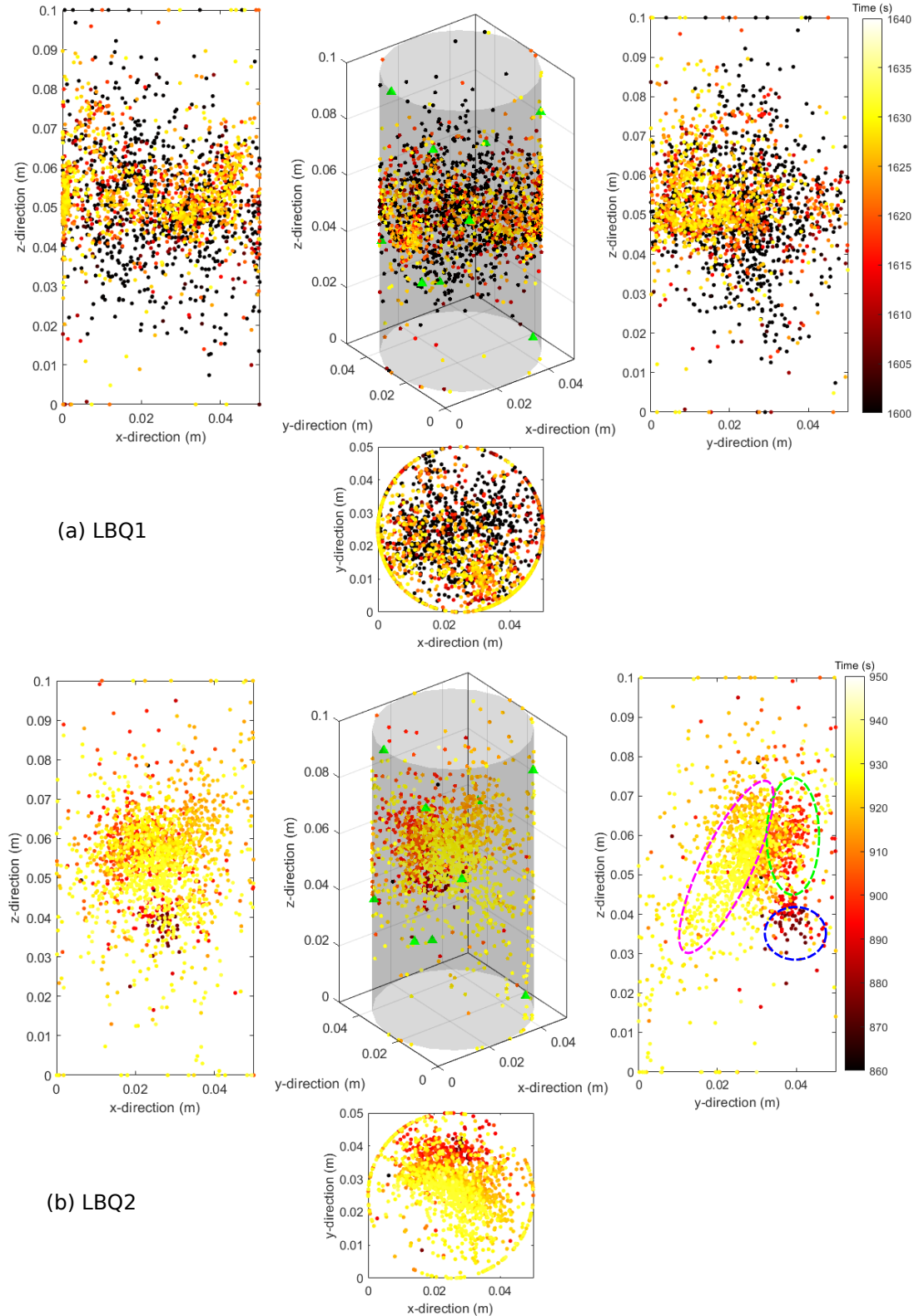


Figure 4.5: Locations of events in LBQ1 (a) and LBQ2 (b). The events are color-coded according to their time of occurrence. The three dashed circles in (b) marks the clusters mentioned in Figure 4.6c.

More experiments are required to understand if this deviation at large magnitude is introduced by the physics of the sample failure or from the processing methodology. We noticed that early in the loading, events of large magnitude occurred and resulted in swarms of earthquakes (Mogi, 1966) and a step increase in the cumulative seismic moment. However, most major events are observed in the few seconds before the failure of the entire sample. From the swarms of earthquakes in Figure 4.6c, three major groups, between which no event occurs, are observed. The average magnitude and the number of events in each group increase with time. The first group between 870 and 880 s contains only a few events and is located at the bottom of the events cluster that propagated upward (see Figure 4.5b), probably related to the initial coalesce of microcracks. The second group occurs between around 890 and 900 s along with the upward propagation of events. After 900 s and before the eventual failure of the sample, much more events appear and corresponds to the migration of events downward along the changed direction.

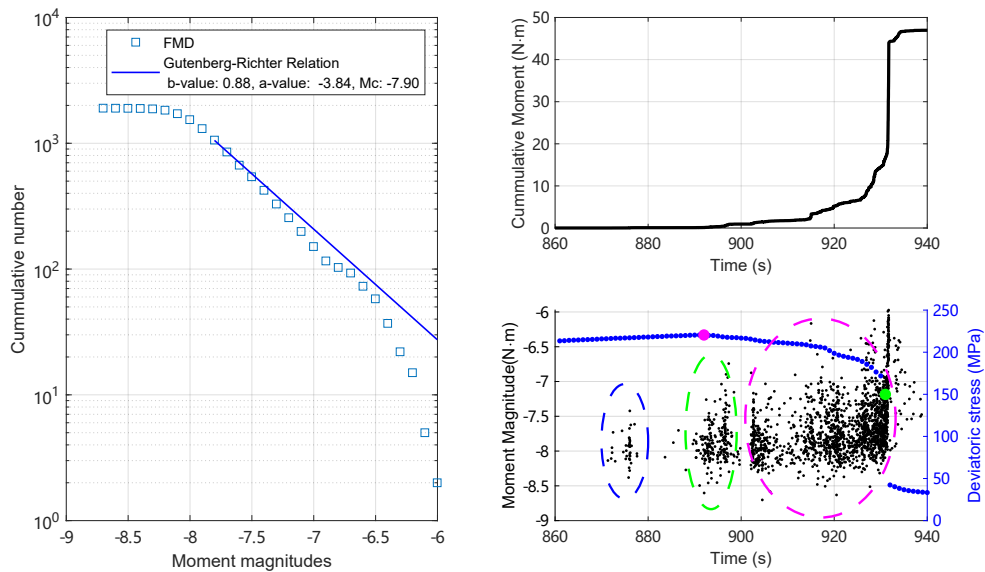


Figure 4.6: (a) Fitting of the frequency magnitude distribution of the events with estimation of the magnitude of completeness. (b) The cumulative moment release in time. (c) The magnitude of all events over time. The three dashed circles in (b) marks the clusters mentioned in Figure 4.5b.

Types of events for the full seismic catalog and for each swarm of seismic events circled in Figure 4.6c are shown in Figure 4.7. The Hudson plot shows that most events have little isotropic component and are distributed along the line between the positive and the negative linear vector dipole. From the first swarm to the third swarm, the proportion of events that are expansive increases. Similar distributions have also been shown in the numerical modeling results of van der Baan and Chorney (2019). While many events do not have high double couple (DC) components, orientations of the DC component can still show how the direction of the fault slips along the fault planes with the triangle diagram proposed by Frohlich and Apperson (1992). As shown in Figure 4.7b, normal fault is the dominant fault type. This is consistent with the loading scheme where the highest compressive stress is along the axial direction of the sample.

4.4 Stress inversion

We employed the unstructured inversion from Section 3.2.9 in LBQ2.

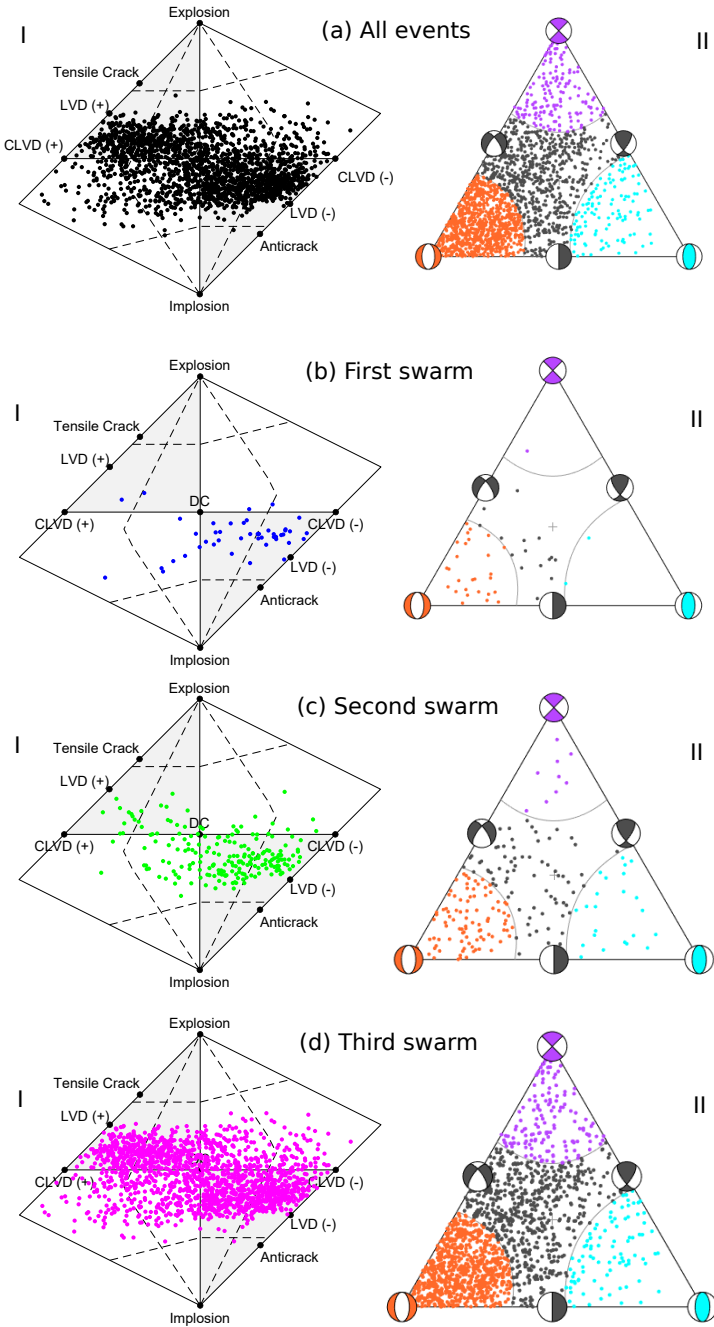


Figure 4.7: (a- to d-I) Hudson plots for the full seismic catalog (a-I) and the events in each seismic swarm (b- to d-I) marked in Figure 4.6c. Dots are plotted in colors corresponding to those in Figure 4.6c. (a- to d-II) The triangle diagrams for the full seismic catalog (a-II) and the events in each seismic swarm (b- to d-I) marked in Figure 4.6c. The orange beach ball and dots are categorized as normal faults, the cyan beach ball and dots as reverse fault and the red beach ball and purple dots as strike-slip fault. The gray beach balls and dots mark events that are mixtures of these three major types of DC events.

As observed in Section 4.2, the events form three distinct bursts from two large scale structures. The first structure occurs before around 898 s while the second shows up afterwards. So far, it is still uncertain if the structures are large scale faults propagating in the sample. The results of unstructured stress inversion before and after 898 s are shown in Figure 4.8a and 4.8b. The color-coded events in the top-middle subplots show how the events are clustered prior to the stress inversion. The other three subplots surrounding them give the orientations of each cluster viewing from three perspectives. “Principal vector 1” (green arrows) and “Principal vector 3” (red arrows) correspond to the direction of the largest (most tensile) and the smallest (most compressive) eigenvalues, respectively. In both Figure 4.8a and 4.8b, the red arrows point in the directions roughly parallel to the z -axis. This is in agreement with the compressive deviatoric stress applied in the axial direction. Focusing on the green arrows in both subfigures, it is further found that the orientations of the green arrows are almost perpendicular to the lines formed by the events in x - y plane. Comparing between the two subfigures, the green arrows are generally rotated clockwise after 898 s. The orientations of the eigen vectors provide additional hints on the fault geometry and will be detailed discussed in Section 5.2.

To quantitatively estimate the variation in the orientation of “Principal vector 1” in time, a one-second window, that spans time between 892 and 896 s and between 920 and 931 s, is applied on the events. The time interval between 896 and 920 s is not considered due to insufficient numbers of events for stress inversion. The stress field is inverted using that same method above and the orientation of “Principal vector 1” is represented by its angle between the positive direction of x -axis with positive counterclockwise angles. This angle is termed as the “orientation angle” in this section for the convenience of discussion. Average of the orientation angles of the clusters is shown with the solid green curves in Figure 4.8c. It is found that the orientation angle oscillates around 70 degrees between 892 and 896 s whereas maintains a relatively constant value of 40 degrees between 920 and 931s. This indicates the stress field has been re-oriented by roughly 30 degrees after 898 s. These results are combined next with the estimates of the peripheral strain field of the specimen measured from the fiber optics technology.

4.5 Strain field

Figure 4.9 shows the strain field and the locations of the events prior to the sudden drop of stress at around 931 s. It can be found that the local peaks in the strain field coincide with the approximate locations where seismic events are focused. The match between locations of events and strain field measurement provides a preliminary qualitative insight into the fracturing process. From 890 s to 898 s, clusters of events migrate upward, accompanied by the increase of hoop strain (the red and yellow region in Figure 4.9c and 4.9d) on the side of the surface close to the clusters. The event clusters then propagate downward and in the positive direction of x -axis, leading to the expansion of high hoop strain region (the yellow and white region in Figure 4.9e to 4.9j) in the same direction.

The variation of heterogeneous strain field provides details about how the sample has been deformed as it approaches failure. These results show preliminary efforts into linking seismic deformation from AEs and aseismic deformation from FO. As illustrated in Section 3.2.8, the moment release rate tells the seismic deformation averaged across the entire sample and can be compared against the averaged aseismic deformation. Figure 4.10 shows the temporal evolution of the averaged axial strain (the solid black curves) measured from vertical FO sensors, hoop strain from horizontal FO sensors and volumetric strain computed from Eq.(3.17). The error bars show the standard deviation of the strain across the sample. With the increase of compression in axial direction, the axial and the hoop strain grow negatively and positively, respectively, meaning the sample

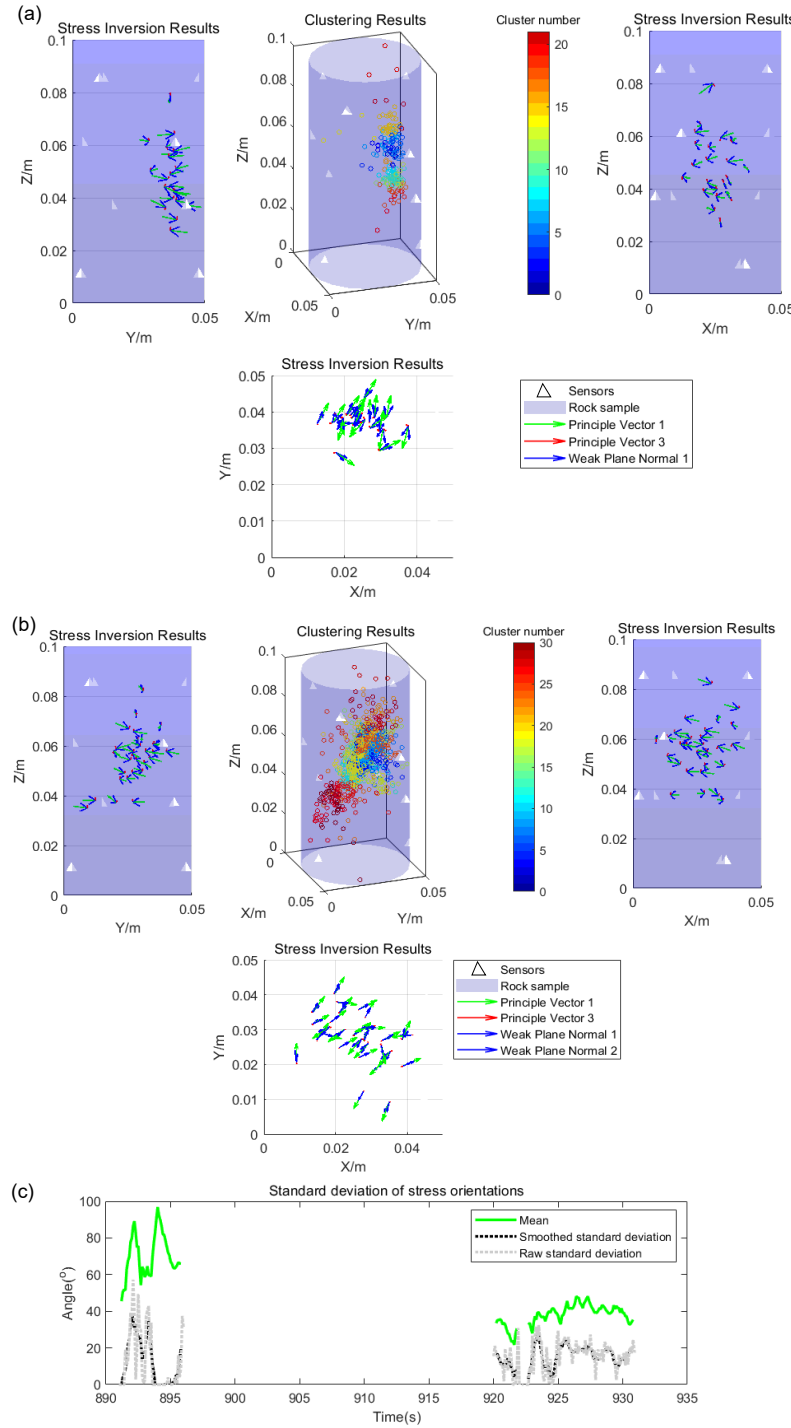


Figure 4.8: (a) Stress inversion results for the events occurs before 898 s in LBQ2. The color-coded events in the top-middle subplots show how the events are clustered for stress inversion. The other three subplots surrounding them give the orientations of each cluster viewing from three perspectives. “Principal vector 1” (green arrows) and “Principal vector 3” (red arrows) correspond to the direction of the largest (most tensile) and the smallest (most compressive) eigenvalues. (b) Stress inversion results for the events occurs after 898 s in LBQ2. (c) Temporal variation of orientation angles of the clusters in each one-second window. Average of the orientation angles is plotted in solid green curves, while the raw and smoothed standard deviations are plotted in dashed gray and black curves.

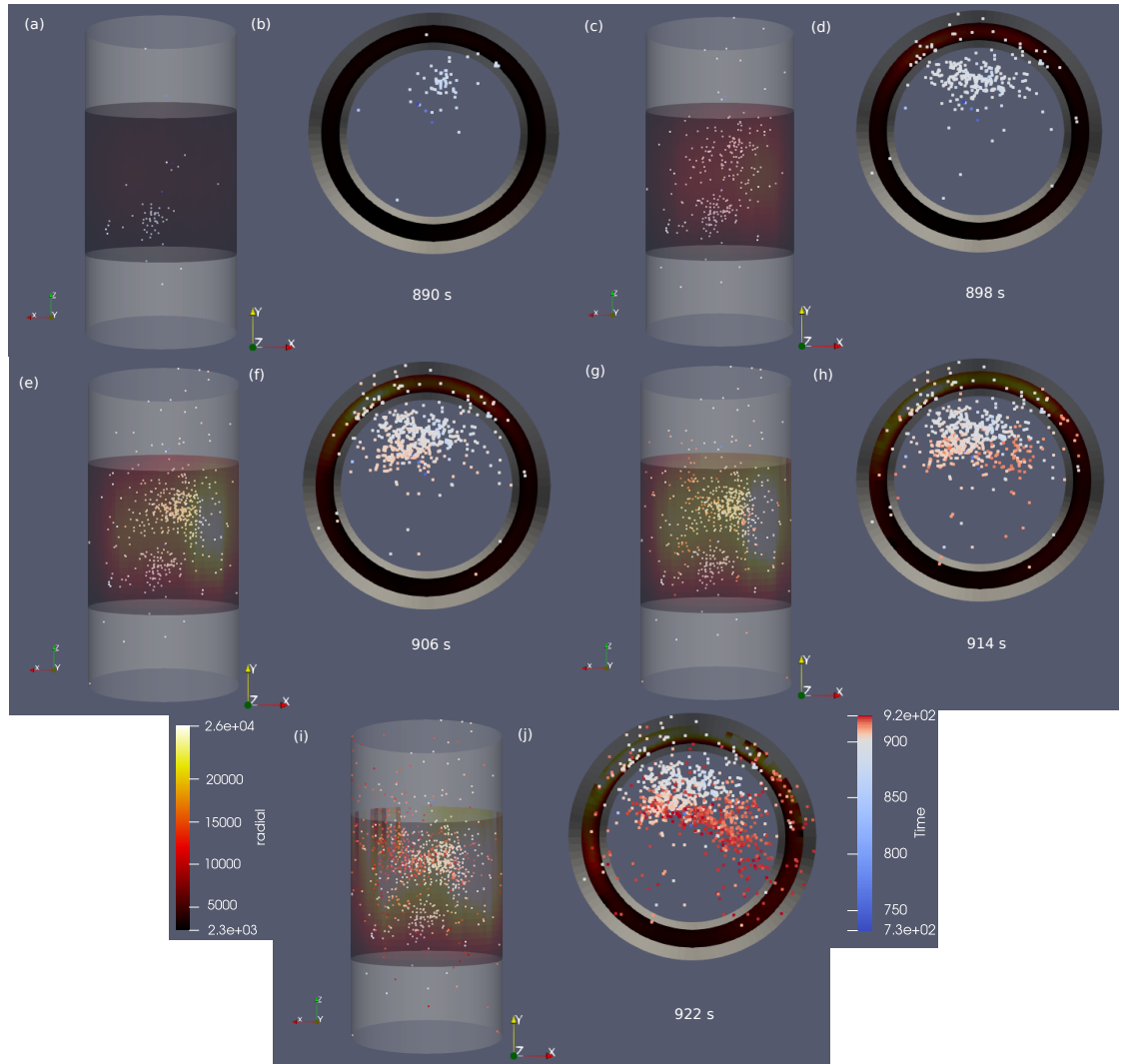


Figure 4.9: Comparison of the localization results at 890 s (a, b), 898 s (c, d), 906 s (e, f), 914 s (g, h) and 922 s (i, j) with surface hoop strain field measured with the optical fibers.

monotonously shrinks in the axial direction and expands in the hoop and radial direction, which suggests linear elastic behavior (Davis and Selvadurai, 2005). The strain does not change linearly with deviatoric stress, indicating the existence of important anelastic mechanisms. The changes of tangent modulus as the deviatoric stress increases from around 5 MPa to 50 MPa is most likely due to the deformation of the pre-existing pores and micro-cracks (Davis and Selvadurai, 2005).

The non-linear trend as deviatoric stress increases to 230 MPa is more complex and harder to explain. van der Baan and Chorney (2019) proposed that anelastic deformation is almost proportional to the cumulative moment based on his numerical simulation using the bonded-particle method. Seismic deformation, therefore, seems to be an important mechanism for anelasticity. To the author's knowledge, given that their results have not been confirmed by experiments and simplifications on the rock materials have been made in simulation, it is not clear if seismic deformation is the only mechanism for anelasticity. To estimate anelastic deformation from fiber optics, an elastic segment of deformation between 50 MPa and 150 MPa is assumed and marked with black circles in Figure 4.10. The elastic trend is subtracted from the total deformation and the results are shown with the green curves. Comparing with the cumulative moment in Figure 4.10, some similarities seem to exist. More rigorous discussion will be given in Section 5.1.

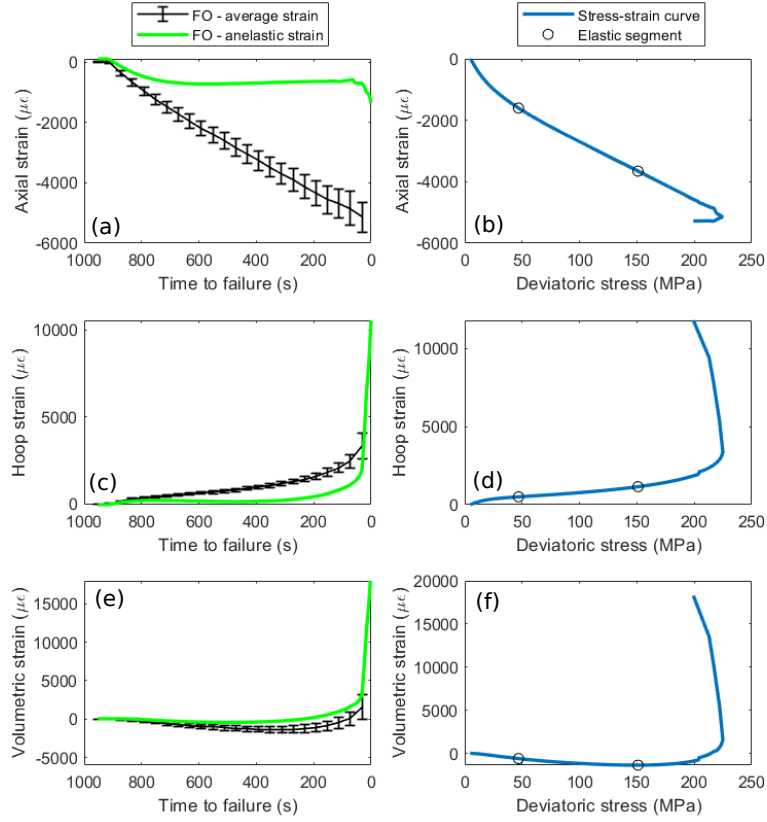


Figure 4.10: Variation of axial (a), hoop (c) and volumetric (e) strain with the time to failure. The black curves with error bars are the averaged total strain values across the sample and the green curves are the anelastic strain of each component. The variation of the above three components with the deviatoric stress is shown in (b), (d) and (f), respectively. Black circles mark the proposed elastic segment in deformation.

Discussion

Both seismic and aseismic deformation of the sample as it approaches failure in LBQ2 will be discussed in combination of the locations, moment tensors of AE events and the strain field from FO. These measurements will be first discussed in averaged sense across the entire sample by comparing seismic moment release with the anelastic deformation in Section 5.1. Seismic statistics will then be analyzed in terms of the spatial and temporal distribution of the occurrence, magnitudes and orientations of the events in Section 5.2. This will shed light on the ways seismicity are related to the fault propagation and the occurrence of major events. Then, stress inversion results are compared with FO measurement in Section 5.3. The discussion will be ended in the preliminary discussion of how the occurrence of AEs seem to perturb the strain field in Section 5.4.

5.1 The relationship between the seismic moment release and the anelastic deformation across the sample

As explained in Section 3.2.7, volumetric deformation due to seismic events can be estimated from the scalar moment using Eq.(3.17). Lei et al. (1992) also found correlations between the volumetric strains with AEs in his experiments on rock with various grain sizes. For the above reasons, the volumetric strain is compared with cumulative moment in Figure 5.1. The cumulative volumetric deformation estimated from the moment tensors is also compared to account for the angle between the slip and normal vectors. Both cumulative moment and cumulative volumetric deformation are divided by the bulk modulus times the volume of the sample to keep them having the same unit as volumetric strain. This makes it possible to estimate the proportion of anelastic deformation that can be accounted for by the seismic moment. If just considering the proportion of seismic and aseismic data before the failure of the FO sensors, the ratio between the seismic deformation and the total anelastic deformation increases from $[0.07 \text{ to } 0.66] \times 10^{-2}\%$. In order to estimate the upper bound of this ratio, it is assumed that, after the failure of FO sensors, the anelastic deformation becomes purely seismic. With this assumption, it is estimated that the ratio increases from around $[0.07 \text{ to } 4] \times 10^{-2}\%$ as the sample approaches failure. While the proportion can increase if the magnitude of completeness in the seismic catalog can be lowered, the amount of energy released by those small events is unlikely making up for the large discrepancy between the cumulative moment and the anelastic volumetric strain. Such low proportion might result from that most anelastic deformation comes from aseismic processes. Similar observations have also been made from the field scale (Maxwell et al., 2009; Maxwell and Rutledge) to the laboratory scale (Goodfellow et al., 2015). Albeit small, the deformation related to the seismic moment seems to play a more important role (two orders of magnitude larger in LBQ2) as the sample approaches failure.

Such increase in the proportion of seismic related anelastic deformation seems more prominent when the angle between the slip and the normal vectors is considered. It is found that the cumulative volumetric deformation does not monotonously increase with time but drops until around

17 seconds before the failure. The time of failure is defined at the time of occurrence of the largest event, which is around 931 s. Given that the increase of anelastic deformation occurs much earlier than the time of increase of the anelastic volumetric strain, it is more certain that aseismic processes are predominant at the early stage of damage.

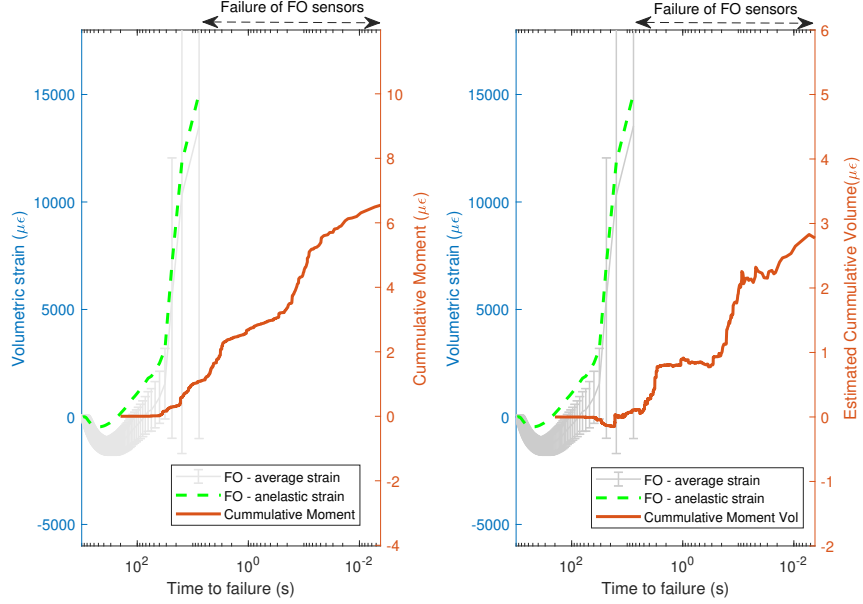


Figure 5.1: (a) Comparison between the averaged anelastic deformation and cumulative moment. The cumulative moment is converted to the same unit as strain through dividing it by divided by the bulk modulus times the volume of the sample. (b) Comparison between the averaged anelastic deformation and cumulative volumetric deformation estimated from the moment tensors.

5.2 What occurs on the spatio-temporal front

Temporal distribution of the occurrence of the events is shown Figure 5.2. The cumulative number of events and the occurrence rate is plotted against the time to failure. The occurrence rate curve is fitted against the modified Omori's law (Lei and Ma, 2014). The exponential index is around -0.83, close to the value pointed out by Lei et al. (2003).

In Figure 5.3, temporal variation of fractal dimension, b-value and types of moment tensors are shown together for comparison.

Before discussing the correlations between statistical variables, the two large scale structures mentioned in Section 4 are discussed since they may also control some aspects of those statistical variables. There are many hints pointing to the possibility that these two structures are large scale faults. (1) In Figure 4.3b, the P-wave velocity drops at 900s between the sensor pair whose ray path intersects the structures but not between the pair that does not intersect. The existence of a large-scale fault can explain such observation. (2) Also, the orientations of the “Principal vector 1” in Figure 4.8a and 4.8b are found to be perpendicular to the strike of the fault. This is consistence with the fault theory (Anderson, 1905). (3) The final and, probably, the most convincing evidence might come from the FO. The peak of strain close to the locations of the two large AE clusters might be the outcrops of the faults at the surface of the sample. The above evidences give us some confidence in assuming that the two clusters are large-scale faults in the following discussions.

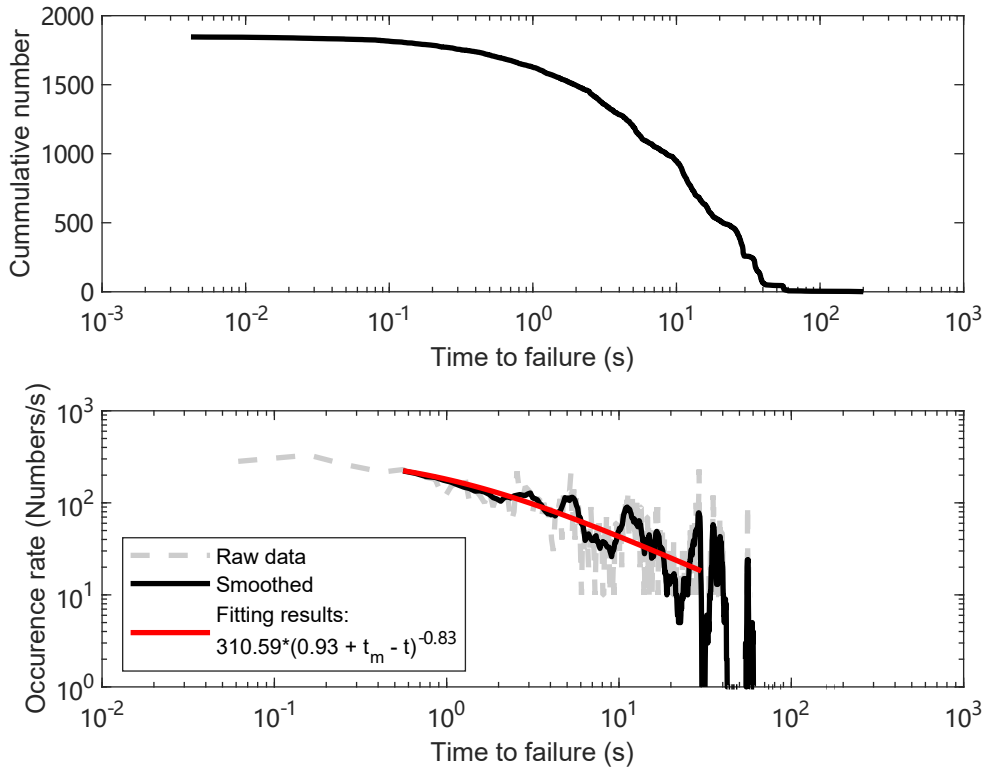


Figure 5.2: (a) The cumulative number of events against the time to failure. (b) The occurrence rate against the time to failure at the log-log scale. The dashed gray curve is the raw occurrence rate computed from the full seismic catalog in LBQ2. The solid black curve smooths the variation for better visualization of the trend and red curve is fitted using the raw data against the modified Omori's law.

Spatial distribution is characterized by the change of fractal dimension with time. As known from the locations of the events, a fault first propagated upwards from around 890 s to around 900 s. During this period the fractal dimension increased indicating the delocalization of events as the fault propagated. Next, the events localized again from 900 s to around 906 s, representing the nucleation of the new fault that would propagate in a different direction later. Then, during the propagation of new faults, the fractal dimension oscillated around 1.5, probably indicating the stop and propagation of the fault before failure. Immediately before the failure (around 931 s), the fractal dimension dropped from ~ 1.6 to ~ 1.4 , which may correspond to the nucleation of the rupture front at a large aperture.

B-value is an often-used indicator of seismicity in the sample. The lower the b-value, the higher the probability that large seismic events may occur. From Figure 5.3b, from around 890 to around 898 s, during the propagation of the first fault, b-value drops from around 1.32 to around 0.88. Then, the position of the loading piston was held, accompanied by a small recovery of b-value. It is kept around 1.00 from 903 to 923 s until a further drop to around 0.80 right before the failure of the rock.

In Figure 5.3c, we looked at the types of events that also vary with the development of damage in the rock sample. During the propagation of the first fault, angles between the normal and the slip vectors increase from around 100 to 108 degrees, together with the drop of DC component. It shows that the sample is still shrinking and the events are becoming more compressive as the fault propagates. But since the change of the direction of the fault, the angles start to drop and reach 90 degrees at around 923 s. Then, the angles oscillate around 87 degrees. This indicates that events become predominantly expansive before the failure of the sample. This is also consistent with the observations in the cumulative volumetric deformation in Figure 5.1b.

Previous studies tried to find correlations between the b-value and the fractal dimension. [Lei et al. \(2000b, 2003\)](#) found that scattered background AEs results in relatively higher b-values. By assuming constant stress drop and isotropic rupture, it was estimated and also observed by [Goebel et al. \(2017\)](#) that the fractal dimension is nearly proportional to b-value with a slope of around 2. However, the spatio-temporal variation of the two variables was not looked at. The fractal dimension is plotted against the b-value at the same time in LBQ2 in Figure 5.4. It is found that the correlation is not as simple as previous observations. While the fractal dimension is at least generally positively correlated to the b-value after 899 s (during the propagation of the second fault), such correlation is reversed during the development of the first fault. This probably comes from the fact that the increase of seismicity at this stage is accompanied with the propagation of the fault. This may be a different mechanism of failure from that proposed by [Lei et al. \(2003\)](#) where seismicity increased as the scattered background AEs becomes localized in a certain region. The latter mechanism might be related to the eventual failure of the sample in LBQ2 between 923 and 931 s.

5.3 Orientation of the strain/stress field and that of the cracks

In Section 4.4, the orientation of the stress field in x-y plane seems to be re-oriented by around 30 degrees after 898 s according to the stress inversion. To validate the inversion results, peaks in the surface strain field are chosen as another indicator for the re-orientation. The results are shown in Figure 5.5 and such change in the orientation is also approximately 30 degrees. This is only a preliminary attempt on the validation of unstructured inversion in 3D geometry. More experiments need to be conducted to justify the application of stress inversion in the experiments.

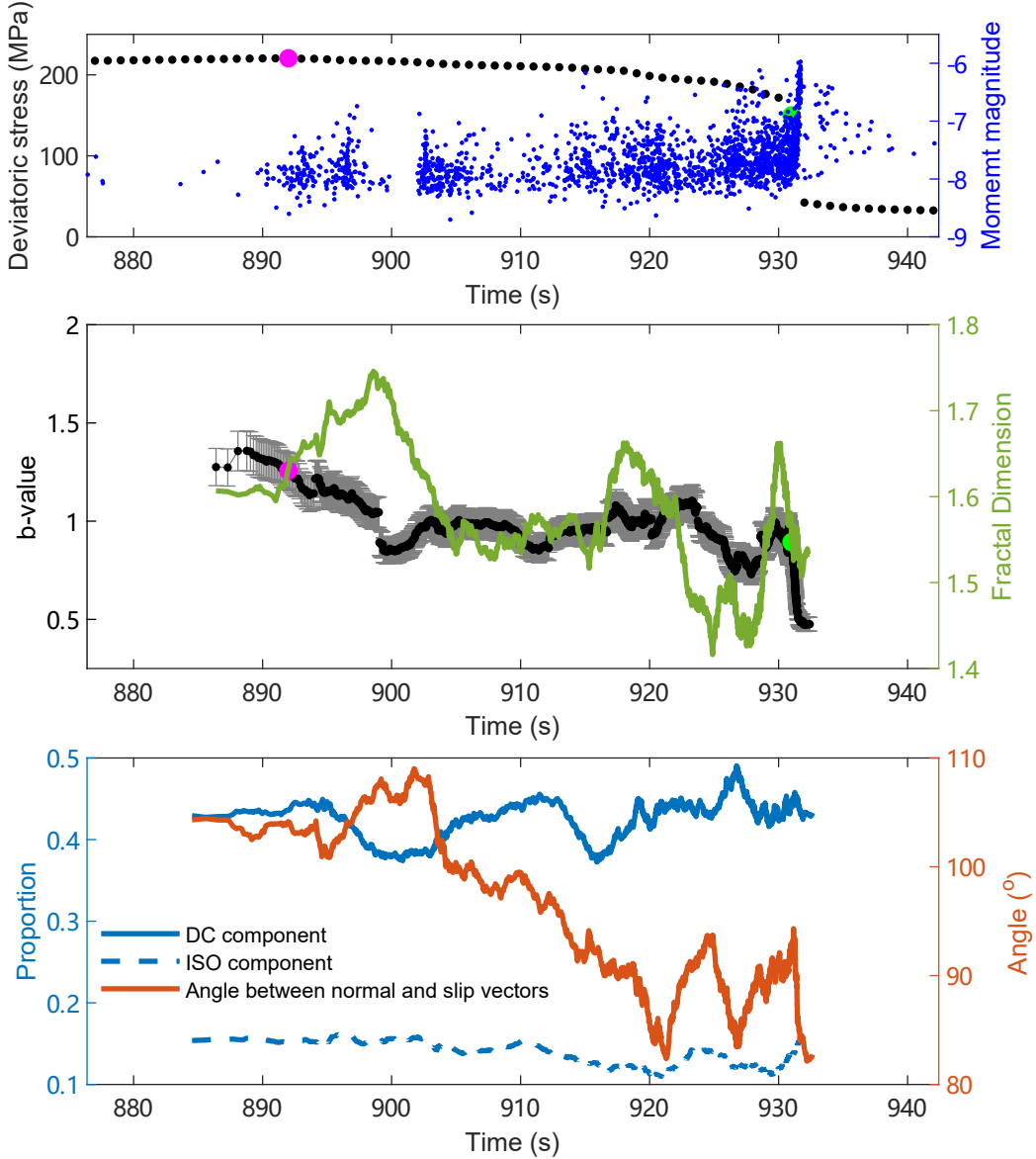


Figure 5.3: (a) The change of deviatoric stress (black dots) and moment magnitude of events (blue dots) in time serving as the indicator of the loading stage as statistical variables varies. The pink dots indicate the start of nucleation and propagation of the first fault, while the green dots mark the failure of the sample (the time when the sudden stress drop occurs). (b) Temporal variation of the b-value and the fractal dimension. (c) Temporal variation of different components of the moment tensors (the solid and dashed curves) and of the angle between normal and the slip vectors (the red curve).

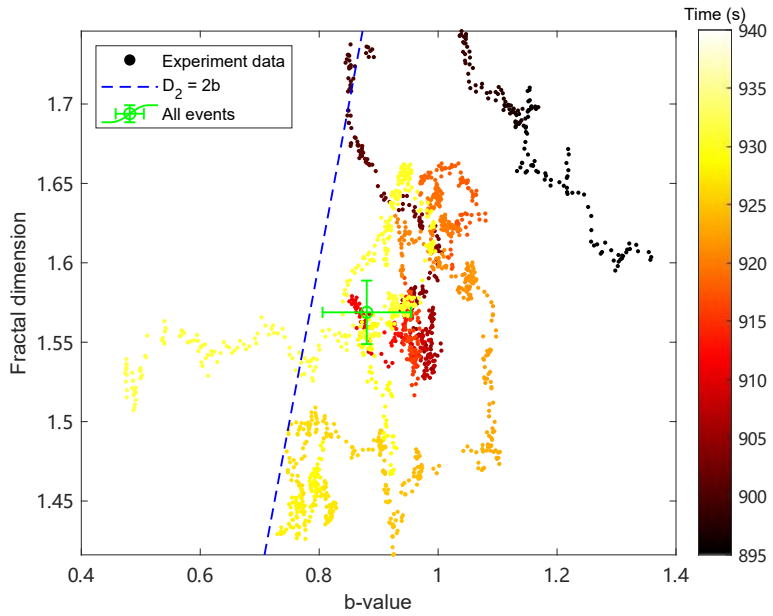


Figure 5.4: The correlation between b-value and fractal dimension (D_2). The values before 898 s (during the upward propagation of the first fault) are marked in black dots and data afterwards are color-coded from brown to yellow. The region where $D_2 = 2b$ is marked by dashed blue line for comparison. The green circle with error bars marks the b-value and the fractal dimension estimated with all the events.

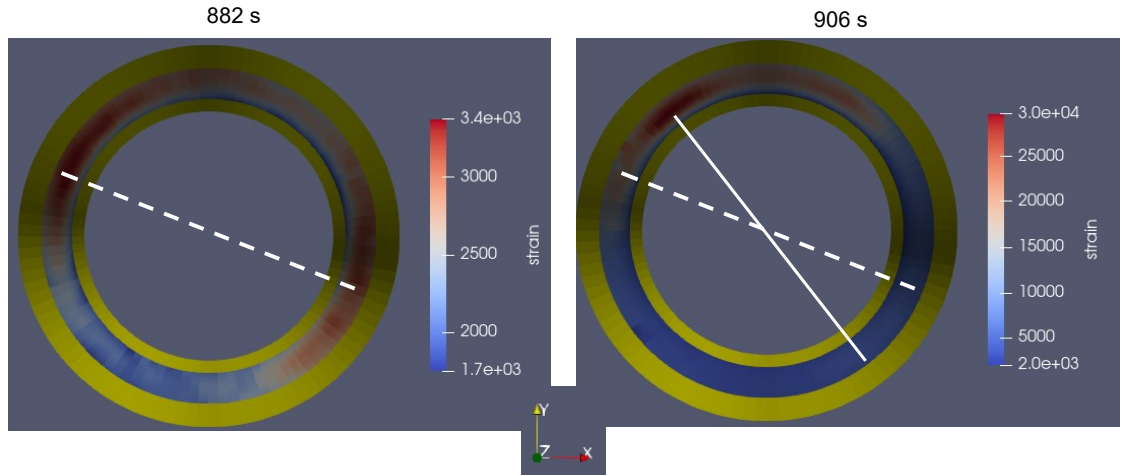


Figure 5.5: Migration of the peaks in the surface strain field from around 882 s (left) to 906 s (right). The dashed white line is at the same position in both subplots, while the solid white line marks the position of the peaks at around 906 s.

5.4 Perturbation of the stress field by AE events

As noted in the previous analysis, two large scale faults seemed nucleate and propagate from 892 to 932 seconds in LBQ2. Such fault propagation was known to be accompanied by the strain field variation due to a stress drop on the fault surfaces. Theoretical and analytical solutions have been derived on how much the stress drop along the fault would perturb the neighboring strain field (Okada, 1992). With the help of the distributed strain measurement with FO, it is now possible to quantify the strain field perturbation.

With a sampling interval of 8 seconds, the strain field was measured for five times during the propagation of the two faults. During the first interval between 890 and 898 s and last three intervals between 898 and 922 s, the first and the second fault propagated respectively. In each eight-second interval, AE events that occurred can be selected and center of these events is determined as the center of stress drop (rectangles with black edges in Figure 5.6a and 5.6b). From previous studies (Okada, 1992), the level of strain perturbation by a point source is roughly proportional to r^{-1} , where r is the distance from the source to the point of interest. Figure 5.6c to 5.6f shows how the hoop (or radial) strain variation on the surface of the sample change with the distance to the center in each of the five intervals. It is found that during the first two intervals (see Figure 5.6c and 5.6d), the strain variation is almost proportional to r^{-1} and r^{-2} , respectively, with relatively high goodness-of-fit of 0.89 and 0.82. As time goes by, during the two later intervals, the points become less focused along the fitting curve and it seems that the strain variation is less likely a simple function of only distance. This probably results from the existence of the first fault in the hanging wall, increasing the rock heterogeneity there. And the partial loss of light in FO sensors, as can be observed in Figure 4.9i and 4.9j, during the last measurement is also playing a role in the scattered measurements.

While the strain perturbation seems agree to analytical solutions during the early stage of damage, not enough data is available so far to justify the repeatability. Moreover, the above analysis neglects the influence on the perturbations by the shapes and orientations of the events clusters. As discussed in Section 5.1, seismic related deformation may only account for $[0.07 \text{ to } 4] \times 10^{-2}\%$ of the total anelastic volumetric deformation. The stress perturbation from aseismic slip should also be considered. These are possible directions to go with more experiments conducted in the future.

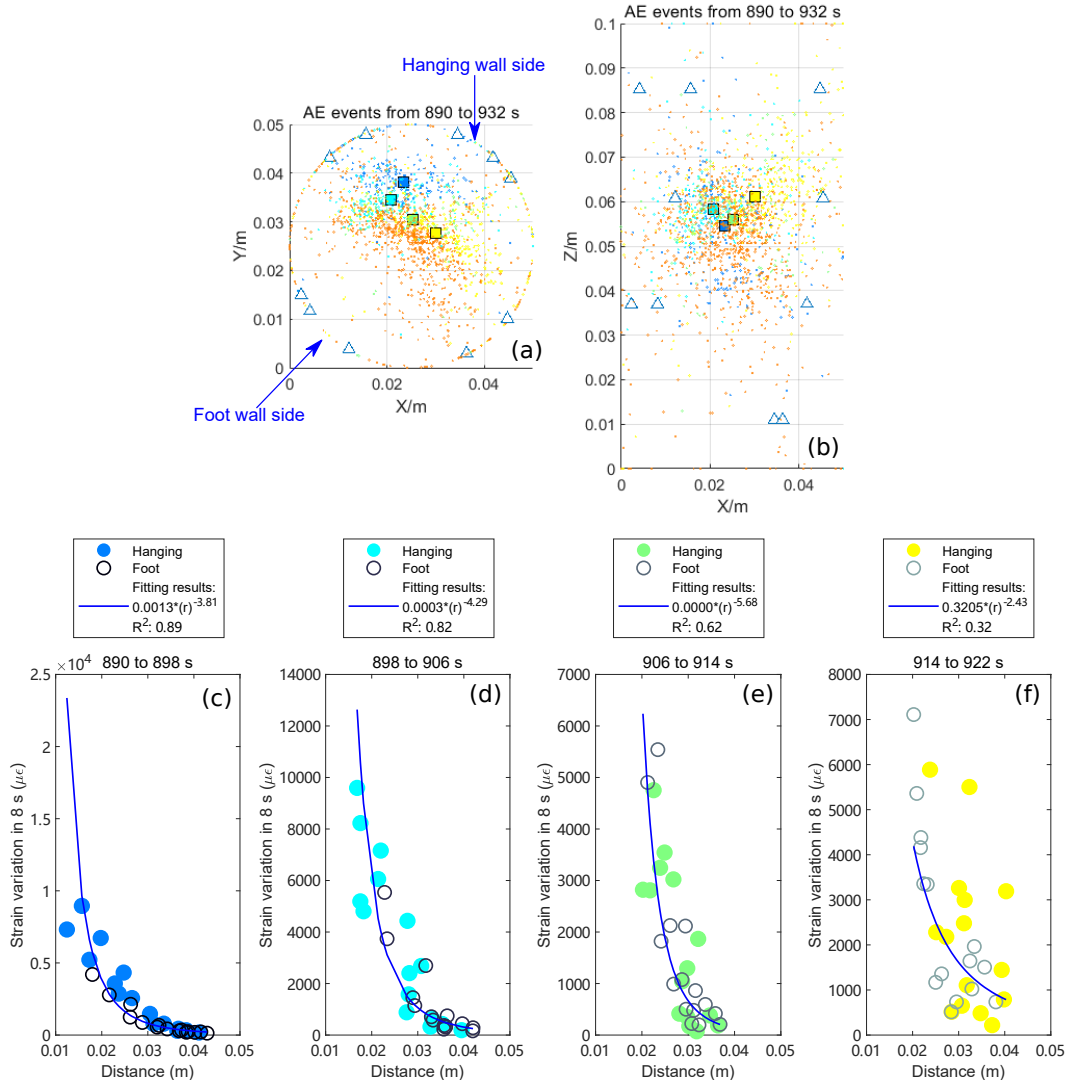


Figure 5.6: Perturbations of the strain field by the AE events. The events from 890 to 922 s are divided into 4 clusters every eight seconds. The clusters are colored in blue, cyan, green and yellow. Events between 922 and 932 s (marked by orange dots in a and b) are not related to FO measurement due to lack of measurement then. Center of each cluster is marked by a filled square in (a and b). The change of the hoop strain field in these 8-second intervals are also computed and is averaged on a coarse grid on the sample surface with a grid-size of 16 mm. And the changes are plotted against their distances to the cluster center in the same time interval in (c-f). The color-coded solid circles are strain variations on the hanging-wall of the faults while the gray circles are on the foot-wall of the faults. The solid blue curves in (c-f) are linearly fitted in the log-log space.

Conclusions

6.1 Summary

With the data processing toolbox that developed in this thesis, seismic events recorded by the broadband piezoelectric sensors can be located, inverted for their moment tensors and eventually compared against the measured strain field on the sample surface using the fiber optics technology. Three confined compression tests on the intact cylindrical Rotondo granite samples have been conducted, through which the loading protocols and the parameters in the acquisition system are improved step by step. Based on the results obtained from the three experiments, especially from LBQ2, seismic and aseismic processes before the failure of the intact Rotondo granite sample have been studied. The stories of how the two processes intertwine with each other and cause the failure of the sample are summarized as follows.

- Aseismic deformation may be the predominant process during the failure of rock in the confined compression test. In LBQ2, it is found that the seismic deformation only accounts for $[0.07 \text{ to } 4] \times 10^{-2}\%$ of the total anelastic deformation and it seems to play a more important role (two orders of magnitude larger) as the sample approaches failure. Such relationship is based on the measurement of the distributed strain field and is, therefore, more representative of the entire volume than the point measurement.
- The temporal distribution of seismic events is studied. It is found that the occurrence rate curve is almost following the modified Omori's law ([Lei and Ma, 2014](#)). The exponential index is around -0.83, close to the value pointed out by [Lei et al. \(2003\)](#).
- Fractal dimension, b-value in GR relation and the angle between normal and slip vectors of moment tensors are all closely related to the stage of failure in the rock. The first large scale fault seems to nucleate between ten to twenty seconds before reaching peak stress. Statistical variables are not estimated in this period since only a few tens of events are detected. At around 890 s, the fault starts to propagate upward following the drop in axial stress. At the same time, the b-value starts to drop indicating the increase of large events while the fractal dimension and the angle between normal and slip vectors increased. Since the latter is kept larger than 90 degrees, the seismic related deformation is still compressive, which is also observed in the curve of cumulative volume change in Figure 5.1b. The propagation of the first fault, as well as the change of the loading condition to "hold position" at around 898 s, the stress field is likely re-orientated by around 30 degrees. These might lead to the change of direction of the fault propagation (marked by cluster inside the pick circle in Figure 4.5b). During the first few seconds (until around 905 s), the fractal dimension deceases probably due to the localization of the events at the asperities as the direction alters. Afterwards, both the b-value and the fractal dimension are almost kept constant until around 922 s, which is also roughly the time when the seismic related deformation becomes tensile according to the normal and slip vectors. Later on, the b-value and the fractal dimension fall together until the eventual failure of the entire sample (the sudden stress drop at around 931 s). This means the focusing of events at this time is accompanied by increase of the magnitude.

- At the early stage of failure before large scale fractures fully developed, the perturbation on the strain field is found to be nearly inversely proportional to r^n , where n is around 4, as predicted by analytical solutions from Okada (1992). Here, r is the distance from the point of interest to the center of seismic clusters. Such quantitative agreement was previously impossible without a distributed strain measurement from the fiber optics cables. Since aseismic deformation is found to play the major role in failure, the fact that strain varies as a function of r might indicate that the center of aseismic deformation is close to the center of seismicity. This is still a nice start, indicating the possibility of further linking the displacement at the surface to seismic and aseismic deformation patterns within the rock. But more experiments are required to confirm the observations.

With the help of the fiber optics technology, the method of unstructured stress inversion in 3D geometry is also preliminarily validated in this thesis. The change in the orientations of the stress field according to stress inversion is also confirmed by the strain field measurement. This provides confidence in relying on stress inversion to estimate stress field inside the rock sample, as a compensation for the surface measurement with the fiber optics cables.

6.2 Outlook

Following the roadmap built in this thesis, the data from the experiments conducted with the LabQuake facilities can be successfully processed and used to interpret the failure of rock in terms of physics and seismic statistics. High potentials in LabQuake are foreseen with the preliminary observations in this thesis. The technical aspects of data collection and processing are discussed in the first place.

- With more sensors attached to the sample, more complete and accurate seismic catalogs can be constructed. Because this means more signals with low SNR can be neglected while keeping sufficient accuracy in localization and moment tensor inversion. For example, it is recommended in HybridMT (Kwiatek et al., 2016) that for stress inversion, measurements of P-wave omega at minimum of eight stations are required. However, in practice, recordings at some sensors can be of low SNR due to their distances to the source or to the wave attenuation. With only ten sensors employed in the experiments in this thesis, some P-wave omegas have to be poorly estimated, reducing the accuracy of the moment tensor inversion.
- In Section 3.2.3, different picking algorithms have been tested and finally a picking algorithm optimized from the AIC picker is employed. But it is far from ideal. In LBQ1, among 2896 events with high enough SNR, only around 2100 events can be localized with sufficient accuracy as a result of the deficiencies in arrival picking. This corresponds to a loss of around 28% percent of the events. Algorithms based on Deep Learning seems to be a promising direction to go with their ability to capture complex features in seismic wave forms (Ross et al., 2018).
- The moment tensor inversion in heterogeneous and anisotropic rock is also not rigorous enough so far as mentioned in Section 3.2.7. In heterogeneous media, the geometric spreading of the wave shall be proportional to the inverse of the square root of the multiplication between the ray Jacobian and the group velocity according to Cerveny (2005). This value along the ray path is not computed in the package FaATSO that we are using for ray tracing. It is also necessary to differentiate between phase velocity and group velocity in anisotropic media in terms of take-off angles and angles of incidence.

Much more improvement can be made technologically, but the ultimate goal is to assist a better understanding of the physical processes in the failure of rocks.

- It is estimated that seismic deformation takes only a tiny proportion of anelastic deformation. But how the aseismic and seismic deformation are correlated in time and space is still ambiguous. To study seismic and aseismic deformation separately, the first step might be discriminating from measurement. The combination of FO and AE provides such possibility. As shown in Section 5.4, since the overall variation in the strain and the seismic sources are known, it seems possible to single out the seismic related changes in strain based on analytical or numerical solutions. Then, it will be possible to only characterize the aseismic deformation during the failure.
- Stress inversion is potentially a powerful tool for understanding the aseismic processes inside the rock if its reliability can be justified. In this thesis, elementary success has been achieved. But the results need to be testified with more experiments for the repeatability.
- While this thesis only focuses on the failure of intact rock, which may exist in nature. But the physical processes might be too complex to be the starting point given that it involves both creation of new rupture front and sliding on the rough faults. It is recommended start from the physics of sliding on the saw cut surface and gradually increase the fault plane complexity to naturally fracture surface with gauges. Then, samples with pre-existing notches can be studied where the fracture can be propagated but with simpler geometry and fracture mode. Maybe after these steps, the failure of intact rock with more complex fractures can be interpreted better.
- The methods developed in this thesis also lay the foundations for the study of the failure of rock during the injection of fluid, which is the major task of LabQuake. The physical processes can be more complex since hydro-mechanical coupling will be involved. But with the framework developed and the familiarities gained so far, it is ready to overcome the forthcoming challenges.

Bibliography

- Akaike, H., 1974. A new look at the statistical model identification. *IEEE transactions on automatic control* 19, 716–723.
- Akazawa, T., 2004. A technique for automatic detection of onset time of p-and s-phases in strong motion records, in: Proc. of the 13th World Conf. on Earthquake Engineering, Vancouver, Canada.
- Aki, K., 1984. Asperities, barriers, characteristic earthquakes and strong motion prediction. *Journal of Geophysical Research: Solid Earth* 89, 5867–5872. URL: <http://dx.doi.org/10.1029/JB089iB07p05867>.
- Aki, K., Richards, P.G., 2002. Quantitative Seismology. University Science Books.
- Amann, F., Gischig, V., Evans, K., Doetsch, J., Jalali, R., Valley, B., Krietsch, H., Dutler, N., Villiger, L., Brixel, B., 2018. The seismo-hydromechanical behavior during deep geothermal reservoir stimulations: open questions tackled in a decameter-scale in situ stimulation experiment. *Solid Earth* 9, 115–137.
- Anderson, E.M., 1905. The dynamics of faulting. *Transactions of the Edinburgh Geological Society* 8, 387–402.
- Anderson, E.M., 1951. The dynamics of faulting and dyke formation with applications to Britain. Oliver and Boyd.
- van der Baan, M., Chorney, D., 2019. Insights from micromechanical modeling of intact rock failure: Event characteristics, stress drops, and force networks. *Journal of Geophysical Research: Solid Earth* 124, 12955–12980.
- Bachmann, C.E., Wiemer, S., Goertz-Allmann, B., Woessner, J., 2012. Influence of pore-pressure on the event-size distribution of induced earthquakes. *Geophysical Research Letters* 39.
- Benson, P.M., Vinciguerra, S., Meredith, P.G., Young, R.P., 2010. Spatio-temporal evolution of volcano seismicity: A laboratory study. *Earth and Planetary Science Letters* 297, 315–323.
- Berger, A., Mercalli, I., Herwegh, M., Gnos, E., 2016. Geological map of the aar massif, tavetsch and gotthard nappes, geological special map no. 129. Federal Office of Topography swisstopo, Wabern .
- Beroza, G.C., Ide, S., 2011. Slow earthquakes and nonvolcanic tremor. *Annual review of Earth and planetary sciences* 39, 271–296.
- Beyreuther, M., Barsch, R., Krischer, L., Megies, T., Behr, Y., Wassermann, J., 2010. Obspy: A python toolbox for seismology. *Seismological Research Letters* 81, 530–533.
- Bhattacharya, P., Viesca, R.C., 2019. Fluid-induced aseismic fault slip outpaces pore-fluid migration. *Science* 364, 464–468.
- Bott, M.H.P., 1959. The mechanics of oblique slip faulting. *Geological magazine* 96, 109–117.

- Brace, W., Byerlee, J., 1966. Stick-slip as a mechanism for earthquakes. *Science* 153, 990–992.
- Brantut, N., 2018. Time-resolved tomography using acoustic emissions in the laboratory, and application to sandstone compaction. *Geophysical Journal International* 213, 2177–2192.
- Breckenridge, F., 1990. Transient sources for acoustic emission work. *Progress in acoustic emission*, 20–37.
- Cappa, F., Scuderi, M.M., Collettini, C., Guglielmi, Y., Avouac, J.P., 2019. Stabilization of fault slip by fluid injection in the laboratory and in situ. *Science advances* 5, eaau4065.
- Cerveny, V., 2005. Seismic ray theory. Cambridge university press.
- Chen, L., Liu, Y., Kong, F., He, N., 2011. Acoustic source localization based on generalized cross-correlation time-delay estimation. *Procedia engineering* 15, 4912–4919.
- Cornet, F.H., 2016. Seismic and aseismic motions generated by fluid injections. *Geomechanics for Energy and the Environment* 5, 42–54.
- David, C., Nejati, M., Geremia, D., 2020. On petrophysical and geomechanical properties of Bedretto Granite. Report. ETH Zurich.
- Davis, R.O., Selvadurai, A.P., 2005. Plasticity and geomechanics. Cambridge university press.
- Deichmann, N., Giardini, D., 2009. Earthquakes induced by the stimulation of an enhanced geothermal system below basel (switzerland). *Seismological Research Letters* 80, 784–798.
- Detournay, E., Cheng, A.D., . Poroelastic response of a borehole in a non-hydrostatic stress field, in: *International Journal of Rock Mechanics and Mining Sciences & Geomechanics Abstracts*, Elsevier. pp. 171–182.
- Diehl, T., Kraft, T., Kissling, E., Wiemer, S., 2017. The induced earthquake sequence related to the st. gallen deep geothermal project (switzerland): Fault reactivation and fluid interactions imaged by microseismicity. *Journal of Geophysical Research: Solid Earth* 122, 7272–7290. URL: <https://doi.org/10.1002/2017JB014473>, doi:[10.1002/2017JB014473](https://doi.org/10.1002/2017JB014473).
- Dieterich, J.H., 1979. Modeling of rock friction: 1. experimental results and constitutive equations. *Journal of Geophysical Research* 84, 2161–2168.
- Dresen, G., Kwiatek, G., Goebel, T., Ben-Zion, Y., 2020. Seismic and aseismic preparatory processes before large stick-slip failure. *Pure and Applied Geophysics* 177, 5741–5760.
- Eitzen, D., Breckenridge, F., Clough, R., Fuller, E., Hsu, N., Simmons, J., 1981. Summary of fundamental developments for quantitative acoustic emission measurements. Report. National Bureau of Standards.
- Eitzen, D., Wadley, H., 1984. Acoustic emission: establishing the fundamentals. *Journal of research of the National Bureau of Standards* 89, 75–100.
- Elsys, A., 2017. High Speed Data Acquisition Cards.
- Fitch, T.J., McCOWAN, D.W., Shields, M.W., 1980. Estimation of the seismic moment tensor from teleseismic body wave data with applications to intraplate and mantle earthquakes. *Journal of Geophysical Research: Solid Earth* 85, 3817–3828.
- Frohlich, C., Apperson, K.D., 1992. Earthquake focal mechanisms, moment tensors, and the consistency of seismic activity near plate boundaries. *Tectonics* 11, 279–296.

- Galis, M., Ampuero, J.P., Mai, P.M., Cappa, F., 2017. Induced seismicity provides insight into why earthquake ruptures stop. *Science Advances* 3. URL: <http://advances.sciencemag.org/content/3/12/eaap7528.abstract>.
- Garg, S., Nur, A., 1973. Effective stress laws for fluid-saturated porous rocks. *Journal of Geophysical Research* 78, 5911–5921.
- Gephart, J.W., Forsyth, D.W., 1984. An improved method for determining the regional stress tensor using earthquake focal mechanism data: application to the san fernando earthquake sequence. *Journal of Geophysical Research: Solid Earth* 89, 9305–9320.
- Gischig, V.S., Doetsch, J., Maurer, H., Krietsch, H., Amann, F., Evans, K.F., Nejati, M., Jalali, M., Valley, B., Obermann, A.C., 2018. On the link between stress field and small-scale hydraulic fracture growth in anisotropic rock derived from microseismicity. *Solid Earth* 9, 39–61.
- Glaser, S.D., Weiss, G.G., Johnson, L.R., 1998. Body waves recorded inside an elastic half-space by an embedded, wideband velocity sensor. *The Journal of the Acoustical Society of America* 104, 1404–1412.
- Goebel, T.H., Schorlemmer, D., Becker, T.W., Dresen, G., Sammis, C.G., 2013. Acoustic emissions document stress changes over many seismic cycles in stick-slip experiments. *Geophysical Research Letters* 40, 2049–2054. URL: <https://doi.org/10.1002/grl.50507>, doi:[10.1002/grl.50507](https://doi.org/10.1002/grl.50507).
- Goebel, T.H.W., Hauksson, E., Plesch, A., Shaw, J.H., 2017. Detecting significant stress drop variations in large micro-earthquake datasets: A comparison between a convergent step-over in the san andreas fault and the ventura thrust fault system, southern california. *Pure and Applied Geophysics* 174, 2311–2330. URL: <https://doi.org/10.1007/s00024-016-1326-8>, doi:[10.1007/s00024-016-1326-8](https://doi.org/10.1007/s00024-016-1326-8).
- Goodfellow, S., Nasseri, M., Maxwell, S., Young, R., 2015. Hydraulic fracture energy budget: Insights from the laboratory. *Geophysical Research Letters* 42, 3179–3187.
- Goodfellow, S.D., Young, R.P., 2014. A laboratory acoustic emission experiment under in situ conditions. *Geophysical Research Letters* 41, 3422–3430.
- Grigoli, F., Cesca, S., Priolo, E., Rinaldi, A.P., Clinton, J.F., Stabile, T.A., Dost, B., Fernandez, M.G., Wiemer, S., Dahm, T., 2017. Current challenges in monitoring, discrimination, and management of induced seismicity related to underground industrial activities: A european perspective. *Reviews of Geophysics* 55, 310–340.
- Guglielmi, Y., Cappa, F., Avouac, J.P., Henry, P., Elsworth, D., 2015. Seismicity triggered by fluid injection-induced aseismic slip. *Science* 348, 1224–1226.
- Guglielmi, Y., Nussbaum, C., Jeanne, P., Rutqvist, J., Cappa, F., Birkholzer, J., 2020. Complexity of fault rupture and fluid leakage in shale: insights from a controlled fault activation experiment. *Journal of Geophysical Research: Solid Earth* 125, e2019JB017781.
- Gutenberg, B., Richter, C.F., 1944. Frequency of earthquakes in california. *Bulletin of the Seismological society of America* 34, 185–188.
- Hafner, S., 1958. Petrographie des südwestlichen Gotthardmassivs zwischen St. Gotthardpass und Nufenenpass. Thesis.

- Hafner, S., Günthert, A., Burckhardt, C.E., Steiger, R.H., Hansen, J.W., , Niggli, C.R., 1975. Geologischer atlas der schweiz 1:25000, val bedretto, atlasblatt 68. Schweizerische Geologische Kommission .
- Hanks, T.C., 1979. b values and $\omega\gamma$ seismic source models: Implications for tectonic stress variations along active crustal fault zones and the estimation of high-frequency strong ground motion. *Journal of Geophysical Research: Solid Earth* 84, 2235–2242.
- Hardebeck, J.L., Michael, A.J., 2006. Damped regional-scale stress inversions: Methodology and examples for southern california and the coalinga aftershock sequence. *Journal of Geophysical Research: Solid Earth* 111.
- Harris, F.J., 1978. On the use of windows for harmonic analysis with the discrete fourier transform. *Proceedings of the IEEE* 66, 51–83.
- Hartigan, J.A., Wong, M.A., 1979. Algorithm as 136: A k-means clustering algorithm. *Journal of the royal statistical society. series c (applied statistics)* 28, 100–108.
- Hirata, T., Satoh, T., Ito, K., 1987. Fractal structure of spatial distribution of microfracturing in rock. *Geophysical Journal International* 90, 369–374.
- Hudson, J., Brown, E., Fairhurst, C., 1971. Optimizing the control of rock failure in servo-controlled laboratory tests. *Rock mechanics* 3, 217–224.
- Hudson, J., Pearce, R., Rogers, R., 1989. Source type plot for inversion of the moment tensor. *Journal of Geophysical Research: Solid Earth* 94, 765–774.
- Ito, Y., Obara, K., Shiomi, K., Sekine, S., Hirose, H., 2007. Slow earthquakes coincident with episodic tremors and slow slip events. *Science* 315, 503–506.
- Jacques, A., 2002. Inversion of earthquake focal mechanisms to obtain the seismotectonic stress iv—a new method free of choice among nodal planes. *Geophysical Journal International* 150, 588–609.
- Kanamori, H., 1978. Quantification of earthquakes. *Nature* 271, 411–414.
- Kawasaki, I., Asai, Y., Tamura, Y., Sagiya, T., Mikami, N., Okada, Y., Sakata, M., Kasahara, M., 1995. The 1992 sanriku-oki, japan, ultra-slow earthquake. *Journal of Physics of the Earth* 43, 105–116.
- King Hubbert, M., Rubey, W.W., 1959. Role of fluid pressure in mechanics of overthrust faulting: I. mechanics of fluid-filled porous solids and its application to overthrust faulting. *Geological Society of America Bulletin* 70, 115–166.
- Kurths, J., Herzel, H., 1987. An attractor in a solar time series. *Physica D: Nonlinear Phenomena* 25, 165–172.
- Kurz, J.H., 2015. New approaches for automatic threedimensional source localization of acoustic emissions—applications to concrete specimens. *Ultrasonics* 63, 155–162.
- Kwiatek, G., Martínez-Garzón, P., Bohnhoff, M., 2016. Hybridmt: A matlab/shell environment package for seismic moment tensor inversion and refinement. *Seismological Research Letters* 87, 964–976.
- Labhart, T., 2005. Erläuterungen zum geologischen atlas der schweiz 1: 25000. Val Bedretto, Atlasblatt 68.

- Lei, X., Kusunose, K., Nishizawa, O., Cho, A., Satoh, T., 2000a. On the spatio-temporal distribution of acoustic emissions in two granitic rocks under triaxial compression: the role of pre-existing cracks. *Geophysical Research Letters* 27, 1997–2000.
- Lei, X., Kusunose, K., Rao, M., Nishizawa, O., Satoh, T., 2000b. Quasi-static fault growth and cracking in homogeneous brittle rock under triaxial compression using acoustic emission monitoring. *Journal of Geophysical Research: Solid Earth* 105, 6127–6139.
- Lei, X., Kusunose, K., Satoh, T., Nishizawa, O., 2003. The hierarchical rupture process of a fault: an experimental study. *Physics of the Earth and Planetary Interiors* 137, 213–228.
- Lei, X., Ma, S., 2014. Laboratory acoustic emission study for earthquake generation process. *Earthquake Science* 27, 627–646.
- Lei, X., Nishizawa, O., Kusunose, K., Satoh, T., 1992. Fractal structure of the hypocenter distributions and focal mechanism solutions of acoustic emission in two granites of different grain sizes. *Journal of Physics of the Earth* 40, 617–634.
- Lei, X., Nishizawa, O., Moura, A., Satoh, T., 2005. Hierarchical fracture process in brittle rocks by means of high-speed monitoring of ae hypocenter. *J. of Acoustic Emission* 23, 102.
- Lei, X., Satoh, T., 2007. Indicators of critical point behavior prior to rock failure inferred from pre-failure damage. *Tectonophysics* 431, 97–111.
- Li, B.Q., Du, J., 2020. A methodology for unstructured damped stress inversion of microseismic focal mechanisms: Application to the vaca muerta formation, argentina. *Geophysics* 85, KS39–KS50.
- Li, Q.B., 2015. Acoustic emissions in hydraulic fracturing of Barre granite. Thesis.
- Lockner, D.A., 1993. The role of acoustic emission in the study of rock fracture. *International Journal of Rock Mechanics and Mining Sciences & Geomechanics Abstracts* 30, 883–899.
- Lockner, D.A., Beeler, N.M., 2002. Rock failure and earthquakes. *International Geophysics Series* 81, 505–538.
- Lokajíček, T., Klíma, K., 2006. A first arrival identification system of acoustic emission (ae) signals by means of a high-order statistics approach. *Measurement Science and Technology* 17, 2461.
- Main, I., 1996. Statistical physics, seismogenesis, and seismic hazard. *Reviews of Geophysics* 34, 433–462. URL: <https://doi.org/10.1029/96RG02808>, doi:10.1029/96RG02808.
- Main, I.G., Meredith, P.G., Jones, C., 1989. A reinterpretation of the precursory seismic b-value anomaly from fracture mechanics. *Geophysical Journal International* 96, 131–138.
- Manthei, G., 2005. Characterization of acoustic emission sources in a rock salt specimen under triaxial compression. *Bulletin of the Seismological Society of America* 95, 1674–1700.
- Manthei, G., Plenkers, K., 2018. Review on in situ acoustic emission monitoring in the context of structural health monitoring in mines. *Applied Sciences* 8, 1595.
- Margrave, G.F., 1998. Theory of nonstationary linear filtering in the fourier domain with application to time-variant filtering. *Geophysics* 63, 244–259.
- Marone, C., 1998. The effect of loading rate on static friction and the rate of fault healing during the earthquake cycle. *Nature* 391, 69–72.

- Maxwell, S., Rutledge, J., . Deformation investigations of induced seismicity during hydraulic fracturing, in: 2013 SEG Annual Meeting, OnePetro.
- Maxwell, S.C., Waltman, C., Warpinski, N.R., Mayerhofer, M.J., Boroumand, N., 2009. Imaging seismic deformation induced by hydraulic fracture complexity. *SPE Reservoir Evaluation & Engineering* 12, 48–52.
- McGarr, A., 2014. Maximum magnitude earthquakes induced by fluid injection. *Journal of Geophysical Research: Solid Earth* 119, 1008–1019. URL: <https://doi.org/10.1002/2013JB010597>, doi:[10.1002/2013JB010597](https://doi.org/10.1002/2013JB010597).
- McLaskey, G.C., Lockner, D.A., Kilgore, B.D., Beeler, N., 2015. A robust calibration technique for acoustic systems. *Bulletin of the Seismological Society of America* 105, 257–271.
- Michael, A.J., 1984. Determination of stress from slip data: faults and folds. *Journal of Geophysical Research: Solid Earth* 89, 11517–11526.
- Mignan, A., Komendantova, N., Scolobig, A., Fleming, K., 2016. Multi-Risk Assessment and Governance. *WORLD SCIENTIFIC*. pp. 357–381. URL: https://doi.org/10.1142/9789813207950_0014, doi:[doi:10.1142/9789813207950_0014](https://doi.org/10.1142/9789813207950_0014)[10.1142/9789813207950_0014](https://doi.org/10.1142/9789813207950_0014)
- Miller, S.A., Collettini, C., Chiaraluce, L., Cocco, M., Barchi, M., Kaus, B.J., 2004. Aftershocks driven by a high-pressure co 2 source at depth. *Nature* 427, 724–727.
- Mogi, K., 1966. Some presice measurements of fracture strength of rocks under uniform compressive stress. *Felsmech. Ingenieurgeol.* 4, 41.
- Moradian, Z., Einstein, H.H., Ballivy, G., 2016. Detection of cracking levels in brittle rocks by parametric analysis of the acoustic emission signals. *Rock Mechanics and Rock Engineering* 49, 785–800.
- Nasseri, M.H.B., Goodfellow, S.D., Wanne, T., Young, R.P., 2013. Thermo-hydro-mechanical properties of cobourg limestone. *International Journal of Rock Mechanics and Mining Sciences* 61, 212–222. URL: <http://www.sciencedirect.com/science/article/pii/S1365160913000579>, doi:<https://doi.org/10.1016/j.ijrmms.2013.03.004>.
- Nielson, G.M., 1983. A method for interpolating scattered data based upon a minimum norm network. *Mathematics of computation* 40, 253–271.
- Obara, K., 2002. Nonvolcanic deep tremor associated with subduction in southwest japan. *Science* 296, 1679–1681.
- Obara, K., Kato, A., 2016. Connecting slow earthquakes to huge earthquakes. *Science* 353, 253–257.
- Ohnaka, M., 1992. Earthquake source nucleation: a physical model for short-term precursors. *Tectonophysics* 211, 149–178.
- Okada, Y., 1992. Internal deformation due to shear and tensile faults in a half-space. *Bulletin of the seismological society of America* 82, 1018–1040.
- Passelègue, F.X., Latour, S., Schubnel, A., Nielsen, S., Bhat, H.S., Madariaga, R., 2017. Influence of fault strength on precursory processes during laboratory earthquakes. *Fault Zone Dynamic Processes* , 229–242.

- Peng, Z., Gomberg, J., 2010. An integrated perspective of the continuum between earthquakes and slow-slip phenomena. *Nature geoscience* 3, 599–607.
- Petrucelli, A., Vannucci, G., Lolli, B., Gasperini, P., 2018. Harmonic fluctuation of the slope of the frequency–magnitude distribution (b-value) as a function of the angle of rake. *Bulletin of the Seismological Society of America* 108, 1864–1876.
- Proctor, B., Lockner, D., Kilgore, B., Mitchell, T., Beeler, N., 2020. Direct evidence for fluid pressure, dilatancy, and compaction affecting slip in isolated faults. *Geophysical Research Letters* 47, e2019GL086767.
- Rast, M., 2020. Geology, geochronology and rock magnetics along bedretto tunnel (gotthard massif, central alps) and numerical modelling of quartz-biotite aggregates-appendix a .
- Rogers, G., Dragert, H., 2003. Episodic tremor and slip on the cascadia subduction zone: The chatter of silent slip. *Science* 300, 1942–1943.
- Ross, Z.E., Meier, M., Hauksson, E., Heaton, T.H., 2018. Generalized seismic phase detection with deep learning. *Bulletin of the Seismological Society of America* 108, 2894–2901.
- Rubin, A.M., Ampuero, J., 2005. Earthquake nucleation on (aging) rate and state faults. *Journal of Geophysical Research: Solid Earth* 110.
- Rubinstein, S., Cohen, G., Fineberg, J., 2007. Dynamics of precursors to frictional sliding. *Physical review letters* 98, 226103.
- Salazar, A.V., Rabaiotti, C., Germanovic, L., Puzrin, A., in preparation. Distributed strain measurement (dsm) in triaxialtests (tt). in preparation .
- Schneider, T., 1985. Basistunnel furka - geologische aufnahme des fensters bedretto. Technical report, FurkaOberalp-Bahn AG, Brig. .
- Scholz, C., 1968. Microfracturing and the inelastic deformation of rock in compression. *Journal of Geophysical Research* 73, 1417–1432.
- Scholz, C.H., 2015. On the stress dependence of the earthquake b value. *Geophysical Research Letters* 42, 1399–1402.
- Scholz, C.H., 2019. The mechanics of earthquakes and faulting. Cambridge university press.
- Scotti, O., Cornet, F., 1994. In situ evidence for fluid-induced aseismic slip events along fault zones, in: International journal of rock mechanics and mining sciences & geomechanics abstracts, Elsevier. pp. 347–358.
- Selvadurai, P.A., 2019. Laboratory insight into seismic estimates of energy partitioning during dynamic rupture: An observable scaling breakdown. *Journal of Geophysical Research: Solid Earth* 124, 11350–11379.
- Selvadurai, P.A., Wu, R., Bianchi, P., Niu, Z., Michail, S., Madonna, C., Wiemer, S., . A methodology for reconstructing absolute source properties of actuated piezoelectric sensors. Submitted to *Journal of Nondestructive Evaluation* .
- Sergeev, S.A., Meier, M., Steiger, R.H., 1995. Improving the resolution of single-grain U/Pb dating by use of zircon extracted from feldspar: Application to the variscan magmatic cycle in the central alps. *Earth and Planetary Science Letters* 134, 37–51.

- SFOE, 2018. Energy strategy 2050. URL: <https://www.bfe.admin.ch/bfe/en/home/policy/energy-strategy-2050.html>.
- Shapiro, S., Patzig, R., Rothert, E., Rindschwentner, J., 2003. Triggering of seismicity by pore-pressure perturbations: Permeability-related signatures of the phenomenon. Springer. pp. 1051–1066.
- Shapiro, S.A., 2003. Elastic piezosensitivity of porous and fractured rocks. *Geophysics* 68, 482–486.
- Shelly, D.R., Beroza, G.C., Ide, S., 2007. Non-volcanic tremor and low-frequency earthquake swarms. *Nature* 446, 305–307.
- Sornette, A., Sornette, D., 1990. Earthquake rupture as a critical point: Consequences for telluric precursors. *Tectonophysics* 179, 327–334.
- Stanchits, S., Vinciguerra, S., Dresen, G., 2006. Ultrasonic velocities, acoustic emission characteristics and crack damage of basalt and granite. *Pure and Applied Geophysics* 163, 975–994.
- Steck, A., 1976. Albit-oligoklas-mineralgesellschaften der peristeritluecke aus alpinmetamorphen granitgneisen der gotthardmassivs .
- Sun, J., Deng, Z.J., Tu, M.J., 1991. Effect of stress triaxiality levels in crack tip regions on the characteristics of void growth and fracture criteria. *Engineering fracture mechanics* 39, 1051–1060.
- Torić, N., Brnić, J., Boko, I., Brčić, M., Burgess, I.W., Uzelac, I., 2017. Experimental analysis of the behaviour of aluminium alloy en 6082aw t6 at high temperature. *Metals* 7, 126.
- Trnkoczy, A., 1998. Understanding and setting sta/lta trigger algorithm parameters for the k2. *Appl Note* 41, 16–20.
- Trutnevyte, E., Wiemer, S., 2017. Tailor-made risk governance for induced seismicity of geothermal energy projects: An application to switzerland. *Geothermics* 65, 295–312. URL: <http://www.sciencedirect.com/science/article/pii/S0375650516301316>, doi:<https://doi.org/10.1016/j.geothermics.2016.10.006>.
- Udías, A., Madriaga, R., Buforn, E., 2014. Source Mechanisms of Earthquakes: Theory and Practice. Cambridge University Press.
- Utsu, T., 1961. A statistical study on the occurrence of aftershocks. *Geophys. Mag.* 30, 521–605.
- Utsu, T., Ogata, Y., 1995. The centenary of the omori formula for a decay law of aftershock activity. *Journal of Physics of the Earth* 43, 1–33.
- Vavryčuk, V., 2011. Tensile earthquakes: Theory, modeling, and inversion. *Journal of Geophysical Research: Solid Earth* 116.
- Vavryčuk, V., 2014. Iterative joint inversion for stress and fault orientations from focal mechanisms. *Geophysical Journal International* 199, 69–77.
- Vavryčuk, V., 2015. Moment tensor decompositions revisited. *Journal of Seismology* 19, 231–252.
- Villiger, L., 2015. Experimental investigation of induced seismicity in granitic rock on centimeter scale. Thesis.

- Villiger, L., Gischig, V.S., Doetsch, J., Krietsch, H., Dutler, N.O., Jalali, M., Valley, B., Selvadurai, P.A., Mignan, A., Plenkers, K., 2020. Influence of reservoir geology on seismic response during decameter-scale hydraulic stimulations in crystalline rock. *Solid Earth* 11, 627–655.
- Wallace, R.E., 1951. Geometry of shearing stress and relation to faulting. *The Journal of geology* 59, 118–130.
- Wang, L., Kwiatek, G., Rybacki, E., Bonnelye, A., Bohnhoff, M., Dresen, G., 2020. Laboratory study on fluid-induced fault slip behavior: The role of fluid pressurization rate. *Geophysical Research Letters* 47, e2019GL086627.
- Wiemer, S., Wyss, M., 2000. Minimum magnitude of completeness in earthquake catalogs: Examples from alaska, the western united states, and japan. *Bulletin of the Seismological Society of America* 90, 859–869. URL: <http://dx.doi.org/10.1785/0119990114>, doi:10.1785/0119990114.
- Wu, R., Selvadurai, P.A., Chen, C., Moradian, O., 2020. Revisiting piezoelectric sensor calibration methods using elastodynamic stress waves .
- Xing, G., Zhu, T., 2019. Modeling frequency-independent q viscoacoustic wave propagation in heterogeneous media. *Journal of Geophysical Research: Solid Earth* 124, 11568–11584.
- Yamashita, T., Knopoff, L., 1989. A model of foreshock occurrence. *Geophysical Journal International* 96, 389–399.
- Yu, Z.G., Anh, V., Lau, K.S., 2004. Chaos game representation of protein sequences based on the detailed hp model and their multifractal and correlation analyses. *Journal of theoretical biology* 226, 341–348.

APPENDIX A

Accuracy of localization with ball drop experiments

The accuracy of localization is the foundation for further physical and statistical analysis of the rock failure. It is thus very important to understand how accurate the localization of FaATSO can be in practice. A benchmark test with the equipment for the ball drop experiment (Figure 2.6b) was conducted since the positions of sources (where the ball hits the plate surface) can be recorded with slow motion videos. During the experiment, 12 sensors (white circles in Figure A.1) were attached to the bottom of the steel plate and the ball was dropped from 9 positions (marked by rectangles) on the plate with low or high sensor coverage. The localization results are shown in color-coded dots. It is found that errors in localization are mostly a few millimeters. The drop at position 9 is localized the most inaccurately with errors larger than 1 cm. But the errors are more likely coming from errors in arrival picking since 5 out of the 12 sensors have low SNR for this drop. This bench mark test not only approximated the accuracy of localization can reach with 12 sensors, it also sheds light on the importance of SNR and the accuracy in the arrival picking for localization.

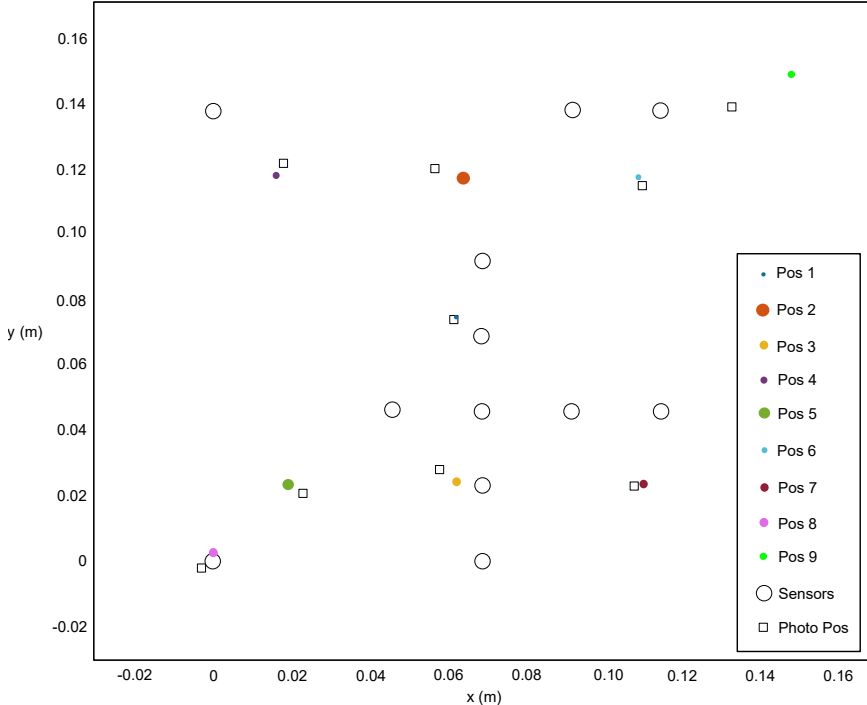


Figure A.1: Validation of the localization results with the adapted FaATSO package. The sensor positions are marked by circles and the ball drop positions from photos are marked by rectangles. The color-coded dots are localization results with FaATSO.

APPENDIX B

Detailed steps in calibration with the capillary fracturing source

As explained in Eq.(3.7) and (3.8), the frequency spectra of sensors' instrument responses are computed from the frequency spectra of the recorded voltage signals ($s(t)$) and theoretical displacement $u_k(x, t)$. The steps on how these two types of frequency spectra are processed from the raw data collected with the force transducer (see Figure 2.6c) and the AE sensors (see Figure 3.18) are illustrated with the flow chart in Figure B.1. The Blackman-Harris (BH) window function (Harris, 1978) is applied to the cropped signals to compensate for the distortion of the frequency spectra due to finite signal lengths.

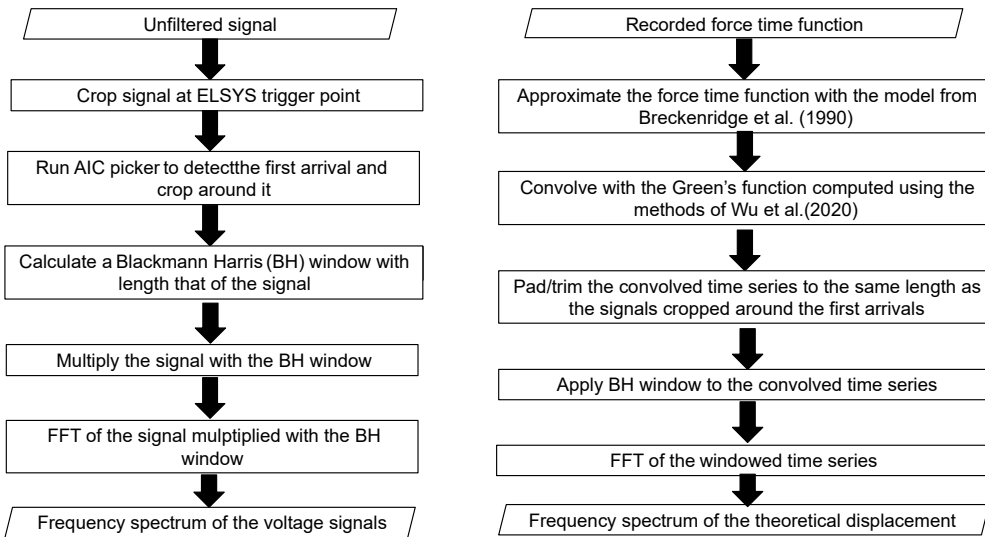


Figure B.1: The flow chart that illustrates how the frequency spectra of the voltage signals and the theoretical displacement are computed.

APPENDIX C

Declaration of Originality

The Declaration of Originality is attached on the following page.



Eidgenössische Technische Hochschule Zürich
Swiss Federal Institute of Technology Zurich

Declaration of originality

The signed declaration of originality is a component of every semester paper, Bachelor's thesis, Master's thesis and any other degree paper undertaken during the course of studies, including the respective electronic versions.

Lecturers may also require a declaration of originality for other written papers compiled for their courses.

I hereby confirm that I am the sole author of the written work here enclosed and that I have compiled it in my own words. Parts excepted are corrections of form and content by the supervisor.

Title of work (in block letters):

Experimental study on the seismic and aseismic deformation during the failure of granitic rock

Authored by (in block letters):

For papers written by groups the names of all authors are required.

Name(s):

Niu

First name(s):

Zihua

With my signature I confirm that

- I have committed none of the forms of plagiarism described in the '[Citation etiquette](#)' information sheet.
- I have documented all methods, data and processes truthfully.
- I have not manipulated any data.
- I have mentioned all persons who were significant facilitators of the work.

I am aware that the work may be screened electronically for plagiarism.

Place, date

Zurich, 27.08.2021

Signature(s)

Zihua Niu

For papers written by groups the names of all authors are required. Their signatures collectively guarantee the entire content of the written paper.